



# **Bioprinting of novel ECM-based electroconductive hydrogels for tissue engineering**

**Catarina Fernandes Roque Ferreira**

Thesis to obtain the Master of Science Degree in

## **Biological Engineering**

Supervisors: Professor Frederico Castelo Alves Ferreira

Doctor Paola Sanjuan Alberte

### **Examination Committee**

Chairperson: Professor Cláudia Alexandra Martins Lobato da Silva

Members of the Committee: Doctor João Carlos Fernandes da Silva

Doctor Paola Sanjuan Alberte

**November 2021**

## **Preface**

The work presented in this thesis was performed at the Institute for Bioengineering and Biosciences of Instituto superior Técnico (Lisbon, Portugal), during the period March-October 2021, under the supervision of Prof. Frederico Ferreira and Dr. Paola Sanjuan Alberte.

This work is financed by national funds from FCT – Fundação para a Ciência e Tecnologia, I. P., in the scope of the project UIDB/04565/2020 and UIDP/04565/2020 of the Research Institute for Bioengineering and Biosciences – iBB and the project LA/P/0140/2020 of the Associate Laboratory Institute for Health and Bioeconomy – i4HB.

I declare that this document is an original work of my own authorship and that it fulfills all the requirements of the Code of Conduct and Good Practices of the Universidade de Lisboa.

## Acknowledgements

First, I would like to thank my supervisors, Prof. Frederico Ferreira and Dr. Paola Sanjuan Alberte, for the opportunity to work on such promising and innovative interdisciplinary field, Tissue Engineering and Bioprinting, for their knowledge, guidance, corrections and productive ideas.

I would also like to thank Mariana Gomes for the all the help and company shared regarding all the lab work.

I would also like to express my gratitude to Laura Sordini for the assistance with electrochemical assays, and Ana Carina Manjua for the knowledge about magnetic nanoparticles.

I would like to thank all my friends for the friendship and laughs throughout these years. Finally, I would like to thank my family, especially my parents for the support and confidence they always had in me throughout my masters, and my siblings, for the patience to put up with me during these more stressful times.

I would like to thank for the funding received from the FCT granted to the project Belive (PTDC/EMD-EMD/30828/2017) to the Research Unit iBB - Institute for Bioengineering and Biosciences ( UIDB/04565/2020 and UIDP/04565/2020) and to i4HB - the Associate Laboratory Institute for Health and Bioeconomy (LA/P/0140/2020). The research group would also like to thanks to PARSUK - Portuguese Association of Researchers and Students in the UK for funding through Portugal-UK Bilateral Research Fund (BRF) 2021 Grant and to the Engineering and Physical Sciences Research Council (EPSRC) for the EPSRC Doctoral Prize award granted through the University of Nottingham(project code RA26DF) to Paola Alberte."

## **Abstract**

In the field of tissue engineering and regenerative medicine, hydrogels are used as biomaterials to support cell attachment and promote tissue regeneration due to their ability to mimic the native tissues' extracellular matrix (ECM). The high biocompatibility and processability of hydrogels have made them prime candidates for 3D bioprinting, where cell-laden 3D structures are formed through layer-by-layer deposition. Interest in ECM hydrogels has increased recently. The ECM is an essential non-cellular component of the tissue microenvironment, that provide structural support and guidance for cell migration, proliferation, differentiation, and maturation. Also, the tunability of the ECM hydrogel's properties, including electrical conductivity, magnetic stimulation, and substrate stiffness allows to produce scaffolds designed to better mimic the native microenvironment, with special interest for cardiac tissue engineering.

In this work, a novel electroconductive ECM-based bioink is formulated. Addition of the conductive polymer PEDOT:PSS to digested ECM preparation, led to bioinks with suitable rheological properties and electrical conductivity. FRESH extrusion bioprinting was used to obtain conductive *in situ* ECM scaffolds. Bioink printability was evaluated with successful results. Biocompatibility was assessed with cell seeding assays for mouse fibroblasts, with > 96.5% cell viability, and cardiomyocytes derived from human induced pluripotent stem cells, with acceptable cell adhesion on PEDOT:PSS hydrogels. Finally, fibroblasts were bioprinted on the developed bioinks, with great success in cell viability, > 93%, but some inability to maintain scaffold self-support. Overall, there was great success in developing a novel conductive bioink formulation for potential application in cardiac tissue engineering.

## **Keywords**

3D FRESH Bioprinting, extracellular matrix, electroconductive hydrogels, cardiac tissue engineering

## **Resumo**

Na área de engenharia de tecidos e medicina regenerativa, os hidrogéis são biomateriais utilizados para fixação celular e promoção de regeneração de tecidos pela sua capacidade de reproduzir a matriz extracelular dos tecidos nativos. A biocompatibilidade e capacidade de processamento destes materiais torna os hidrogéis como principais candidatos para bioimpressão 3D, processo de formação de estruturas embebidas de células formadas por deposição camada-por-camada. O interesse em hidrogéis de matriz extracelular (ECM) tem vindo a aumentar por ser um componente essencial ao microambiente dos tecidos, composto por um vasto conjunto de macromoléculas que providenciam suporte estrutural e direção para migração, proliferação, diferenciação e maturação celular. A capacidade de refinamento das propriedades dos hidrogéis de ECM, como condutividade elétrica, estimulação magnética e rigidez do material de suporte, permitem a produção de scaffolds que melhor representam o tecido nativo, com especial interesse na área de engenharia de tecidos cardíacos.

Neste trabalho, foi formulada uma bio-tinta inovadora de ECM electroquimicamente condutora. A adição do polímero condutor PEDOT:PSS a uma preparação de ECM levou à obtenção de bio-tintas com propriedades reológicas e condutividade elétrica do material adequadas. A printabilidade das tintas foi avaliada, com resultados positivos. A biocompatibilidade dos materiais foi avaliada através do crescimento de fibroblastos de rato em hidrogéis, e através da deposição de hiPSC-CMs, com adesão celular aceitável para hidrogéis com PEDOT:PSS. Fibroblastos foram impressos nas tintas desenvolvidas, com excelentes resultados para viabilidade celular. Foi então possível a formulação de uma nova bio-tinta condutora para potenciais aplicações em engenharia de tecidos cardíacos.

## **Palavras-chave**

Bioimpressão 3D FRESH, Matriz extracelular, hidrogéis electrocondutores, engenharia de tecidos cardíacos

# Table of Contents

|  |           |
|--|-----------|
| <b>Chapter 1 - Introduction</b> .....  | <b>1</b>  |
| 1.1. 3D Bioprinting.....   | <b>1</b>  |
| 1.1.1. Brief introduction to 3D bioprinting .....                                    | 1         |
| 1.1.2. The bioprinting process .....   | 3         |
| 1.2. 3D bioprinting techniques .....   | <b>4</b>  |
| 1.2.1. Extrusion bioprinting .....   | 4         |
| 1.2.2. FRESH extrusion bioprinting.....  | 6         |
| 1.3. Hydrogel and bioink characterization for extrusion bioprinting .....            | <b>7</b>  |
| 1.3.1. Rheological Properties.....   | 7         |
| 1.3.1.1. Storage and loss modulus .....  | 7         |
| 1.3.1.2. Viscosity.....  | 8         |
| 1.3.1.3. Loss factor or damping factor.....  | 9         |
| 1.3.2. Extrusion Parameters .....  | 9         |
| 1.3.2.1. Pressure.....   | 9         |
| 1.3.2.2. Temperature.....  | 9         |
| 1.3.2.3. Speed.....  | 10        |
| 1.3.3. Electrochemical properties.....   | 10        |
| 1.4. Bioinks for 3D FRESH extrusion bioprinting .....                                | <b>11</b> |
| 1.4.1. Natural Polymers .....  | 12        |
| 1.4.1.1. Alginate .....  | 12        |
| 1.4.1.2. Collagen.....   | 13        |
| 1.4.1.3. Gelatin.....  | 13        |
| 1.4.1.4. Decellularized extracellular matrix.....                                    | 13        |
| 1.4.2. Synthetic Polymers.....   | 16        |
| 1.4.3. Strategies to increase the functionality of hydrogels .....                   | 18        |
| 1.4.3.1. Conductive Hydrogels.....   | 18        |
| 1.4.3.2. Piezoelectric hydrogels.....  | 19        |
| 1.4.3.3. Magnetic field-responsive hydrogels .....                                   | 21        |
| 1.5. Bioprinting of cardiac tissues: applications and main limitations .....         | <b>22</b> |
| 1.5.1. In vitro engineering of cardiomyocytes .....                                  | 23        |
| 1.5.1.1. Main traits and characteristics of in vitro engineered cardiomyocytes ..... | 23        |
| 1.5.1.2. Mature vs Immature cardiac cells.....                                       | 24        |
| 1.5.2. Strategies to improve maturity of hiPSC-CMs in vitro .....                    | 24        |
| 1.5.2.1. Long term culture.....  | 24        |
| 1.5.2.2. Electrical Stimulation .....  | 24        |
| 1.5.2.3. Mechanical Stimulation.....   | 25        |
| 1.5.2.4. Substrate topology and stiffness .....                                      | 25        |
| 1.5.2.5. 3D strategies .....   | 25        |
| 1.5.2.5.1. Co-culture .....  | 26        |
| 1.5.2.5.2. 3D Cell Culture.....  | 26        |
| 1.5.2.5.3. Hydrogels .....   | 26        |
| 1.6. Motivation, Aim, Objectives and Research Strategy.....                          | <b>27</b> |
| <b>Chapter 2 – Materials and Methods</b> .....                                       | <b>29</b> |

|   |           |
|---|-----------|
| 2.1. Bioink Formulation.....  | 29        |
| 1.1.1. sisECM digestion.....  | 29        |
| 1.1.2. sisECM hydrogel and bioinks preparation .....                            | 29        |
| 1.1.3. Preparation of gelatin support bath for FRESH extrusion bioprinting..... | 30        |
| 1.1.4. Alginate-gelatin bioink preparation .....                                | 31        |
| 1.1.5. Magnetic field-responsive bioink preparation.....                        | 31        |
| 1.1.6. PEDOT:PSS concentration adjustments .....                                | 31        |
| 2.2. Hydrogel Characterization .....  | 32        |
| 2.2.1. Water content assay.....   | 32        |
| 2.2.2. Stability Assay.....   | 32        |
| 2.3. Electrical characterization.....   | 32        |
| 2.3.1. Resistance .....   | 32        |
| 2.3.2. Four-probe method.....   | 33        |
| 2.3.3. Electrochemical Impedance Spectroscopy (EIS).....                        | 33        |
| 2.4. FRESH extrusion printing .....   | 34        |
| 2.4.1. Bioprinter setup .....   | 34        |
| 2.4.2. Scaffold Design .....  | 35        |
| 2.4.3. Optimization of printing parameters.....                                 | 35        |
| 2.5. Bioink Characterisation.....   | 35        |
| 2.5.1. Rheology – oscillating time sweep .....                                  | 35        |
| 2.5.2. Printability.....  | 36        |
| 2.6. Cell Culture .....   | 36        |
| 2.6.1. hiPSCs culture and passaging .....                                       | 36        |
| 2.6.2. hiPSCs differentiation towards cardiomyocytes.....                       | 36        |
| 2.6.3. Mouse fibroblast culture.....  | 37        |
| 2.6.4. Imaging of cells. ....   | 37        |
| 2.7. Viability assays.....  | 37        |
| 2.7.1. Live/Dead Assay.....   | 37        |
| 2.7.2. Cardiomyocyte’s immunostaining.....                                      | 38        |
| 2.8. Bioinks formulation and bioprinting .....                                  | <b>38</b> |
| 2.8.1. Bioink and gelatin sterilization for bioprinting.....                    | 38        |
| 2.8.2. Bioink preparation for bioprinting.....                                  | 39        |
| 2.9. Statistical analysis.....  | <b>39</b> |
| <b>Chapter 3 - Results and Discussion.....</b>                                  | <b>40</b> |
| 3.1. Optimization of bioinks composition.....                                   | <b>40</b> |
| 3.2. Hydrogel characterization.....   | <b>42</b> |
| 3.2.1 Hydrogel properties .....   | 42        |
| 3.2.1.1. Water Content .....  | 42        |
| 3.2.1.2. Stability of the casted structures .....                               | 43        |
| 3.2.2. Electrical characterization.....   | 43        |

|  |           |
|--|-----------|
| 3.2.2.1. Four-probe Method.....  | 43        |
| 3.2.2.2. Preliminary conductivity assay .....  | 44        |
| 3.2.2.3. Electrochemical Impedance Spectroscopy (EIS) .....                              | 45        |
| <b>3.3. Optimization of the bioprinting conditions.....</b>                              | <b>47</b> |
| 3.3.1. Rheological Characterization of the bioinks.....                                  | 47        |
| 3.3.2. Tuning of bioprinting parameters.....   | 49        |
| 3.3.3. Evaluation of the printability .....  | 52        |
| 3.3.3.1. Uniformity factor .....   | 52        |
| 3.3.3.2. Pore factor.....  | 53        |
| 3.3.3.3. Wall thickness and Pore size .....  | 54        |
| <b>3.4. Preliminary cell viability studies on the different hydrogel materials .....</b> | <b>55</b> |
| 3.4.1. Mouse fibroblasts .....   | 55        |
| 3.4.2. hiPSC-CMs .....   | 58        |
| <b>3.5. Cell bioprinting .....</b>   | <b>61</b> |
| 3.5.1 Mouse Fibroblasts .....  | 61        |
| <b>3.6. Alternative bioinks explored.....</b>  | <b>66</b> |
| 3.6.1 Alginate and Gelatin bioink .....  | 66        |
| 3.6.1.1 Bioink formulation and hydrogel testing.....                                     | 66        |
| 3.6.1.2 Alg-gel printing .....   | 67        |
| 3.6.2 Magnetic particles and sisECM bioink.....  | 70        |
| <b>Chapter 4 - Conclusions and Future Remarks.....</b>                                   | <b>74</b> |



## List of Figures

|  |    |
|--|----|
| Figure 1 - Steps in the bioprinting process .....  | 3  |
| Figure 2 - Schematic diagram of extrusion-based bioprinting pneumatic and mechanical methods: (A) Pneumatic via pressurized air, (B) Piston-driven mechanical extrusion and (C) Screw-driven mechanical extrusion.....   | 4  |
| Figure 3 - FRESH-printing method: A microgel gelatin-support bath is used for printing low viscosity materials. The gelatin can be removed post-printing by heating to 37 °C.....  | 7  |
| Figure 4 - Vector diagram illustrating the relationship between complex shear modulus $G^*$ , storage modulus $G'$ and loss modulus $G''$ using the phase-shift angle $\delta$ . .....   | 8  |
| Figure 5 – Impedance can be expressed as modulus $ Z $ and phase angle $\phi$ or can be given by the real part ( $Z_R$ ) and the imaginary part ( $Z_I$ ) of impedance. ....   | 10 |
| Figure 6 - Scheme of the general ECM space showing some primary ECM components and the interactions between these components and cells.....  | 16 |
| Figure 7 - PEDOT:PSS chemical structure.....   | 19 |
| Figure 8 - sisECM digestion, with constant stirring at room temperature.....   | 29 |
| Figure 9 – A: Schematic for sisECM digestion and hydrogels/bioinks preparation; B: Final dECM hydrogel before incubation (left) and after 30 minutes incubation at 37°C (right) .....  | 30 |
| Figure 10 - Gelatin preparation schematic.....   | 30 |
| Figure 11 - Alginate-Gelatin bioink preparation schematic. ....  | 31 |
| Figure 12 - 4-probes schematic (left), with the representation of the 4 probes (current passes on the outer probes and voltage is read across the inner probes) and gold deposited strips, with $d$ corresponding to the gap between gold strips; and gold deposition chamber (right)..... | 33 |
| Figure 13 – A: Schematic for the two electrode set up for EIS measurements; B: Copper bands for sample deposition, with sisECM + 0.1%PEDOT:PSS sample; C: EIS setup with PalmSens4 potentiostat and Faraday cage.....  | 34 |
| Figure 14 - Bioprinter setup; A: Fisnar Compact Desktop Robot; B: Teach Pendant; C: Air dispensing Unit .....  | 34 |
| Figure 15 - Materials for bioprinting; A: 5 cc end cap; B: 0.3 mm diameter needle; C: 0.6 mm diameter needle; D: 5 cc piston; and E: 5 cc ink cartridge. ....  | 34 |
| Figure 16 - Fisnar Robot Edit software interface, with a square mesh geometry, diagonal mesh geometry, triangle mesh geometry and honeycomb mesh geometry, from left to right, respectively.....   | 35 |
| Figure 17 - 96-well plate for cell seeding assays; 1 - positive control; 2 - sisECM; 3 - sisECM + 0.05% PEDOT:PSS; 4 - sisECM + 0.1% PEDOT:PSS; 5 - negative control .....   | 38 |
| Figure 18 -- Bioink preparation for bioprinting schematic .....  | 39 |
| Figure 19 - Water content results for all three hydrogels; $n=3$ . ....  | 43 |
| Figure 20 - Stability assay results for days 0 and 30 for all bioinks; A: sisECM; B:sisECM + 0.05% PEDOT:PSS; C: sisECM + 0.1% PEDOT:PSS.....  | 43 |
| Figure 21 - Four-probe method results for conductivity for all hydrogels; $n=5$ ; $p < 0.05$ for Student's t-test  | 44 |
| Figure 22 - Results for conductivity obtained for hydrogels with PEDOT:PSS concentrations of 0.01%, 0.05% and 0.1%; $n=5$ .....  | 45 |
| Figure 23 - Impedances for frequencies 0.1; 1; 1000 and 100000 Hz for sisECM, sisECM + 0.05% PEDOT:PSS and sisECM + 0.1% PEDOT:PSS hydrogels; $n=6$ . ....   | 46 |
| Figure 24 – Impedances measured of all hydrogels and copper.....   | 46 |
| Figure 25 - Oscillating time sweep results for all bioinks; Variation of storage and loss modulus through time; $n=3$ ; $p < 0.05$ for Student's t-test. ....  | 47 |
| Figure 26 - Gel point graphs for each bioink.....  | 48 |
| Figure 27 - Results for A: loss factor $\tan \delta$ and B: complex viscosity through time for all bioinks; $n=3$ . .....  | 49 |

|   |    |
|---|----|
| Figure 28 - Pictures of singles strands of sisECM (left), sisECM + 0.05% PEDOT:PSS (center) and sisECM + 0.1% PEDOT:PSS (right).....  | 52 |
| Figure 29 - Uniformity factors for all three bioink conditions; n=6.....  | 53 |
| Figure 30 - Pictures of printed square meshes of sisECM (left), sisECM + 0.05% PEDOT:PSS (center) and sisECM + 0.1% PEDOT:PSS (right).....  | 53 |
| Figure 31 - Pore factors for all three bioink conditions; n=25.....   | 54 |
| Figure 32 - Pictures taken with Leica microscope (10x magnification) of fibroblasts seeded on the 3 different hydrogels and positive control. Days 0 and 7 of cell culture. ....  | 55 |
| Figure 33 - Cell viability assays for mouse fibroblasts, culture for 7 days, for cell seeding in sisECM, sisECM+0.05% PEDOT:PSS and sisECM+0.1%PEDOT:PSS hydrogels; A: growth curve; B: Fold-increase curve; n=6. ....  | 56 |
| Figure 34 - Pictures taken with Leica fluorescence microscope (20x magnification) of fibroblasts seeded on the 3 different hydrogels and positive control on day 7 of cell culture. Green cells (alive) are stained with calcein-AM red cells (dead) with ethidium homodimer-1 .....                          | 57 |
| Figure 35 - Viability results for cell seeding of fibroblasts for all 3 hydrogels; n=6.....   | 57 |
| Figure 36 - hiPSC cells on day -2 of the preparation step of cardiomyocyte differentiation. Photo taken with Leica microscope, at x10 magnification.....  | 58 |
| Figure 37 - hiPSC cells on day -1 of the pre-conditioning step of cardiomyocyte differentiation, presenting cheese-like morphology. Photo taken with Leica microscope, at x10 magnification.....  | 59 |
| Figure 38 - Cells on day 0 of the differentiation step of cardiomyocyte differentiation. Photo taken with Leica microscope, at x10 magnification.....   | 59 |
| Figure 39 - Cells on days 4 (A) and 6(B) of the differentiation step of cardiomyocyte differentiation. Photos were taken with Leica microscope, at x10 magnification. ....  | 60 |
| Figure 40 – Cardiomyocytes from the first differentiation batch. Immunostaining of these cells was performed using Hoechst 33258 – blue, Alexa Fluor-phalloidin - red and anti-TNNI3 – green). Photo taken with Leica microscope, at x10 magnification.....   | 60 |
| Figure 41 - Cardiomyocyte immunostaining results, on two different regions of the well plate; A: positive control; B: sisECM; C: sisECM + 0.05% PEDOT:PSS; D: sisECM + 0.1% PEDOT:PSS .....   | 61 |
| Figure 42 - Pictures taken with Leica microscope (10x magnification) of fibroblasts containing printed structures of the 3 different hydrogels. Days 1, 3 and 5 of cell culture. ....   | 63 |
| Figure 43 - Pictures taken with Leica fluorescence microscope (20x magnification) of fibroblasts printed with sisECM, sisECM + 0.05% PEDOT:PSS and sisECM+0.1% PEDOT:PSS hydrogels on day 7 of cell culture. Green cells (alive) are stained with calcein-AM red cells (dead) with ethidium homodimer-1 ..... | 63 |
| Figure 44 - Viability results for cell bioprinting of fibroblasts for all 3 hydrogels; n=4.....   | 64 |
| Figure 45 - Viability results for bioprinting and cell seeding of fibroblasts; n=4 .....  | 64 |
| Figure 46 - Pictures taken with Leica fluorescence microscope (20x magnification) of fibroblasts printed with sisECM, sisECM + 0.05% PEDOT:PSS and sisECM+0.1% PEDOT:PSS hydrogels on day 7 of cell culture. Green cells (alive) are stained with calcein-AM red cells (dead) with ethidium homodimer-1 ..... | 66 |
| Figure 47 - Stability assay for 2.5%-7.5% alg-gel, 2.5%-7.5% alg-gel+0.05% PEDOT:PSS and 2.5%-7.5% alg-gel+0.1% PEDOT:PSS (left to right, respectively) ; day 0 (top), day 3(middle) and day 5 (bottom).....  | 70 |
| Figure 48 - Transmission electron microscopy for non-functionalized iron oxide (Fe <sub>3</sub> O <sub>4</sub> ) nanoparticles. ...   | 71 |
| Figure 49 - Dynamic light scattering for non-functionalized iron oxide (Fe <sub>3</sub> O <sub>4</sub> ) nanoparticles.....   | 71 |
| Figure 50 – Impact of the magnetic field on the glycerol contact angle for sisECM + 0.2% Fe <sub>3</sub> O <sub>4</sub> nanoparticles bioink. ....  | 72 |

## List of Tables

|  |                                     |
|--|-------------------------------------|
| Table 1 - Characteristics of the most commonly used bioprinted techniques .....  | 5                                   |
| Table 2 - Impedance definition, frequency dependence and phase shift of resistors and capacitors. ....   | 11                                  |
| Table 3 – Structure, advantages, disadvantages, and examples of applications of the main synthetic polymers used in bioprinting. ....  | <b>Error! Bookmark not defined.</b> |
| Table 4 - Conductive hydrogels for cell experiments in current literature. ....  | 20                                  |
| Table 5 - Differences between mature and immature cardiomyocytes. ....   | 24                                  |
| Table 6 - All PEDOT:PSS concentrations tested and respective gelation outcome .....  | 32                                  |
| Table 7 - Overall dimensions for the different geometries used for bioprinting .....   | 35                                  |
| Table 8 - Printed structures attributes and the intervals they were varied to achieve optimal conditions....   | 35                                  |
| Table 9 - Printed structures attributes used for mouse fibroblasts' bioprinting. ....  | 39                                  |
| Table 10 - Different PEDOT:PSS and sisECM concentrations in final hydrogel tested; parameters classification scale: 1 – discarded; 2 – acceptable; 3 – ideal. ....                                     | 41                                  |
| Table 11 - Circularity values for sisECM, sisECM + 0.05%PEDOT:PSS and sisECM+0.1%PEDOT:PSS for days 0 and 30 of the stability assay for the casted structures. ....                                    | 43                                  |
| Table 12 - Printing attributes for sisECM + 0.1% PEDOT:PSS bioink; results before and after gelatin removal. ....  | 50                                  |
| Table 13 - Printing speeds and dispensing pressures optimization for sisECM + 0.1% PEDOT:PSS bioink; circular geometry (r=5mm). ....   | 51                                  |
| Table 14 - Results for wall thickness and pore diameter for each bioink, as well as their respective deviations to the intended dimensions. ....   | 54                                  |
| Table 15 - Bioink formulation for fibroblasts bioprinting.....   | 62                                  |
| Table 16 - Bioink formulation for fibroblasts bioprinting after sisECM concentration adjustments.....  | 65                                  |
| Table 17 - Different alginate and gelatin concentrations and proportions in final hydrogel tested; parameters classification scale: 1 – discarded result; 2 – acceptable; 3 – perfect result. ....     | 67                                  |
| Table 18 - Printing parameters for the 2.5%-7.5% alg-gel bioink and respective results. ....   | 68                                  |
| Table 19 - Printing parameters for the 2.5%-7.5% alg-gel, 2.5%-7.5% alg-gel+0.05% PEDOT:PSS and 2.5%-7.5% alg-gel+0.1% PEDOT:PSS bioinks and respective results.....                                   | 69                                  |
| Table 20 - Results for wall thickness, pore diameter and pore factor for each bioink, as well as their respective deviations to the intended dimensions. ....  | 69                                  |
| Table 21 - Different iron oxide magnetic nanoparticles concentrations in final sisECM hydrogel tested; parameters classification scale: 1 – discarded result; 2 – acceptable; 3 – perfect result. .... | 73                                  |

## List of Abbreviations

CVDs – cardiovascular diseases

MSCs – Mesenchymal Stem Cells

CMs – Cardiomyocytes

hiPSC-CMs - Human Induced Pluripotent Stem Cells – Cardiomyocytes

hiPSCs - human induced pluripotent stem cells

CAD – computer aided design

FDM - Fused-deposition modeling

FRESH – freeform reversible embedding of suspended hydrogels

ECM – extracellular matrix

HA - Hyaluronic acid

GelMA - gelatin methacryloyl

PAAm – Polyacrylamide

PVA – Polyvinyl alcohol

PEG - Polyethylene glycol

PCL - poly-caprolactone

dECM - Decellularized extracellular matrix

NPs – nanoparticles

PPy – polypyrrole

PANi - polyaniline

PT - polythiophene

PEDOT - poly(3,4-ethylenedioxythiophene)

PEDOT:PSS - poly(3,4-ethylenedioxythiophene) polystyrene sulfonate

PLLA - Poly(Lactide)

PVDF - Poly(vinylidene fluoride)

PVDF-TrFE - Poly(vinylidene fluoride-trifluoro ethylene)

PHB - Poly hydroxy butyrate

HA - Hydroxyapatite

BT - Barium titanate

LN - Lithium niobate

BNNT - Boron nitride nano tubes

FF - Diphenylalanine

PBS – phosphate buffer solution

NB – neutralization buffer

DI – Deionized

RPM – rotations per minute

sisECM – small intestine submucosa ECM

EIS – electrochemical impedance spectroscopy

DMEM – Dulbecco's Modified Eagle Medium  
E8 – Essential 8 media  
ROCKi – rho kinase inhibitor  
TE – tissue engineering  
PEGDMA - poly(ethylene glycol) dimethacrylate  
Car-MA - methacrylated κ-carrageenan  
MA - methacrylic anhydride  
EDTA – Ethylenediamine tetraacetic acid  
EGTA – Ethylene glycol tetraacetic acid  
CHAPS – (3-((3-cholamidopropyl) dimethylammonio)-1-propanesulfonate)  
TBP - TATA binding protein  
PERV - porcine endogenous retrovirus  
hCPCs - human cardiac progenitor cells  
hTMSCs – human turbinata mesenchymal stromal cells  
VEGF – Vascular endothelial growth factor  
dtECM – decellularized tendon extracellular matrix  
mdECM – muscle decellularized extracellular matrix  
GO – graphene oxide  
PSS - Polystyrene sulfonate  
MA-CS - methacrylated chondroitin sulfate  
PL – platelet lysate  
EMF – external magnetic field  
bFGF – basal fibroblast growth factor  
NOM - nasal olfactory mucosa  
MNP – Magnetic nanoparticles  
HBSS - Hanks' Balanced Salt Solution  
HEPES - (4-(2-hydroxyethyl)-1-piperazineethanesulfonic acid)  
BTS - N-Benzyl-p-toluenesulphonamide  
FBS - Fetal Bovine Serum  
PFA – paraformaldehyde  
U – uniformity factor  
R – Resistance  
C – Capacitance  
Pr – pore factor  
EHS - Engelbreth-Holm-Swarm  
RPMI - Roswell Park Memorial Institute  
TEM - Transmission electron microscopy  
DLS - dynamic light scattering

# Chapter 1 - Introduction

Tissue engineering (TE) is an interdisciplinary field where principles of life sciences are applied to materials engineering to restore, maintain, and enhance tissue function, and has become the main process involved in the development of novel strategies for organ regeneration<sup>1</sup>. In physiological conditions, cells are organized in a complex three-dimensional (3D) microenvironment that allows the interaction between different cell types and between the cells and the extracellular matrix (ECM). TE allows the production of 3D models that can better mimic the in vivo tissue and organ conditions, using a wide variety of cells, biomaterials, growth factors and other supporting components to create functional constructs. The design of 3D engineered tissue models is currently in its development stage, showing high potential in overcoming the limitations of already available models. However, despite the many technologies that have been introduced, a limitation in biocompatibility, control precision and controllability have hindered the progress in TE. 3D bioprinting has emerged among all other methods for producing tissue scaffolds to bridge the divergence between artificially engineered tissue constructs and native tissues<sup>2,3</sup>.

## 1.1. 3D Bioprinting

### 1.1.1. Brief introduction to 3D bioprinting

Bioprinting has been defined in the literature as a *“computer-aided transfer processes for patterning and assembling living and nonliving materials with a prescribed layer-by-layer stacking organization in order to produce bio-engineered structures serving in regenerative medicine and other biological studies”*<sup>4</sup>. This technique is currently transforming the field of tissue engineering as it allows the manufacturing of complex structures with living cells in a 3D environment, mimicking more accurately the hierarchy of organs and tissues.

These 3D organ-like structures could be applied in regenerative medicine, an interdisciplinary field of research and clinical applications focused on the repair, replacement or regeneration of cells, tissues and organs, using a combination of approaches such as gene therapy, stem cell transplantation, use of small molecules, tissue engineering and reprogramming of cell and tissue types<sup>5,6</sup>. Comparing with traditional methods, 3D bioprinting allows for the direct deposition of biomaterials that are encapsulated with cells or loaded with cells afterwards, in micrometer scale to form structures comparable to native tissue.

**3D bioprinted organs:** The use of these 3D structures allows for the design of a perfect replica of the patient's organs, using patient specific cells that make these printed organs genetically compatible, eliminating the rejection risk. Also, the need for organ donors and associated waiting lists would be reduced. Lastly, 3D bioprinting is a fast, efficient, replicable, and cost-effective approach that can be used in emergency situations (like natural disasters) to bioprint structures like bones or skin, without the need to transport patients<sup>7,8</sup>. However, there are some limitations to the use of 3D bioprinting of organs. One of the biggest limitations associated with

this technology is the lack of printable materials with all-inclusive properties desired for the construction of the bioprinted tissues, especially due to the complexity and variability among different tissues and organs with regard to their structural and physiological requirements<sup>9</sup>. Also, the construction of *in vitro* large-size organs is still limited by the inability to achieve effective microvasculature, and so nutrient supply to cells in the interior section of the bioprinted organ is difficult<sup>10</sup>. A human heart was successfully bioprinted using an alginate based bioink to create a low-cost, high print fidelity, mechanically tunable and suturable model<sup>11</sup>. On another study, aortic valve conduits were microextrusion-bioprinted with two cell types, smooth muscle cells and aortic valve leaflet interstitial cells<sup>12</sup>, using an alginate and gelatin bioink, where cells remained viable over 7 days in culture. A cartilage substitute was produced using an inkjet bioprinting system, by bioprinting poly(ethylene glycol) dimethacrylate (PEGDMA) with human chondrocytes, and successful cartilage construct implantation was achieved on an osteochondral plug<sup>13</sup>.

**3D bioprinted drug screening platforms:** 3D bioprinting also allows the bioprinting of structures for the creation of disease models and cytotoxicity detection platforms for drug and cosmetic testing, as well as for personalized medicine, where pharmaceuticals could be tested in bioprinted patient specific tissue. This allows the elimination of preclinical animal testing, and the creation of disease models that better recapitulate the complexity of human metabolism<sup>14</sup> and lowering the cost of taking a drug to market. So, 3D bioprinting enables the standardized production, parallelization, and application of tailored-designed human tissue, allowing the monitorization of tissue-specific physiologic drug responses, such as the reorganization of micro vessels or cell death, that can be imaged by fluorescence microscopy or via luminescence-based reporters. This is important to measure drug efficacy on the target tissue, but also to assess direct 'real-time' drug-conversion, generation of by-products or cytokine expression, which is almost impossible in experimental tests performed on animals<sup>15</sup>. So far, cardiac cells have been printed on a chip and connect to a bioreactor before using it to test the cardiac toxicity of doxorubicin, a well-known cancer drug, and it was shown that exposure to this drug led to a significant decrease in the cells beating rate<sup>16</sup>. The bioprinting of human liver tissue, comprised of patient-derived hepatocytes and non-parenchymal cells in a defined architecture, allowed for the assessment of trovafloxacin, a drug whose hepatotoxic potential could not be assessed by standard pre-clinical models, that induced significant, dose-dependent toxicity at clinically relevant doses<sup>17</sup>. Successfully bioprinted reconstituted glioblastoma tumors, consisting of patient-derived tumor cells, vascular endothelial cells and decellularized extracellular matrix from brain tissue, was able to reproduce clinically observed patient-specific resistances to treatment with concurrent chemoradiation and temozolomide, and the model can be used to determine drug combinations associated with superior tumor killing capabilities<sup>18</sup>. Alginate hydrogels were inkjet bioprinted to create 3D ring structures with encapsulated human induced pluripotent stem cells and embryonic stem cells-derived hepatocyte like cells, and the cell laden alginate droplets were exposed to calcium chloride solution followed by barium chloride before

incubating in culture medium and examined for the presence of hepatic markers to validate the compatibility of the valve-based bioprinting process with fragile cell transfer<sup>19,20</sup>.

**3D bioprinted hiPSCs:** The advances of bioprinting are closely linked to the achievements of tissue engineering. The discovery of human induced pluripotent stem cells (hiPSCs) was very important in the field because they represent an unlimited cell source for tissue regeneration and the study of human disease. 3D bioprinting has been successfully performed using multiple stem cell types of different lineages and potency. On a study, extrusion-based bioprinting of hiPSCs within an alginate/chitosan/agarose bioink was performed, with post-printing cross-linking in calcium chloride, and the maintenance of pluripotency was demonstrated by the expression of markers of the three germ layers<sup>21</sup>. Also, bioprinting of iPSCs co-cultured with irradiated chondrocytes in a bioink composed of nanofibrillated cellulose with alginate was successfully performed, and pluripotency and cartilaginous tissue was maintained over five weeks<sup>22</sup>. On another study, hiPSC-derived cardiomyocytes and hepatocytes were bioprinted using photocrosslinkable dECM bioinks, and the printed cells maintain high viability and maturity<sup>23</sup>. These few examples demonstrate the versatility of tissues that can be produced in vitro, which combined to the capabilities of 3D bioprinting has the potential to tackle the current limitations in tissue engineering.

In our case, the aim of our work is to develop an electroconductive extracellular matrix bioink, for extrusion bioprinting with potential applications in cardiac tissue engineering. A detailed overview of the objectives presented in this work can be seen in Section 1.6.

### 1.1.2. The bioprinting process

This bioprinting process is divided into three sequential technological steps: preprocessing, processing (printing), and postprocessing (Figure 1)<sup>24,25</sup>.

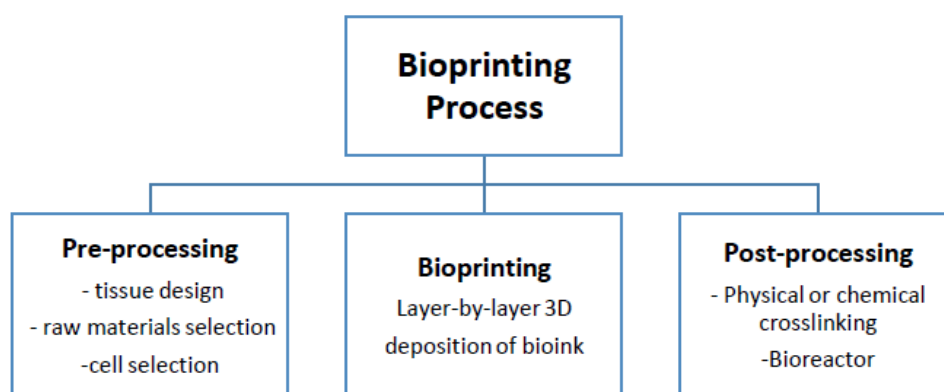


Figure 1 - Steps in the bioprinting process

- Preprocessing: before starting the bioprinting process, it is required to design the structures that will be manufactured. For this, the blueprint of a tissue or an organ is generated using computer-aided design (CAD) techniques. Once this blueprint is designed, the actual printing is processed through a bioprinter. Also, the bioinks' materials and cell type are chosen.



- Processing (bioprinting): Different bioprinting techniques can be used, exhibiting different advantages and limitations and careful consideration should be done to select the most appropriate technique. A summary of the most used techniques in bioprinting will be presented in the following section.

- Post-processing: Depending on the printing techniques and materials used, structures can undergo a post-process to ensure the formation of a mechanically stable and functional structure from printed materials. Some post-processing techniques include temperature, UV radiation or ionic or enzyme-driven crosslinking. In some cases, the bioprinted constructs are subjected to a process of tissue remodeling and maturation performed in bioreactors. This is the most critical and challenging step because shape fidelity and mechanical stability need to be ensured.

After these steps, the structure, morphology, and functionality of the printed construct are evaluated using different tests and machines. Finally, the tissue becomes ready to be used in vitro as a drug testing platform or in vivo as engraft.

## 1.2. 3D bioprinting techniques

Bioprinting techniques range from microextrusion bioprinting and inkjet bioprinting to laser-assisted bioprinting. A brief description of these techniques can be seen in Table 1. However, in this work, extrusion bioprinting was selected due to its ease of use, suitability to the biomaterial to be printed (ECM) and high cells densities resulting in high cell viability. Therefore, more emphasis will be given to this technique in the following sections.

### 1.2.1. Extrusion bioprinting

Extrusion bioprinting is one of the 3D printing methods that has received most interest in the world of tissue engineering and biofabrication. In this technique a bioink is extruded through a dispenser when an external force is applied, either a mechanical force (through screw or piston inserted in the printing barrel), or pneumatically (via a gas or pressurized air). A detailed description of the different types of dispensers can be seen in Figure 2. In our case, the printer we will be using in this work uses a pneumatically-driven system and has the main advantage that inks with various viscosities (in the range of  $30 - 6 \times 10^7$  mPa.s) can be used.

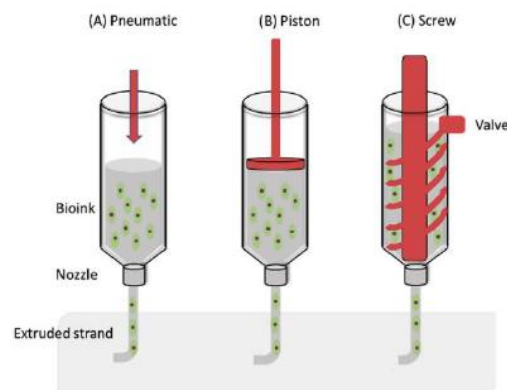


Figure 1 - Schematic diagram of extrusion-based bioprinting pneumatic and mechanical methods: (A) Pneumatic via pressurized air, (B) Piston-driven mechanical extrusion and (C) Screw-driven mechanical extrusion.

Table 1 - Characteristics of the most commonly used bioprinted techniques

|                                  | Extrusion   | Inkjet  | Stereolithography  | Laser-assisted  |
|----------------------------------|---|---|--|---|
| <b>Advantages</b>                | Simple, capable of printing various biomaterials  | Low risk of contamination <sup>26</sup>   | Nozzle-free technique, printing time independent of complexity <sup>27</sup>   | deposition of biomaterials in solid or liquid phase; ability to print constructs of small dimensions <sup>26</sup>  |
| <b>Disadvantages</b>             | Only applicable for viscous liquids   | high viscosity materials and high cell density can cause clogging; low mechanical stability <sup>26</sup><br>Inherent inability to provide a continuous flow, poor functionality for vertical structures  | evaporation of the bioink;<br>shock-absorbing mattress of hydrogel is required to absorb the mechanical shock of the printed cells <sup>28</sup>   | Thermal damage; long fabrication time leads to cell deposition on the bioink <sup>26,29</sup>   |
| <b>Speed</b>                     | Slow (700 mm s <sup>-1</sup> –10 μm s <sup>-1</sup> ) <sup>30</sup>   | Fast (100 000 droplets s <sup>-1</sup> )  | Fast (200–1600 mm s <sup>-1</sup> )  | Medium (200–1600 mm s <sup>-1</sup> )   |
| <b>Cost</b>                      | Moderate  | Low   | Low  | High  |
| <b>Cell viability</b>            | ~90%  | 80-95%  | >90%   | <85%  |
| <b>Cell Density<sup>31</sup></b> | High  | Low   | Medium   | Medium  |
| <b>Resolution</b>                | 200–1000 μm   | 10–50 μm  | 3–200 μm   | 10–100 μm   |
| <b>Viscosity</b>                 | 30 - 6x10 <sup>7</sup> mPa.s  | <10 mPa.s   | No limitation  | 1-300 mPa.s   |
| <b>Examples</b>                  | osteocondral tissue-mimetic structures composed of two compartments, osteoblast-encapsulated Collagen-1 hydrogels and chondrocyte-encapsulated hyaluronic acid hydrogels, with maintained viability and functions up to 14 days in culture; alginate-based bioinks were shown to be capable of modulating proliferation and spreading of hADSCs without affecting the structure integrity of lattice structures after 8 days in culture <sup>32</sup> . | spatially defined patterns of immobilized growth factors were bioprinted to direct cell fate towards osteogenic or myogenic cells simultaneously on the same chip; <sup>33</sup><br>bioprinted NSCs embedded in a thermoresponsive, water-based polyurethane bioink was used to demonstrate the fabrication of bioactive scaffolds without a crosslinking agent <sup>34</sup> | PEGDA-GelMA hydrogel with eosin Y based photoinitiator, containing NIH 3T3 fibroblasts was bioprinted and produced a highly vertical 3D structure with high cell viability for at least five days <sup>27</sup> ;<br>PEGDA hydrogels were supplemented with alginate and cured by an UV LED crosslinking , with porcine aortic valve interstitial cells seeded within these scaffolds and cultured in vitro at physiologic conditions for 21 days, showing high cell viability <sup>35</sup> | patterning of co-culture of HUVEC and hMSC onto a disk of polyester urethane urea, suggesting that patterning may favor faster vasculogenesis and grafting <sup>36,37</sup><br>bioprinting of MG63 cells and electrospun PCL biopapers on a layer-by-layer sandwich model <sup>38</sup> |

ADSCs - Adipose tissue-derived stem cells; NSCs – neural stem cells; PEGDA - polyethylene glycol diacrylate; GelMA - gelatin methacrylate; HUVEC - human umbilical vein endothelial cells; MSC – mesenchymal stem cells; PCL – polycaprolactone

Extrusion bioprinters are compatible with multiple materials with an extensive range of viscosities (0.3 Pa.s for collagen I-alginate bioink and 4000 Pa.s for gelatin-alginate bioink<sup>39</sup>, for example) and bioinks with high cell densities ( $>10^8$  cells/mL). The resolution of this technique is in the order of 200–1000  $\mu\text{m}$  and careful control over shear stress is required to minimize cell death. Shear stress is defined as the mechanical force induced by the friction of liquid against the cell membrane and is unavoidable in all dispensing bioprinting techniques, being directly linked to cell viability. When bioprinting, the bioink is pressurized to move through the nozzle with a specific diameter and geometry, where cells experience different velocity gradients – cells near the wall of the nozzle experience the maximum velocity gradient and shear stress, leading to greater cell deformation and potential cell death. Mechanisms to avoid excessive shear stress forces involve controlling material properties, where an optimal bioink should have a low viscosity under extrusion induced shear stress, but increased viscosity after printing to achieve high shape fidelity and cell viability, and printing parameters, where needle geometry and dispensing pressure should be taken into account.

### **1.2.2. FRESH extrusion bioprinting**

Printing with low viscosity materials is challenging in traditional extrusion bioprinting because the materials need to be relatively viscous, otherwise the bioprinted structures will have low print resolution or even 3D self-standing structures will not be possible to print. While current 3D printing techniques can produce full-size adult organ models, the materials used generally do not mimic the mechanical properties of native tissue. A solution can be the rheological modification of the materials used for the bioinks or to impart a yield stress so that they maintain their shape during the printing process<sup>40</sup>.

To address this challenge, freeform reversible embedding of suspended hydrogels, also known as the FRESH method, was developed. The main difference with conventional extrusion bioprinting is that materials are extruded inside a thermo reversible gelatin-slurry microparticle support bath, used as a sacrificial material<sup>41</sup>. This support bath maintains the shape of the structures until they have gelled/crosslinked and can support multiple independent crosslinking strategies, such as pH changes, divalent cations, and UV, to gel different hydrogels and other soft polymeric materials. FRESH printing within the support bath effectively mitigates the effects of gravity by embedding the printed material, allowing for freeform printing of delicate, unsupported structures that would immediately collapse in air<sup>42</sup>. At the end of the printing process, the sacrificial material is removed. A schematic of this process is represented in Figure 3. The bioinks used with FRESH usually have low viscosities and are liquid-like and must be gelled or crosslinked *in situ*.

Multiple organ-like structures were manufactured using this method by several research groups. A research group has scaled down the model of a human femur, that was FRESH printed in alginate, with shape-fidelity and easy handling successfully achieved. The same group developed a model of a section of a human right coronary arterial tree and FRESH printed it with alginate bioink in a gelatin slurry support bath with great success<sup>43</sup>. On another study,

vascularized, and perfusable cardiac patches that completely match the immunological, cellular, biochemical, and anatomical properties of the patient were reported. The authors used a bioink comprised of decellularized omentum and iPSC derived CMs or neonatal rat cardiac cells that was bioprinted in a gelatin supporting bath<sup>44</sup>. The 3D printing of a muscle construct was also reported<sup>45</sup>. Here, a bioink of decellularized extracellular matrix of skeletal muscle and vascular tissues mixed with human skeletal muscle cells was FRESH bioprinted in a gelatin support bath. In this work, a FRESH extrusion bioprinting method will be used because the bioink chosen – extracellular matrix is the main component – is extremely liquid (water-like), with low viscosity, that undergoes polymerization at 37°C, where its viscosity increases and bioprinted constructs are self-standing.

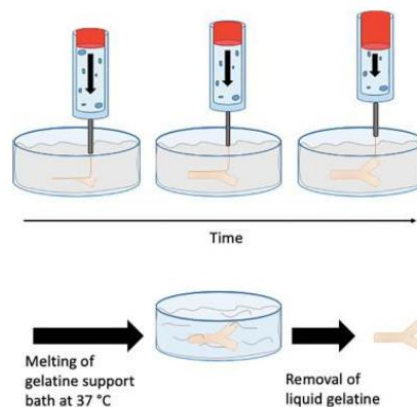


Figure 3 - FRESH-printing method: A microgel gelatin-support bath is used for printing low viscosity materials. The gelatin can be removed post-printing by heating to 37 °C.

### 1.3. Hydrogel and bioink characterization for extrusion bioprinting

As stated before, extrusion based bioprinting allows for the printing of hydrogels of varying viscosities and large-scale constructs (cm scale) with high cell densities, though with limited resolution. The varied bioink formulations, crosslinking mechanisms and the use of sacrificial materials, as well as printing parameters control can be varied to achieve optimal print quality and cell viability. On the following section, a detailed overview on bioink rheological, electrochemical and printability characterization is described.

#### 1.3.1. Rheological Properties

In extrusion bioprinting, fluid is dispensed and pushed through a nozzle. The normal force exerted by the downward motion of the plunger induces a rheological response from the bioink, which determines its flow through the nozzle. The flow response of a bioink is vital while developing and screening bioinks.

##### 1.3.1.1. Storage and loss modulus

Some polymers have a viscoelastic behavior, that refers to the fact that a polymeric fluid can exhibit a response which resembles that of an elastic solid under some circumstances, while under others it can act as a viscous liquid<sup>46</sup>. The viscoelastic behavior of most polymers

involves both a long-time retarded response and a phase shift  $\delta$  in rapid dynamic response. It can be separated in two parts: the storage modulus ( $G'$ ) and the loss modulus ( $G''$ ), in Pa, Figure 4.

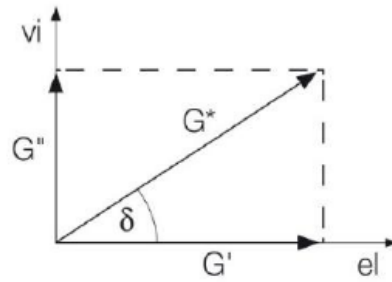


Figure 4 - Vector diagram illustrating the relationship between complex shear modulus  $G^*$ , storage modulus  $G'$  and loss modulus  $G''$  using the phase-shift angle  $\delta$ .

The loss modulus  $G''$  characterizes the viscous portion of the viscoelastic behavior (liquid-state behavior of the sample) and characterizes the deformation energy lost through internal friction when flowing. The viscous behavior arises from the internal friction between molecules and particles in a flowing fluid, that always goes along with the development of frictional heat in the sample, and consequently, with the transformation of deformation energy into heat energy. This part of the energy is absorbed by the sample; it is used up by internal friction processes and is no longer available for the further behavior of the sample material. This loss of energy is also called energy dissipation. In contrast, the storage modulus  $G'$  represents the elastic portion of the viscoelastic behavior (solid-state behavior of the sample) and represents the stored deformation energy. This energy is stored in the deformed material with stretching or destroying the material. When the material is later released, this unused stored energy acts like a driving force for reforming the structure into its original shape<sup>47</sup>. For viscoelastic solids,  $G' > G''$ , due to chemical bonds or physical-chemical interactions inside the materials. On the other hand, in viscoelastic liquids with  $G'' > G'$  there are no such strong bonds between the individual molecules, which represents a mechanically inferior system incapable of providing high-definition post extrusion.

On a bioink for extrusion bioprinting, initially the loss modulus is higher than the storage modulus, so that the bioink behaves like a solution and is able to be extruded without compromising cell integrity. After printing and undergoing polymerization/gelation, the opposite needs to happen, where storage modulus needs to be higher than loss modulus, and the biomaterial is gel-like. The point at which the biomaterial transitions from a sol to a gel is called gel point and can be found by the intersection of the storage and loss moduli curves.

#### 1.3.1.2. Viscosity

In bioprinting, viscosity is the resistance of a bioink to a deforming force. High viscosity bioinks are readily extruded and can retain shape following extrusion. However, they require high deforming forces during extrusion, which can harm encapsulated cells. Low viscosity bioinks can minimize nozzle-clogging and enable mixing of cells but cannot maintain shape following extrusion resulting in poor feature definition. It is also possible to define a complex viscosity  $\eta^*$ ,

which is a measure of the total resistance to flow as a function of angular frequency ( $\omega$ ) and is given by the quotient of the maximum stress amplitude and maximum strain rate amplitude<sup>48</sup>.

On a bioink for extrusion bioprinting, complex viscosity should be low before bioprinting, as it should have a liquid-like behavior, and consequently less resistance to flow. After printing, complex viscosity should increase as the biomaterial suffers gelation, becoming gel-like and resistance to flow should increase.

#### 1.3.1.3. Loss factor or damping factor

The loss factor ( $\tan \delta$ ) is defined as the ratio of  $G''$  to  $G'$  and is used to characterize the stability of materials. The loss factor provides useful information about the state of crosslinking and the stability of a material system. The loss factor  $\tan \delta$  can be plotted in addition to the curves of  $G'$  and  $G''$ , in particular if there is a phase transition in the sample, the gel point. For ideal elastic behavior,  $\delta = 0^\circ$ , meaning that there is no viscous portion. Therefore,  $G'' = 0$  and with that  $\tan \delta = G''/G' = 0$ . On the other hand, for ideally viscous behavior  $\delta = 90^\circ$  and there is no elastic portion. Therefore,  $G' = 0$  and the value of  $\tan \delta = G''/G'$  approaches infinity.

A liquid can be classified as ideally viscous if  $\tan \delta > 100:1 = 100$ , while a solid material is called ideally elastic if  $\tan \delta < 1:100 = 0.01$ . Some authors have investigated the correlation between the loss factor, extrudability, and printability. According to them, bioinks with  $\tan \delta$  greater than 1 have no shape retention. When  $\tan \delta$  is between 0.6 and 1, there is poor shape retention. When  $\tan \delta$  falls between 0.4 and 0.6, there is good extrudability and shape retention, and inks having  $\tan \delta$  values less than 0.4 were not extrudable<sup>49</sup>.

### 1.3.2. Extrusion Parameters

The variation in extrusion parameters directly affects the printing outcome. Below are described some of these parameters.

#### 1.3.2.1. Pressure

Most extrusion bioprinting processes use a pneumatic system to dispense bioinks through nozzle, using compressed air to aid adequate extrusion. Printing pressure needs to be optimized to initiate the generation of continuous filaments during extrusion. Low pressure can result in insufficient extrusion and cause discontinuities in the printed lines. Too high pressures can result in unstable flow, leading in structures with poor resolution.

#### 1.3.2.2. Temperature

Temperature control is crucial since it influences rheological properties of the bioink. So, determining the optimal printing temperatures is essential to obtaining smooth extrusion and deposition. Also, cells are thermosensitive, and so temperature control is an important factor in maintaining cell viability. Additionally, some commonly used temperature-sensitive biomaterials include gelatin, collagen, GelMA<sup>49</sup>.

### 1.3.2.3. Speed

The speed at which the nozzle moves during deposition determines the geometrical characteristics of the deposited filaments. The print speed of the nozzle is chosen to approximately match the velocity of bioink flowing out of the nozzle. As extrusion pressure increases, the flow rate of ink through the nozzle increases, and the print speed must increase as well. If the print speed is higher than the velocity of ink exiting the nozzle, then the extruded filament is elongated and may result in discontinuities or inferior mechanical properties. If the print speed is below the velocity of ink, then the ink spreads laterally to produce wider printed lines and resolution is poor.

### 1.3.3. Electrochemical properties

Electrical Impedance spectroscopy (EIS) is a powerful method to analyze the complex electrical resistance of a system and is sensitive to surface phenomena and changes of bulk properties. It can reveal details regarding the conduction mechanism in a complex system such as the hydrogel. Using EIS, the cellular responses in bulk artificial and biological tissues have been studied, including the development of cell layers, the electrical properties of porcine tissues, the impedance of tofu and the impedance of viable zebra fish embryos<sup>50</sup>.

The impedance  $Z$  of a system is determined by applying a voltage perturbation of small amplitude and detecting the current response. From the definition, impedance is the quotient of the voltage-time function  $V(t)$  and the resulting current-time function  $I(t)$ , equation 1.

$$Z = \frac{V(t)}{I(t)} \quad (1)$$

The impedance is a complex value since the current can not only differ in the amplitude (as in the case for a pure resistance) but can also show a phase shift  $\varphi$  compared to the voltage-time function (as in the case of capacitive or inductive resistances). Measuring the amplitude and phase difference provides information pertinent to the speed at which ions move in the conducting sample. Impedance can be described either by the modulus  $|Z|$  and the phase shift  $\varphi$  or alternatively by the real part  $Z_R$  and the imaginary part  $Z_I$  of the impedance, Figure 5. The name impedance “spectroscopy” is derived from the fact that usually not only a single frequency is measured but impedance is determined at different frequencies, resulting in an impedance spectrum that allows the characterization of surfaces, layers or membranes as well as exchange and diffusion processes. The circuit analyzed, commonly consisting of resistances and capacitances, represents the different physico-chemical properties of the system under investigation<sup>51</sup>.

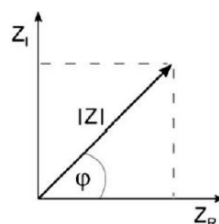


Figure 5 – Impedance can be expressed as modulus  $|Z|$  and phase angle  $\varphi$  or can be given by the real part ( $Z_R$ ) and the imaginary part ( $Z_I$ ) of impedance.

In EIS, where the electrolyte solution is one component of the system to be investigated, two major elements are used for the description of the impedance behavior: resistance and capacitance. A resistance,  $R$ , appears in the impedance spectrum when charge carriers are transported within the bulk of a material, through thin layers or across interfaces. A resistance causes no phase shift between the ac voltage and the ac current, and the impedance value is independent of the frequency used for the measurement. This means the impedance is constant over the whole frequency range. A capacitance,  $C$ , appears when charge carriers are separated at interfaces or at membranes or films. A capacitance results in a phase shift of  $-90^\circ$  of the current-time function compared to the applied voltage function and the impedance is strongly dependent on the frequency of measurement. Particularly at low frequencies the capacitive impedance becomes very high. A summary of the resistor and capacitor is in Table 2<sup>52</sup>.

Table 2 - Impedance definition, frequency dependence and phase shift of resistors and capacitors.

| Component | Current Vs. Voltage | Impedance         | Phase Shift | Frequency Dependence |
|-----------|---------------------|-------------------|-------------|----------------------|
| resistor  | $E = IR$            | $Z = R$           | $0^\circ$   | No                   |
| capacitor | $I = C \, dE/dt$    | $Z = 1/j\omega C$ | $90^\circ$  | Yes                  |

#### 1.4. Bioinks for 3D FRESH extrusion bioprinting

One of the main challenges in the fabrication of organs or tissues through using 3D printing technology is to mimic the mechanical, chemical, and morphological properties of in vivo structures. These aspects can be controlled through the bioink composition, where the main requirements are:

- Printability: the material chosen should be easily handled and extruded by the bioprinter, with appropriate viscosity, gelation methods and rheological properties taken into account.
- Biocompatibility: the materials and the degradation of byproducts should be nontoxic; materials should demonstrate suitable swelling or contractile characteristics.
- Structural and mechanical properties: the materials should be chosen based on the required mechanical properties of the construct, ranging from rigid thermoplastic polymer fibers for strength to soft hydrogels for cell compatibility to achieve the desired structural and functional characteristics.

The materials that most closely fulfill these characteristics are hydrogels, 3D networks formed by molecular chains embedded in a water-rich environment. Hydrogels can be formed using several crosslinking mechanisms, show tunable physicochemical properties and high biomimicry of the native tissues' ECM, and allow cell encapsulation in a highly hydrated, mechanically supportive 3D environment similar to that in many natural tissues<sup>53</sup>. In addition,



hydrogels can be further modified with chemically and biologically active recognition cues such as stimuli-responsive molecules and growth factors (GFs) that enhance their biofunctionality.

The polymers for hydrogels can be classified into natural and synthetic polymers. Natural polymers include alginate, chitosan, hyaluronic acid, gelatin, fibrin, silk and many others, whilst the synthetic polymers include materials such as polyacrylamide (PAAm), polyvinyl alcohol (PVA), polyethylene glycol (PEG), polylactic acid (PLA), and others<sup>54</sup>. Bioactivity, biocompatibility, 3D geometry, antigenicity, non-toxic byproducts of biodegradation, and intrinsic structural resemblance are the most important properties of natural polymers, but their lack of mechanical strength is a major disadvantage. On the other hand, synthetic polymers are characterized by their tunable properties, endless forms, and established structures over natural polymers and their polymerization, interlinkage, and functionality of their molecular weight, molecular structure, physical and chemical features make them easily synthesized as compared to naturally occurring polymers. Depending on the cell type and application, careful selection of the materials is required. A more detailed description of the different types of hydrogels can be seen below.

#### **1.4.1. Natural Polymers**

Natural polymer-based hydrogels have good hydrophilicity, biocompatibility, specific enzymatic degradation and promote cell proliferation and differentiation<sup>54</sup>.

##### **1.4.1.1. Alginate**

Alginate is a polysaccharide formed with blocks of(1–4)-linked  $\beta$ -D-mannuronic acid (M) and  $\alpha$ -L-guluronic acid (G) monomers. This material is frequently used in bioprinting due to biocompatibility with different cell types including articular chondrocytes<sup>55,56</sup>, skeletal myoblasts<sup>57,58</sup>, neural stem cells<sup>59</sup>, and mouse embryonic stem cells<sup>60</sup> and due to its outstanding properties in terms of biodegradability, non-antigenicity and chelating ability. Its rheological properties make it suitable for 3D bioprinting with viscosities in the range of  $\sim 400$  mm<sup>2</sup>/s to  $\sim 3000$  mm<sup>2</sup>/s<sup>32</sup>. The crosslinking method of alginate is based on ionic crosslinking in the presence of various divalent cations, like Ca<sup>2+</sup>, by crosslinking the carboxylate groups of the guluronic acid with the divalent cations and forming tightly held junctions. The limitations of this ink include the limited long-term stability in physiological conditions, because these gels can be dissolved due to release of divalent ions into the surrounding media as a result of exchange reactions with monovalent cations<sup>61</sup>. So, chemical modifications are often required to induce the desirable cellular functions and maintain the 3D printed structure<sup>62</sup>. These include alginate oxidation<sup>32</sup>;  $\gamma$ -irradiation<sup>63</sup>, and combination with other molecules<sup>64</sup>. 3D bioprinted structures with alginate bioinks have been manufactured by other groups, including a polycaprolactone-alginate bioink to create 3D osteochondral tissue constructs<sup>65</sup>, 3D-bioprinted human ears and sheep meniscus using a bioink combining nanofibrillated cellulose and alginate<sup>66</sup>, and vascular-like structures with bifurcations (horizontal and vertical) were printed in sodium alginate and mouse fibroblast-based alginate bioinks<sup>67</sup>.

#### 1.4.1.2. Collagen

Collagen is a major ECM protein obtained from natural sources that has been extensively used in 3D bioprinting. Its crosslinking mechanism is based on changes in temperature and pH<sup>68</sup>. Briefly, when temperature increases above 37 °C, collagen fibrillogenesis process is triggered, consisting on the conversion to peptide bound aldehydes of specific lysine and hydroxylysine residues in collagen, and renders the collagen fibers stable, providing them with an adequate degree of tensile strength and viscoelasticity to perform their structural roles<sup>69</sup>. However, the slow gelation time (at least 30 min at 37 °C) and the low mechanical properties (Young's Modulus of 150-500<sup>70</sup> MPa) are a major barrier for use in 3D printing<sup>62</sup>. Some bioprinted structures using collagen as a bioink include a skin model, that employed keratinocytes and fibroblasts as constituent cells to represent the epidermis and dermis, and collagen was used to represent the dermal matrix of the skin<sup>71</sup>, and a heart valve model, by FRESH bioprinting collagen and rat mesenchymal stem<sup>72</sup> cells.

#### 1.4.1.3. Gelatin

Gelatin is a natural protein that has an amphoteric behavior due to alkaline and acidic amino acids functional groups, and it is derived from collagen hydrolysis. It is extracted from several sources like connective tissues of animals and easily forms hydrogels during cooling, however, the materials are mechanically fragile and thermostability of gelatin is poor (gelatin will become solution due to cleavage of hydrogen bonds when the temperature is above 37 °C) and chemical crosslinking agents that can be poisonous may affect the biocompatibility of gelatin. To improve their properties, they are often chemically crosslinked<sup>73</sup>. For bioprinting, gelatin is commonly used in the form of gelatin methacryloyl (GelMA), through the direct reaction between gelatin and methacrylic anhydride (MA). The resultant groups of this reaction comprise methacrylamide groups and methacrylate groups. The crosslinking of GelMA hydrogels can be achieved by exposing aqueous solution of GelMA prepolymer added with a photoinitiator under both UV and visible light, though the common photoinitiators work within the UV range. However, the usage of UV light may have potential long-term side effects on cells<sup>74</sup>. It was reported the successful bioprinting of a photolabile cell-laden GelMA hydrogel with encapsulated HepG2 cells, with high cell viability after 8 days in culture<sup>75</sup>. Also, scaffolds composed of both GelMA and methacrylated  $\kappa$ -carrageenan (Car-MA) were extrusion bioprinted, with stability over 21 days and mechanical properties comparable to those of native breast tissue, as well as a similar cell viability and proliferation rate after 14 days was obtained for adipose tissue-derived stem cells upon seeding onto the scaffolds<sup>76</sup>.

#### 1.4.1.4. Decellularized extracellular matrix.

The extracellular matrix (ECM), Figure 6, appears as a great candidate for a biomaterial in tissue engineering applications. The extracellular matrix is a complex mixture of collagen fibrils, elastin, macromolecules (glycoproteins), and glycosaminoglycans (GAGs) together with other molecules such as growth factors, cytokines, and extracellular proteases. The ECM provides structural and biochemical support for cell growth and alterations to the ECM influences the cell

state and function<sup>77</sup>. It is essential to maintain tissue structural integrity but also to transduce signals important for homeostasis, which include cell differentiation, migration, proliferation, survival and maturation. In bioprinting, a number of materials have been used for making bioinks although unsuccessfully, due to their poor representation of the complexity of natural ECMs and consequently are inadequate to recreate a microenvironment that is typical of living tissues<sup>62</sup>. Decellularized extracellular matrix (dECM) could be the best choice for doing so, as it can recapitulate all the features of natural ECM.

Decellularized ECM (dECM) materials are extracted from native animal tissues<sup>78</sup> where the cells are removed, usually obtained by chemical, enzymatic, and/or physical decellularization methods<sup>79</sup>, developed to eliminate the cells and their waste, mainly DNA, and the resulting intact ECM is then dried and crushed into a powder<sup>80,81</sup>. For chemical decellularization, treatment with acid/base, Triton X-100, SDS (sodium dodecyl sulphate), Triton X-200, CHAPS (3-((3-cholamidopropyl) dimethylammonio)-1-propanesulfonate), TBP (Tributyl phosphate), and hypertonic and hypotonic solutions are usually used. Chemical methods have to be chosen carefully because of the damage that they may cause to the structural macromolecules of the matrix. Enzymatic reagents include EDTA (Ethylenediaminetetraacetic acid), EGTA (Ethylene glycol tetraacetic acid), trypsin; pepsin; endonucleases and exonucleases: These methods may lead to additional problems related to enzyme removal. Finally, physical treatment includes techniques such as freezing, force, agitation, hydrostatic pressure and vacuum-assisted decellularization, though they do not completely decellularize the ECM and a combination with chemical or enzymatic treatment is needed.

In this way, the mechanical integrity and scaffolding architecture of the ECM remains, with better performance and applicability as implants for tissue repair, and with better mechanical/biochemical properties for the intended use<sup>82</sup>.

Many animals, including pig, cow, goat, and rat, have been used as tissue sources for making ECM hydrogels. However, for the formulation of dECM bioinks, most of the tissues have been obtained from porcine models<sup>83</sup>. Some advantages of porcine ECM over nonhuman primates (significant genetic and evolutionary differences between each other) include availability (pigs have higher breeding potential and shorter reproductive periods with rapid growth), transgenicity, relative organ size and physiological similarities when compared to human and low cost. However, there are some associated risks. Xenotransplantation can cause zoonotic infections to emerge, especially porcine endogenous retrovirus (PERV) and human rejection of porcine antigens.

The resulting bioink is a rich medium with native growth and differentiation factors, which supports the specific functioning of the chosen cell type. In terms of dECM printability, dECM bioinks have a low viscosity<sup>81</sup>. However, despite the cellular benefits of dECM incorporation into bioinks, extraction and processing of the ECM before formulation of the bioink is costly<sup>80</sup>. Also, dECM bioinks are usually softer than most hydrogels, so they need to be either mixed with other crosslinking agents to make them printable in extrusion bioprinting or printed along

biocompatible thermoplastics (such as polycaprolactone) for a mechanically strong scaffold<sup>83</sup>. The slow gelation time (~30 minutes) of the dECM hydrogels also pose as a challenge. Nevertheless, dECM bioinks are providing better microenvironments to support cellular processes and ECM cues.

In a recent study, the 3D bioprinting of a stem cell dECM pre-vascularized cardiac patch to improve the efficacy of the therapy was successful. The bioinks were printed in the presence of human cardiac progenitor cells (hCPCs) and/or (human turbinate mesenchymal stem cells) hTMSCs. Results indicated that cells contained within each bioink remained viable, hCPCs underwent structural maturation and vascular formation by hTMSCs was promoted. The vascular structures formed were shown to be similar in morphology to vascular structures formed by human dermal tissue-derived microvascular endothelial cells. To assess the functional benefits of the dECM patch on tissue repair, the patch was transplanted into the myocardium of a murine MI model. Results revealed that in comparison to the control, a larger quantity of (Vascular endothelial growth factor) VEGF was secreted and less adverse tissue remodeling, and myocardial fibrosis occurred. In addition, the monitored cardiac repair genes were upregulated in the dECM patch group as compared to the MI group. Lastly, cardiac function was improved, and the patch acted as a delivery system for the stem cells<sup>84</sup>. On another study<sup>85</sup>, a bovine Achilles tendon-based dtECM hydrogel was prepared and was tested using encapsulated NIH 3T3 fibroblasts. The results showed that in addition to the good printability of the bioink, the bioink was shown to have no cytotoxic or immunogenic effects on the encapsulated fibroblasts, and cells remained viable and exhibited homogenous distribution throughout the bioink. In addition, lineage-specific cellular morphology and cellular extensions were observed at the third day of culture. The rheology of the bioink indicated, irrespective of the digestion time, increases in dtECM concentration increases storage modulus (see section 1.3.1.1.) before and after hydrogel network formation. Lastly, increasing the dtECM concentration was shown to increase the rate of gel formation and increases both the maximum stress and compressive moduli. Other studies using dECM-based bioinks include the bioprinting of heart, cartilage, and adipose tissue constructs, where heart dECM<sup>86</sup> was mechanically strong enough to be printed independently, but the cartilage and adipose dECM were printed together with PCL frameworks; functional muscle constructs<sup>87</sup> were also obtained after printing C2C12 myoblasts with muscle derived dECM with the help of an extrusion printer; and a special 3D coaxial printing technique was used to fabricate a cell-drug-laden bioblood vessel (BVV)<sup>88</sup>.

In this work, the aim was to develop a dECM-based conductive bioink for tissue engineering, with special interest in cardiac tissue engineering. The ECM 3D framework provides an elastic and supportive environment for cardiomyocyte (CM) electrical impulse propagation and synchronous pump contraction<sup>53</sup>. The CMs are aligned along intertwined collagen and elastic fibers and rest on a matured basement membrane, resulting in a honeycomb-like heterogeneous architecture<sup>53</sup>.

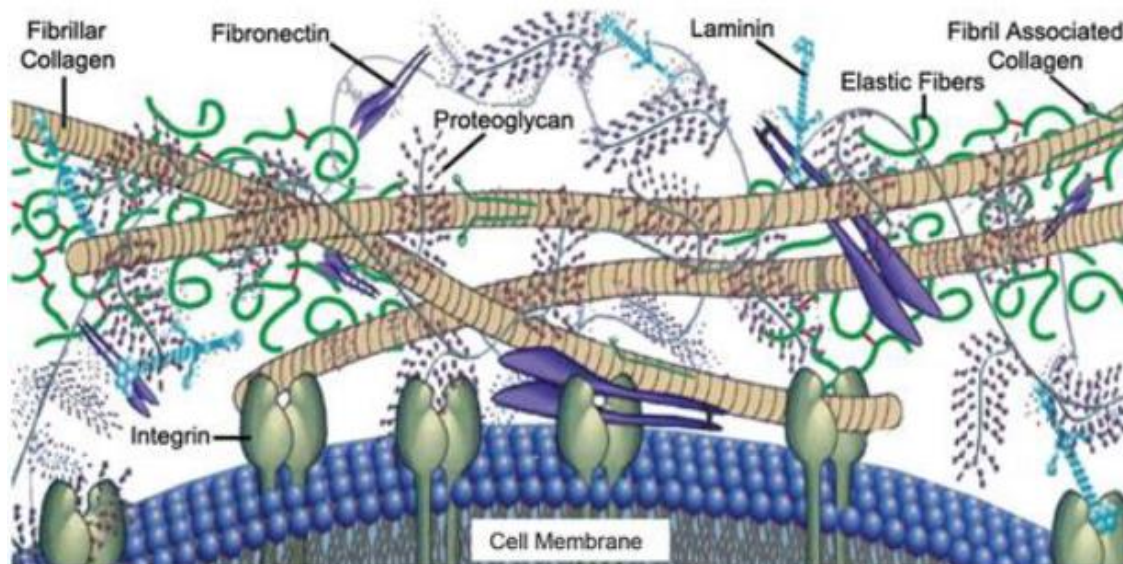
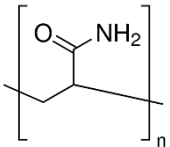
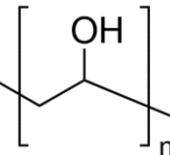
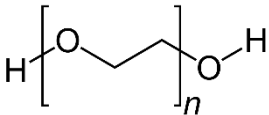
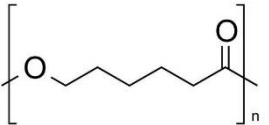


Figure 6 - Scheme of the general ECM space showing some primary ECM components and the interactions between these components and cells.

#### 1.4.2. Synthetic Polymers

Contrary to natural polymers, hydrogels prepared with synthetic polymers have adjustable mechanical and degradation properties and unlimited availability, which is preferred for various kinds of applications such as sensors, contact lenses, artificial organs, and drug delivery systems<sup>89</sup>. Nevertheless, these materials have reduced biocompatibility and may induce cytotoxic responses. Only few synthetic materials with appropriate combination of biodegradability, biocompatibility and mechanical properties without compromising cellular function have been applied to tissue engineering so far<sup>53</sup>. The main synthetic polymers used and the chemical structure of these can be seen in Table 3. Overall, these polymers need to be soluble in water because water plays an important role in determining the physico-chemical properties of the hydrogels. Hydrogels with hydrophilicity can absorb large quantities of water or aqueous solutions. The 3D network is able to retain the liquids forming a swollen gel phase and the liquid prevents the polymer network from collapsing into a compact mass.

Table 3 – Structure, advantages, disadvantages, and examples of applications of the main synthetic polymers used in bioprinting

| Polymer   | Synthesis   | Advantages   | Disadvantages  | Bioprinting Applications   |
|---|---|--|--|--|
| Poly(acrylamide)(PAAm) <sup>89</sup><br> | acrylamide monomer (AAm) and N,N' -<br>methylenebisacrylamide (MBAAm) cross-linker<br>mixed in deionized water  | Water soluble<br>Low toxicity  | de-polymerization to form<br>acrylamide, a neurotoxin<br>and carcinogen    | PAAm- UHMWPE skin-like hydrogel composite <sup>90</sup> ;<br>Alginate-PAAm hydrogel to construct articular-like<br>tissue for cartilage TE <sup>91</sup>   |
| Polyvinyl Alcohol (PVA)<br>              | Low temperature crystallization of a PVA solution in<br>a mixed solvent consisting of water and DMSO <sup>92</sup>  | water-soluble known for<br>its biodegradation<br>capability,<br>biocompatibility and low<br>toxicity <sup>54</sup> | limited biological<br>performance<br>low strength and thermal<br>stability | (PVA)-alginate based hydrogel with MC3T3-E1<br>osteoblast precursor cells <sup>93</sup> ;<br>alginate-PVA-HA hydrogel for 3D bioprinting bone<br>tissue engineered scaffolds with MC3T3 cells <sup>94</sup>  |
| Polyethylene Glycol (PEG)<br>            | anionic or cationic polymerization of ethylene oxide;<br>modified with acrylate or methacrylate groups that<br>allow for hydrogel formation in the presence of<br>initiators by a thermally or photoinitiated<br>polymerization | high biocompatibility and<br>low toxicity;<br>amphipathic behavior   | prone to oxidative<br>degradation <sup>95</sup>                            | Extrusion bioprinting of PEG microgels with<br>mesenchymal stem cells <sup>96</sup> ;<br>micro-capillary based bioprinting of a PEG-based<br>bioink with LMWG fragments <sup>97</sup> .  |
| Poly-caprolactone (PCL)<br>            | polycondensation of a hydroxycarboxylic acid: 6-<br>hydroxyhexanoic acid, and the ROP of epsilon-CL <sup>98</sup>   | good biocompatibility<br>and versatility;  | hydrophobicity   | [PPy-b-PCL] for bioprinting of neural tissue constructs<br>with PC12 cells (derived from a pheochromocytoma of<br>the rat adrenal medulla) <sup>99</sup> ;<br>3D bioprinting of a full thickness skin model with<br>cellular collagen dermal layer that rests on an acellular<br>PCL/collagen scaffold, and is overlaid by sequential<br>extrusion of bioprinted keratinocytes before airlifting for<br>stratification and differentiation dermal fibroblasts <sup>100, 98</sup> |

UHMWPE - Ultrahigh molecular weight polyethylene; HA – hydroxyapatite; LMWG - low molecular weight gelatin; PPy -b-PCL - PPy-block-poly(caprolactone); ROP - ring-opening polymerization; epsilon-CL - epsilon-caprolactone; DMSO - dimethyl sulfoxide

### 1.4.3. Strategies to increase the functionality of hydrogels

There is an increased demand in smart and stimuli-responsive materials to provide additional control over the material's properties and cell fate. Therefore, strategies to increase the functionality of the hydrogels will be key to achieve this. This can be done by incorporation to the hydrogel structure of nano- and microfillers with electrical, piezoelectrical and magnetic properties.

#### 1.4.3.1. Conductive Hydrogels

For applications in the engineering of electrogenic tissues such as cardiac, neural and muscle tissues, conductivity plays an important role in mimicking the electrical conditions of in vivo tissues and can be determinant towards differentiation and functionality.

Conductivity of hydrogels can be increased by addition of metal nanoparticles (NPs), carbon-based materials, and conductive polymers. Table 4 summarizes some already developed examples of conductive hydrogels for cell experiments.

Metallic nanoparticles (NPs) provide a link between bulk materials and molecular or atomic structures. They can be manufactured and modified through utilizing different functional groups that provide conjugation of antibodies, ligands, and drugs as delivery systems<sup>101</sup>, and are attractive for tissue engineering due to their improved electrical conductivity (0.01-0.1 S/cm), magnetic properties and antibacterial properties<sup>99</sup>. The final properties depend on the type of nanoparticles incorporated, which in turn determines the proposed application. Silver (Ag) and gold (Au) are the most commonly used conducting materials for hydrogels<sup>102</sup>. The use of gold for making conducting hydrogel remains limited due to its high cost.

Carbon based materials such as graphene (and derivatives like graphene oxide (GO)) and carbon nanotubes (CNTs) have high biocompatibility, several physical and chemical properties, high surface area and conductivity<sup>99</sup>. Their enhanced electrical properties (conductivity can range from 0.1-1.5 S/cm<sup>102</sup>) are highly attractive, and this shows their potential to be used as reinforcement and additive material for composites and have higher compatibility with cells compared to metal counterparts. This comes from the fact that carbon-based materials can be trapped in synthetic and natural hydrogels, that leads to better biocompatibility. The long-term cytotoxicity of metal nanoparticles (NPs) and carbon-based materials restricts their use in regenerative medicine.

Conductive polymers, on the other hand, are non-biodegradable and possess weak mechanical properties limiting their printability into three-dimensional constructs<sup>60</sup>. Conductive or conjugated polymers are organic polymers which intrinsically conduct electricity. The backbone of these polymers has contiguous sp<sup>2</sup>-hybridized carbon centers, each having a valence electron residing in a p<sub>z</sub> orbital, orthogonal to the other  $\sigma$ -bonds. The  $\pi$  bonds resulting from the combination of these orbitals allow the delocalization of these electrons throughout the polymer backbone<sup>61</sup>. These polymers include polypyrrole (PPy), polyaniline (PANI), polythiophene (PT),

and poly(3,4-ethylenedioxythiophene) (PEDOT). Some examples of conductive hydrogels using some of these polymers are presented in Table 4.

PEDOT in combination with polystyrene sulfonate (PSS) (PEDOT:PSS) shows strong potential in tissue engineering due to its high stability and high electrical conductivity (1–10 S/cm), hence tuning the conducting nature of PEDOT:PSS based hydrogels is a very interesting area to explore<sup>103</sup>. It is a polyelectrolyte consisting of positively charged electrically conducting conjugated PEDOT and negatively charged insulating PSS (stabilizes conjugated polymer cations in water and some polar organic solvents)<sup>104</sup>, Figure 7. It has been increasing its popularity over the years, due to its biocompatibility<sup>105</sup> and ability to be effortlessly modified in order to promote the immobilization of proteins, creating ideal interfaces with biological systems for tissue engineering. PEDOT:PSS possesses several advantages over other conductive polymers, such as high transparency in the visible spectral range, high flexibility, thermal stability and processability in aqueous dispersions<sup>106</sup>.

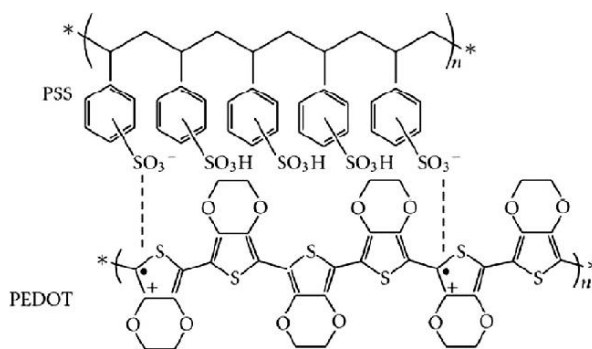


Figure 2 - PEDOT:PSS chemical structure.

#### 1.4.3.2. Piezoelectric hydrogels

Piezoelectric materials, owing to their capability of generating charges/potentials in response to mechanical deformations, have displayed great potential for fabricating smart stimulatory scaffolds for tissue engineering and are capable of delivering electrical cues without the need of an external stimulation device<sup>107</sup>. These materials also show electromechanical behavior (converse piezoelectric effect) and can be driven by physiological electrical changes to give rise to mechanical cues and have the ability to deform with physiological movements and consequently deliver electrical stimulation to cells or damaged tissue without the need of an external power source<sup>108</sup>. Also, piezoelectricity can be found in different parts of the human body, including bones, tendons, ligaments, cartilage, skin and cell membranes<sup>108</sup>. Piezoelectric materials used for tissue engineering include polymers such as poly(L-lactide) (PLLA), poly(vinylidene fluoride) (PVDF), poly(vinylidene fluoride-trifluoro ethylene) (PVDF-TrFE), and poly hydroxy butyrate (PHB); ceramics like hydroxyapatite (HA), barium titanate (BT), lithium niobate (LN) and boron nitride nano tubes (BNNT); and natural materials like diphenylalanine (FF), collagen, bone and silk, though these last ones have lower piezoelectric constants<sup>107</sup>.



Table 4 - Conductive hydrogels for cell experiments in current literature.

| Hydrogel base/Conductive Polymer | Conductive polymer concentration | Cells                                 | Bioengineering technique             | Ref |
|----------------------------------|----------------------------------|---------------------------------------|--------------------------------------|-----|
| GeIMA/PEDOT:PSS                  | 0.3%                             | Myoblasts (C2C12)                     | Extrusion Bioprinting                | 109 |
| GeIMA/PEGDA/PEDOT:PSS            | 0.35%, 0.49%, 0.70% and 0.91%    | DRG neuronal cell lines (50B11)       | Stereolithography                    | 110 |
| Collagen/Alginate/PEDOT:PSS      | 0.26% and 0.52%                  | Cardiomyocytes (P3)                   | Hydrogel scaffolds                   | 111 |
| p(HEMA-co-EGMA)/PEDOT:PSS        | 0 - 1%                           | Neuronal cells (PC12)                 | Microlithography                     | 112 |
| PEG/PEDOT:PSS                    | 0.7%                             | Adipose-derived stem cells            | Hydrogel scaffolds                   | 113 |
| GeIMA/ PANI                      | 0,16M                            | Murine mesenchymal cells (C3H/10T1/2) | Digital Projection stereolithography | 114 |
| Alginate/ PPy                    | 1.0 – 7.0M                       | Neuronal cells (PC12)                 | Extrusion Bioprinting                | 115 |
| Collagen/PPy-b-PCL               | 0.5%, 1% and 2%                  | Neuronal cells (PC12)                 | Extrusion Bioprinting                | 116 |
| GeIMA/ PEDOT NPs                 | 1.0 mM                           | Myoblasts (C2C12)                     | Extrusion Bioprinting                | 117 |
| Hyaluronic acid/alginate/ MXenes | 1.0 mM and 5.0 mM                | Human Embryonic Kidney 293 cells      | Extrusion Bioprinting                | 118 |
| chitosan-AuNPs                   | 36-108 mM                        | MSCs                                  | Hydrogel scaffolds                   | 119 |
| GeIMA-AuNPs                      | 0.5-1.5 mM                       | CMs                                   | Hydrogel scaffolds                   | 120 |
| CNTpega                          | 1-10 mM                          | Neuronal cells (PC12)                 | Hydrogel scaffolds                   | 121 |
| Chitosan-GO                      | 50-600 mM                        | heart H9C2 cells                      | Hydrogel scaffolds                   | 122 |

Piezoelectric polymers possess the advantage of processing flexibility and have high strength and high impact resistance as compared to inorganic materials. On the other hand, the common concern related with piezoceramics in tissue engineering is its cytotoxicity. In general, lead contained ceramics have limited application in tissue engineering due to their toxic nature<sup>123</sup>. Some examples of already developed piezoelectric hydrogels include scaffolds based on poly(lactic-co-glycolic) acid / barium titanate nanoparticle composites, with high proliferation and differentiation of muscle cells (H9C2 cell line)<sup>124</sup>, and collagen-based scaffolds for bone healing<sup>125</sup>.

#### 1.4.3.3. Magnetic field-responsive hydrogels

Magnetic field-responsive materials are comprised of magnetic micro- or nanoparticles, including ferromagnetic or paramagnetic particles, which are able to respond to magnetic fields<sup>126</sup>. Such magnetically responsive materials can potentially be used in bioinks for bioprinting, where orientation and alignment of particles in the printed construct can be tuned using a magnetic field<sup>127</sup>. Magnetic natural polymer hydrogels are composed of polymer matrix and magnetic inclusions, such as magnetic  $\text{Fe}_3\text{O}_4$  and  $\gamma\text{-Fe}_2\text{O}_3$ . The combination of such inorganic materials and natural polymer hydrogels will provide hydrogels magnetic sensitivity, which can overcome the inherent limitations of traditional hydrogels in targeted drug delivery and remotely controlled release. For instance, after introducing magnetic  $\text{Fe}_3\text{O}_4$  nanoparticles into a cellulose hydrogel, the drug release rate can be controlled by switching the magnetic field<sup>128</sup>. To date, various types of natural polymer-based magnetic hydrogels have been developed, such as polysaccharide-based hydrogels (cellulose, chitosan, starch, alginate, carrageenan, and hyaluronic acid), protein-based hydrogels (collagen and gelatin), and DNA-based hydrogels. Some examples of already developed magnetic-field responsive hydrogels include the development of a photocrosslinkable magnetic responsive hydrogel made of methacrylated chondroitin sulfate (MA-CS) enriched with platelet lysate (PL) with tunable features for tendon-to-bone interface. Osteogenically differentiated adipose-derived stem cells and/or tendon-derived cells were encapsulated within the hydrogel, proliferating and expressing bone- and tendon-related markers. External magnetic field (EMF) application modulated the swelling, degradation and release of PL-derived growth factors, and impacted both cell morphology and the expression and synthesis of tendon- and bone-like matrix with a more evident effect in co-cultures<sup>129</sup>. On another study, magnetic fibrin hydrogel scaffolds were prepared by the interaction of thrombin-conjugated iron oxide magnetic nanoparticles with fibrinogen and basal fibroblast growth factor (bFGF) stabilized with the conjugation of the growth factor to the magnetic nanoparticles ( $\gamma\text{-Fe}_2\text{O}_3$ ). Adult nasal olfactory mucosa (NOM) cells were seeded in the transparent fibrin scaffolds in the absence or presence of the free or conjugated bFGF-iron oxide nanoparticles. It was verified that the conjugated bFGF enhanced significantly the growth and differentiation of the NOM cells in the fibrin scaffolds, compared to the same or even five times higher concentration of the free bFGF<sup>130</sup>.

## **1.5. Bioprinting of cardiac tissues: applications and main limitations**

### **1.5.1. Cardiac repair and the emergence of cardiac tissue engineering**

Cardiovascular diseases (CVDs) are a group of disorders of the heart and blood vessels and are the leading cause of global deaths, responsible for an estimated 17.9 million deaths each year (about 31% of all deaths worldwide)<sup>131</sup>. Along with other nontransmissible or chronic diseases like Alzheimer, cancer, and diabetes, it is expected for it to become the leading cause of loss of health and life worldwide, including in developing countries<sup>132,133</sup>. The heart is a structurally and functionally complex organ, that demands high cell density and metabolic effort due to its large consumption of oxygen. The heart wall is composed of tightly packed myocytes and fibroblasts, with dense supporting vasculature and collagen-based extracellular matrix. The myocytes, which confer contractibility to the heart, form a three-dimensional functional syncytium that enables propagation of electrical signals to produce mechanical contractions that pump the blood<sup>134</sup>. However, after myocardial damage, the heart is an organ that has minimal intrinsic regenerative capabilities<sup>133</sup>, therefore, early prevention through pharmacological strategies, and transplantation at the end-stages, which is expensive and limited by organ shortage and rejection, are currently the only viable solutions in treating heart failure with good long-term results. As an alternative, the emerging field of regenerative medicine-based therapies and tissue engineering have shed new hopes to repair or replace tissues and organs damaged by age, disease, trauma and to correct congenital defects.

### **1.5.2. Characteristics of cardiac tissues**

Cardiac muscle tissue, or myocardium, is a syncytial, electrically coupled 3D network of differentiated and electrically interconnected cardiomyocytes combined with fibroblasts, endothelial cells, smooth muscle cells, and various other non-cardiac muscle cells<sup>135</sup>. The intercellular connective structures include adherent junctions, desmosomes, and gap junctions. Adherent junctions connect the actin cytoskeleton of adjacent cells, desmosomes are cell adhesion junctions that anchor the cell membrane to the intermediate filament network and gap junctions metabolically and electrically connect the cytoplasm of adjacent cardiomyocytes<sup>136</sup>. It is a striated muscle comprised of a compact network of muscle strands that occur due to alternating filaments of myosin and actin protein, called myofilaments, and consist of sarcomeres<sup>137</sup>. The sarcomeres, that are densely packed and highly organized contractile units of about 1.8-2.0  $\mu\text{m}$  long, consist of proteins that form thick and thin filaments with different landmarks corresponding to different functional units: Z-discs mark sarcomere borders; I-, H-, and A-bands mark different areas of thick, thin, and overlapping filaments; and M-bands form the central line<sup>138</sup>.

Another component of cardiac muscle cells is the cardiac transverse tubules (t-tubules), that are highly branched invaginations of cardiomyocyte sarcolemma (muscle cell membrane) that penetrate the intracellular space of cardiomyocytes, rich in ion channels important for excitation-contraction coupling, maintenance of resting membrane potential, action potential initiation and

regulation, and signaling transduction, and serve as a centralized signaling hub controlling cardiac contractile function and electrophysiology<sup>139</sup>.

Also, cells on cardiac muscle tissue are embedded in a network of ECM components, that are crucial for correct development and function of the heart and provides a strong support for elastic anchorage for precisely aligned cardiomyocytes and a specialized environment that allows electrical coupling and cardiac impulse propagation between adjacent cells and transmission of contractile forces of cardiomyocytes to the surrounding matrix for the repetitive blood pumping function of the heart<sup>53</sup>.

Finally, calcium handling is related to the role that calcium ions play in linking the electrical activation and mechanical contraction of the cardiac muscle tissue. Calcium ions can either enter the cardiomyocytes through ion channels during each beat or be supplied from the sarcoplasmic reticulum, a big chamber inside the cell that stores most of the calcium required for heart contraction. The calcium ions bind to the troponin complex in the cells, making them contract, and during relaxation, calcium is detached from troponin and is expelled out the cell or stored back in the sarcoplasmic reticulum, in a process called excitation-contraction coupling. Also, due to having an electrical charge, calcium ions contribute to the propagation of the electrical signal that moves cell to cell to produce a uniform contraction<sup>140</sup>.

### **1.5.3. In vitro engineering of cardiomyocytes**

#### **1.5.3.1. Main traits and characteristics of in vitro engineered cardiomyocytes**

Cardiomyocytes (CMs) are the contractile cells of the heart. When stressed, cardiomyocytes undergo enlargement (hypertrophic growth) and apoptotic responses due to increased contractile force, and can lead to heart failure, both in vivo and in vitro cell culture models<sup>141</sup>. They are terminally differentiated cells that are extremely difficult to expand in vitro and are not able to compensate cell loss that occurs during myocardial infarction or chronic heart failure<sup>135</sup>. These cells have a rate of renewal in the order of 0.5%-1% per year, and so an infarct large enough to cause significant heart failure will cause the death of hundreds of millions of cardiomyocytes<sup>142</sup>. The majority of therapies used in clinical trials for cardiac tissue damage repair include cell replacement through application of bone marrow mesenchymal stem cells (MSCs), peripheral blood mononuclear cells or resident cardiac cells. However, their inability to proliferate and produce sufficient amounts of CMs limits the improvement or regeneration of damaged tissue. As an alternative, the combination of these cells with biomaterials such as bioprinting has emerged<sup>133</sup>.

Cardiomyocytes can be successfully differentiated from stem cells in vitro with high yield and purity<sup>143</sup>, and are increasingly used to model cardiac disease, test drug efficacy and for safety pharmacology<sup>144</sup>. The use of hiPSC-CMs enables an unlimited supply of patient-specific stem cells, that can be used for disease modelling, molecular diagnosis, cell-based therapy and testing of personalized treatments<sup>145</sup>. However, these cells are often immature and with similarities to fetal rather than adult cardiomyocytes, which limits their application in cell based cardiac repair, cardiac drug toxicology screening, and human cardiac disease modeling.

### 1.5.3.2. Mature vs Immature cardiac cells

hiPSC-CMs present characteristics aligned with neonatal cardiomyocytes rather than adult cardiomyocytes. On Table 5<sup>53</sup> there is a summary of the defining characteristics between mature and immature cardiomyocytes.

Table 5 - Differences between mature and immature cardiomyocytes.

| Characteristics     | Mature (adult-like)                         | Immature (fetal-like)                           |
|---------------------|---|---|
| <b>Structure</b>    | Rod-shaped                                  | Small and circular cells                        |
|                     | Usually bi-nucleated                        | Mono-nucleated                                  |
|                     | Organized sarcomeres of 2.2 $\mu\text{m}$   | Organized sarcomeres of 1.6 $\mu\text{m}$       |
|                     | Gap junctions' location: intercalated disks | Gap junctions' location: circumference of cells |
|                     | T-tubules present                           | T-tubules absent                                |
| <b>Mitochondria</b> | Synchronous contraction                     | Erratic contraction                             |
|                     | Ovular shape, 35% volume                    | Slender and log, smaller than adult             |
|                     | In the direction of the sarcomere           | Close to the nucleus and the periphery          |
| <b>Force</b>        | 40-80 mN/mm <sup>2</sup> in 3D              | 0.08-4 mN/mm <sup>2</sup> in 3D                 |
| <b>Conduction</b>   | Conduction velocity: 0.3 -1 m/s             | Conduction velocity: 0.1-0.2 m/s                |
|                     | Upstroke velocity: 150 - 350 V/s            | Upstroke velocity: 10-50 V/s                    |
| <b>Metabolism</b>   | Mainly fatty acids                          | Glucose and lactase                             |
| <b>Expression</b>   | MYH7 (b-MHC) > MYH6 (a-MHC)                 | MYH6 (a-MHC) > MYH7 (b-MHC)                     |
|                     | MYL2 (MLC2v) > MLY7 (MLC2a)                 | MYL2 (MLC2v) : MLY7 (MLC2a)                     |
|                     | TNNI 3 (cTnl) > TNNI1 (fetal ssTnl)         | TNNI1 (fetal ssTnl) > TNNI 3 (cTnl)             |

### 1.5.4. Strategies to improve maturity of hiPSC-CMs in vitro

Several strategies in stem cell biology, material science and biofabrication methodologies have greatly contributed for the creation of promising tissue engineered cardiac models and have been proposed to improve the maturation state of hiPSC-CMs, with various degrees of success. These strategies are related to topology, stiffness, electric and magnetic stimulus, chemical and biochemical changes in media formulation and are explored in the section bellow.

#### 1.5.4.1. Long term culture

The complete development and maturation of adult cardiomyocytes normally requires 6 to 10 years in vivo<sup>146</sup>. hiPSC-CMs however, can reach mature-like features in over 100 days when cultured extendedly in vitro<sup>147</sup>. These cultures show molecular signatures similar to adult CMs, and though long-term culture is relatively easy and does not require expensive experimental equipment, such a solution is not feasible for routine biomedical assays due to being very time-consuming, labor intensive and cost prohibitive<sup>147</sup>.

#### 1.5.4.2. Electrical Stimulation

hiPSC-CMs exhibit spontaneous contractility, but, this electrical activity is usually irregular, and the frequency gradually decreases over time in culture<sup>148</sup>. It has been shown, in rodent cells, that electrical stimulation can improve cell-to-cell coupling and alignment, and the remodeling of these cells to an immature phenotype in culture was prevented by electrical stimulation<sup>149</sup>.

Other studies have shown beneficial effects of electrical stimulation on hiPSC-CM maturation evidenced by increased rectifying K<sup>+</sup> current (IK1) and, consequently, lower resting membrane potential, improved Ca<sup>2+</sup> handling (increase in amplitude, upstroke, and decay rate of the Ca<sup>2+</sup> transient), increased contractile forces, and a higher degree of sarcomeric organization<sup>150</sup>.

#### 1.5.4.3. Mechanical Stimulation

The heart is essentially a mechanical pump that continuously responds to mechanical stimuli at all developmental stages, the result of hemodynamic load (cyclic stretch), physical interaction with extracellular matrix (static stretch), and laminar blood flow (shear stress)<sup>151</sup>. Therefore, mechanical stress can be a critical factor in shaping cardiomyocyte maturation. Some common strategies used include cyclic stretch, pulsatile flow, and 3D tissue engineering or electrical stimulation combined with mechanical stimulation. Cyclic stretch has been the most common approach in many studies, and they demonstrate increased rate of maturation in hiPSC-CMs, with an increased expression in ion channel genes such as KCNJ2, increased expression of IK1 and negative resting membrane potentials. Cyclic stretch at rates of 1-2 Hz was shown to promote maturation both morphologically and functionally in hiPSC-CMs<sup>152</sup>.

In more recent studies, it has been shown that the combination of mechanical stimulus coupled with either tissue engineering or electrical stimulation leads to greater maturation success. Studies have shown that mechanical stimulation applied to hiPSC-CMs on a collagen hydrogel<sup>153</sup> and cyclic stretch applied to hESC-CMs on gelatin-based scaffolds resulted in an enhancement in cardiomyocyte maturation. Other study showed that two weeks of static stress stimulation combined with electrical pacing revealed higher contractility, changes in morphology, cell alignment and improved calcium handling of hiPSC-CMs<sup>154</sup>. More recently, remarkable ultrastructural and functional maturation was observed when applying passive stretch<sup>155</sup> and early-stage gradual increase in electrical stimuli frequency<sup>156</sup>, demonstrating the relevance of dynamic conditioning to enhance maturation.

#### 1.5.4.4. Substrate topology and stiffness

Myocardium stiffening processes occurs during the developmental process, beginning from the embryonic stage to the adult stage. There is a 3-fold increase of elastic modulus of stiffness in mice strongly that has been shown that affects the heart's ability to pump blood and increase blood pressure<sup>157</sup>. Therefore, modulating substrate stiffness provides an alternative route to adjust the mechanical load experienced by cardiomyocytes. Culturing these cells on a functionalized micropatterned substrate improved sarcomere organization, myofibril alignment and contractility, if the substrate displayed a physiological stiffness (Young's modulus around 10 kPa)<sup>158</sup>.

#### 1.5.4.5. 3D strategies

The heart and its components are 3D structures composed of cardiomyocytes, ECM and blood vessels that interact with each other to make the function organ. Therefore, strategies for 3D cell culture and maturation have been studied so that the cells have grown on an environment as similar as possible to in vivo. Some strategies are reviewed on the segment bellow.

#### 1.5.4.5.1. Co-culture

Tough the principal cardiac cells are cardiomyocytes, the heart is composed of other cells such as fibroblasts, endothelial cells and smooth muscle cells *in vivo* and it is believed that all these cells can exert an impact on cardiomyocyte maturation through direct physical contact or paracrine effects<sup>158</sup>. A cardiac microenvironment mimicking physiological conditions *in vivo* is crucial for inducing cardiomyocytes differentiation as well as maturation. It has been shown that co-culture with endothelial cells<sup>159</sup>, as well as a combination of cardiac ECM, endothelial cells and smooth muscle cells improve cardiomyocyte maturation<sup>160</sup>.

#### 1.5.4.5.2.3D Cell Culture

Shifting from to 2D-based to 3D culture systems, such as spheroids<sup>161</sup> and engineered tissue constructs<sup>4</sup>, has greatly improved hiPSC-CM metabolic and electrophysiological maturity. 3D strategies have provided the best outcomes to boost hiPSC-CMs maturation and revealed suitable to assess CM performance upon stimulation aimed to improve their maturity. Nonetheless, even the most advanced strategies reported to date are still unable to emulate certain features (contractile force and action potential upstroke velocity) of mature cardiac tissue. Developing advanced 3D tissue constructs able to accurately model the native microenvironment will be key to achieve the unmet goal of maturing hiPSC-CMs and unlock their full potential in pre-clinical research.

#### 1.5.4.5.3. Hydrogels

Hydrogels for cardiac tissue engineering have been extensively used due to their ability to promote cell adhesion and growth, mimicking the microenvironment of cardiac tissues to provide mechanical support for cardiomyocytes maturation. This topic has been explored further in section 1.4.

Cardiomyocytes are highly sensitive to environmental factors, such as elasticity, geometry and topography and extracellular substrates induce some aspects of cardiac maturity. Therefore, in order to emulate the native cardiac environment, an ideal bioink material, besides being commercially feasible, rapidly produced, and have the desired printability, must have long-term elasticity and mechanical strength to sustain the high repetitive mechanical stress and non-linear elasticity of contracting muscle, high biocompatibility, controllable electrical properties that do not interfere with the electrical conductance of the action potential and be biodegradable to facilitate cell attachment.

### 1.5.5. Bioprinting for cardiac tissue engineering

Conventional fabrication approaches for cardiac tissue engineering lack control over scalability and homogeneous cells distribution. Bioprinting provides a technological platform for controlled deposition of biomaterials, cells and biological factors in an organized fashion. Bioprinting is capable of alternating heterogeneous cell printing, printing anatomical relevant structures and microchannels resembling vasculature network, all essential features for an engineered cardiac tissue. These engineered scaffolds can then be implanted *in vivo*, providing a structure to

condition stem cells already present or to transplantable cells that can be contained and organized in these scaffolds<sup>162</sup>. However, despite its significant progress and promise, some challenges need to be overcome. One of the challenges is printing resolution. To closely mimic native tissue, bioink should be ideally deposited with a resolution comparable to cell size (5-10  $\mu\text{m}$ )<sup>163</sup>. Additionally, to reach clinical applications, thick multi-layered muscle tissue is required. The maximum nutrient/oxygen diffusion distance for cells to survive without vascularization is  $\sim 100\text{-}200\ \mu\text{m}$ <sup>164</sup>. However, it is still challenging to generate controlled vascular tree-like networks. The realization of vascularized cardiac tissue engineering might be a barrier for another decade. In recent decades, bioprinting techniques for cardiac tissue engineering have significantly developed in structural complexity, but bioprinting of soft materials (hydrogels) is still immature and many challenges remain<sup>165</sup>. Luckily, the emerging concept of using a reversible support bath to enable freeform reversible embedding of suspended hydrogels bioprinting is valid for most low-viscosity materials and makes it possible to print any complicated structure without the design of extra support<sup>166</sup>.

### **1.6. Motivation, Aim, Objectives and Research Strategy**

Bioprinting of cellular structures and tissues is quite relevant for tissue engineering as a way to recapitulate a biologic tissue and compared to conventional methods, 3D bioprinting allows for greater precision in the construct of the desired tissue. ECM-based biomaterials have come up as great scaffold alternatives for tissue engineering, due to its important source of biochemical and biomechanical signals that support cell differentiation and function, as well as approximation to physiological conditions. Due to the need for 'smart' materials in tissue engineering, functional features were introduced to dECM hydrogels by the addition of dopants, including conductive polymers, magnetic nanoparticles and piezoelectric particles. One potential application of these, could be cardiac tissue engineering. As previously mentioned, the immaturity of hiPSC-CMs severely limit their use in cardiac tissue engineering. Strategies that attempt to mimic in vivo conditions more accurately are urgently required. Conductive hydrogels have the potential to improve the maturity of cardiac cells engineered in vitro, by promoting electrical stimulation of the scaffolds, resulting in potential vascularization and stem cell differentiation to form properly functioning cardiac tissues.

The aim of this work was to develop and bioprint ECM-based bioinks to produce electroconductive scaffolds for tissue engineering, with particular interest in cardiomyocyte maturation.

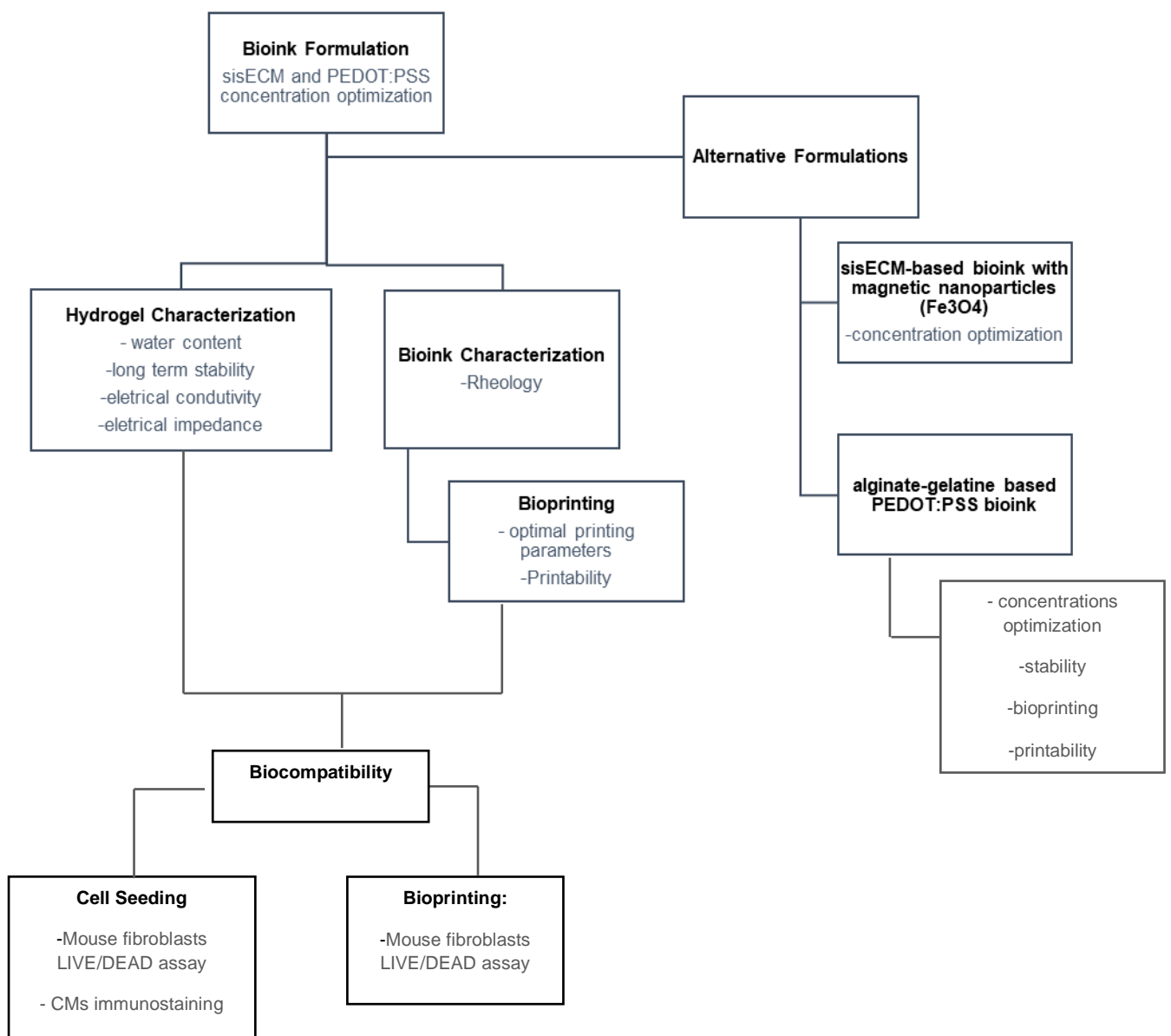
Towards this goal, the following objectives have been established:

- 1) Development of a bioink formulation containing PEDOT:PSS: The formulation of a conductive bioink was evaluated, optimizing the concentrations of the different components.
- 2) Characterization of dECM conductive hydrogels: hydrogels were characterized to evaluate their rheological, electroconductive and stability properties.



- 3) Optimization of the bio-/printing conditions: printing parameters were tuned for optimal bioprinting of mechanically stable constructs; printability was also evaluated.
- 4) Alternative formulations, containing magnetic nanoparticles and an alginate-gelatin-based conductive bioink were evaluated for potential development of a magnetic-field responsive bioink and as alternatives to dECM-based conductive bioink, respectively.
- 5) Biocompatibility: evaluation of dECM conductive bioink toxicity on mouse fibroblasts and hiPSCs-CMs, for both hydrogel scaffolds and bioprinted constructs.

Bellow, a workflow of this project is depicted, evidencing the materials and techniques used for the formulation and printing of the bioinks as well as all the characterization techniques and the biological studies performed on the biomaterials developed.



## Chapter 2 – Materials and Methods

### 2.1. Bioink Formulation

The main component of the proposed bioinks is decellularized extracellular matrix, obtained from porcine small intestine submucosa (sisECM). This material was kindly provided by collaborators at the University of Nottingham. After decellularization, the sisECM was stored at -20°C until further use.

#### 2.1.1. sisECM digestion

For the formulation of the bioinks, an already existing protocol for the digestion of sisECM gels was followed. Briefly, for the preparation of 10 mg/mL sisECM stock solution, 1g of sisECM was digested in a solution containing 1 mg/mL of pepsin from porcine gastric mucosa ( $\geq 2.500$  units/mg protein, Sigma-Aldrich) in 100 mL of 0.01 N HCl and stirred for 48-72 hours at room temperature. Once the sisECM was fully digested, aliquots were prepared and stored in the freezer at -20°C or kept at 4°C for immediate use. Images of the sisECM before and after digestion can be seen in Figure 8.



Figure 8 - sisECM digestion, with constant stirring at room temperature

#### 2.1.2. sisECM hydrogel and bioinks preparation

An already existing protocol was followed<sup>167</sup>. 8 mg/mL was selected as the working sisECM concentration. For the gelation of the sisECM, stock solution of digested sisECM was mixed with a neutralization buffer (NB). NB was prepared by mixing 0.1 N NaOH (1/10 of the volume of stock solution), 10x Phosphate Buffer Solution (PBS) (pH=7.4; Sigma-Aldrich; 1/9 of the volume of stock solution) and 1x PBS (pH=7.4; Sigma-Aldrich; making up the final volume). It was then placed at 37°C for gelation to occur. When mixing the different components, the formation of air bubbles in the solution must be avoided, as they can affect the mechanical properties of the

gels. A schematic diagram showing the sisECM hydrogel and bioink formulation, as well as the hydrogels before and after gelation, can be seen in Figure 9.

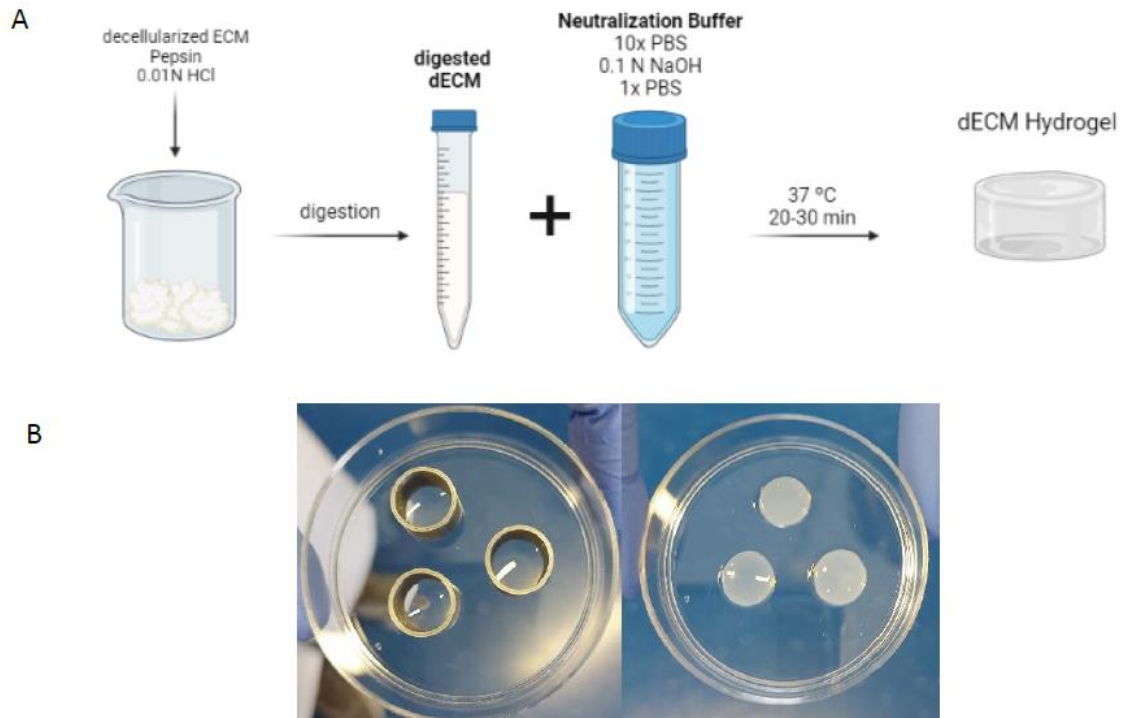


Figure 3 – A: Schematic for sisECM digestion and hydrogels/bioinks preparation; B: Final dECM hydrogel before incubation (left) and after 30 minutes incubation at 37°C (right)

### 2.1.3. Preparation of gelatin support bath for FRESH extrusion bioprinting

For the preparation of the gelatin support bath, an already existing protocol was followed<sup>41</sup>. DI water was preheated at 40-45°C. Porcine skin gelatin (Type A, Sigma-Aldrich), 4% w/v, and CaCl<sub>2</sub> (Honeywell), 0.16% w/v, were added to the warmed water, maintaining agitation until all gelatin was dissolved and solution was clear. The solution was then kept overnight at 4°C to ensure complete gelation on the blender (SilverCrest) for ease of operation. When ready for use, the jar was filled with approximately the same volume of a 0.16% CaCl<sub>2</sub> solution as gelatin and all was blended with pulses for 60-90s. The desired amount was then pipetted to falcon tubes and centrifuged for 2 min, at 4500 rpm. The supernatant, as well as any foam that formed was removed. On Figure 10, a schematic of this process is represented.



Figure 10 - Gelatin preparation schematic

#### 2.1.4. Alginate-gelatin bioink preparation

For the preparation of this bioink, an already existing protocol was adapted<sup>168</sup>, and a schematic for this procedure is represented in Figure 11. Alginate sodium salt (MPbio) was dissolved in PBS to obtain a final solution of 5% w/v. Porcine skin gelatin (Sigma-Aldrich), was dissolved in water, for a final solution of 15% w/v, and pre-treated at 80°C for 3 hours with continuous stirring and stored at 4°C. For the final bioink formulation, 1:1 ratios of the previous solutions were mixed for 10 minutes at 37°C before printing. The final bioink concentration was 2.5%/7.5% Alginate-gelatin (alg-gel).

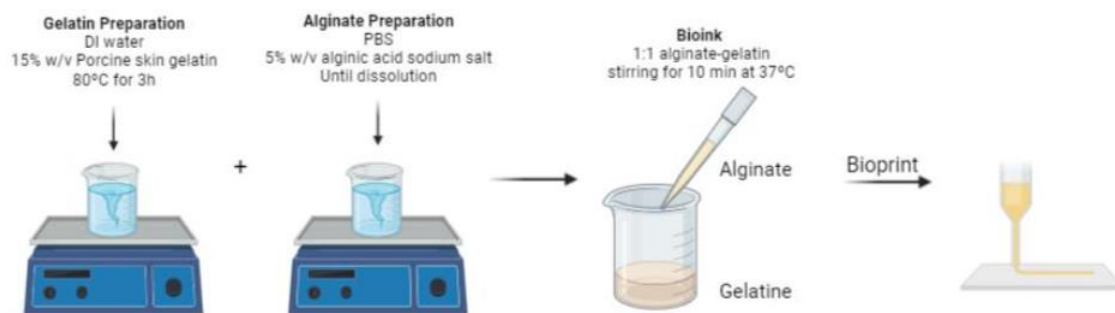


Figure 4 - Alginate-Gelatin bioink preparation schematic.

#### 2.1.5. Magnetic field-responsive bioink preparation

**Magnetic nanoparticles:** The magnetic nanoparticles (MNPs) were synthesized by chemical coprecipitation of two different iron salts  $\text{FeCl}_3$  and  $\text{FeCl}_2$  in alkaline media. Briefly, an aqueous solution with 25% of ammonium hydroxide ( $\text{NH}_4\text{OH}$ ) was added to a mixture of  $\text{FeCl}_3$  and  $\text{FeCl}_2$  at 80 °C, under permanent stirring at 1250 rpm by purging  $\text{N}_2$ . Potassium oleate and ammonium persulfate were then added to the reaction mixture for production of  $\text{Fe}_3\text{O}_4$ -coated particles aiming to minimize particle aggregation. Hitenol-BC was used as a surfactant. Particles then precipitated and after solvent decantation, were left to dry for 1-2 weeks<sup>169</sup>.

**Magnetic Responsive Hydrogel:** MNPs were dispersed by sonication at a concentration of 0.2% in neutralization buffer and added to the sisECM solution. The resulting hydrogel was incubated for 1 h at 37°C.

#### 2.1.6. PEDOT:PSS concentration adjustments

To the 8 mg/mL dECM hydrogel, PEDOT:PSS (Clevios PH1000, stock solution 1%) was added, by mixing thoroughly with a pipette. A description of the different concentrations of PEDOT:PSS tested can be seen in Table 6.

Table 6 - All PEDOT:PSS concentrations tested and respective gelation outcome

| PEDOT:PS<br>Concentration (%) | sisECM<br>Concentration<br>(mg/ml) | ml Neutralization<br>Buffer | ml sisECM | ml PEDOT:PSS |
|-------------------------------|------------------------------------|-----------------------------|-----------|--------------|
| 0.01                          | 7.9                                | 0.2                         | 0.8       | 10           |
| 0.05                          | 7.6                                | 0.2                         | 0.8       | 53           |
| 0.1                           | 7.3                                | 0.2                         | 0.8       | 110          |
| 0.2                           | 6.4                                | 0.2                         | 0.8       | 250          |
| 0.25                          | 6.01                               | 0.2                         | 0.8       | 330          |
| 0.1                           | 6.00                               | 0.33                        | 0.67      | 110          |
| 0.2                           | 7.3                                | 0.2                         | 0.8       | 110          |

## 2.2. Hydrogel Characterization

### 2.2.1. Water content assay

Hydrogels were prepared following the protocol described in section 1.2 and casted on cylindrical molds with 1 cm height and 1 cm diameter, containing 500  $\mu$ L of the sisECM, sisECM + 0.05% PEDOT:PSS and sisECM + 0.1% PEDOT:PSS solutions. At least three samples of each material were prepared. After incubation for 30 minutes at 37°C, molds were removed, and wet weights of each hydrogel were recorded. Samples were then dried at 60°C. After complete water removal, the samples were weighed. The water content was calculated following Equation 1, where  $W_{dry}$  is the weight after water removal and  $W_{wet}$  is weight of the hydrated structures.

$$\frac{W_{wet} - W_{dry}}{W_{wet}} * 100\% \quad (1)$$

### 2.2.2 Stability Assay

Hydrogels were prepared following the protocol described in section 2.1.2 and casted on cylindrical molds with 1 cm height and 1 cm diameter, containing 500  $\mu$ L of the sisECM, sisECM + 0.05% PEDOT:PSS and sisECM + 0.1% PEDOT:PSS solutions, one replicate per bioink. After incubation they were stored with PBS at room temperature. Images of the hydrogels were recorded at 0, 1, 3, 5, 7, 10, 15, 20 and 30 days.

## 2.3. Electrical characterization

### 2.3.1 Resistance

Hydrogels were prepared following the protocol described in section 2.1.2 and casted on cylindrical molds with 1 cm height and 1 cm diameter, containing 500  $\mu$ L of the sisECM, sisECM + 0.01% PEDOT:PSS, sisECM + 0.05% PEDOT:PSS and sisECM + 0.1% PEDOT:PSS solutions, with three replicates per bioink. Resistance ( $\rho$ ) was recorded using a Velleman DVM832 digital multimeter, with fixed distance of 0.5 cm between tips. The electrical conductivity ( $\sigma$ ) is the inverse of the resistance and was calculated using equation 2.

$$\sigma = \frac{1}{\rho} \quad (2)$$

### 2.3.2 Four-probe method

sisECM, sisECM + 0.05% PEDOT:PSS and sisECM + 0.1% PEDOT:PSS bioinks were prepared and 150  $\mu\text{L}$  volume per sample was deposited on glass sheets and left to completely dry for 10 days, with three replicates per bioink. In this step it is important to guarantee that samples are consistently laid on the glass sheets to avoid significant thickness variations through the sample. Resistance was measured on dried samples using a 4-point probes method. After samples were dried, four strips of gold electrodes were deposited on top of the materials by physical vapour deposition using an Edwards Vacuum Coating System E306A, across the entire film and with equal distance from each other. Electrodes were put in direct contact with the gold stripes and measurements were taken. Resistance was calculated using Equation 3, where  $t$  is the sample thickness (measured using a Bruker's Dektak 3.21 Profilometer (Bruker, Billerica, MA, USA),  $l$  is the length of the sample (varied between 0.47-1.4 cm), and the  $gap$  is the distance between gold bands (fixed distances between 330-2000 mm) . The electrical conductivity was then calculated using Equation 2. A diagram of the 4-probes method, and pictures of the experimental set up are in Figure 12.

$$\rho = \frac{R * t * l}{gap} \quad (3)$$



Figure 12 - 4-probes schematic (left), with the representation of the 4 probes (current passes on the outer probes and voltage is read across the inner probes) and gold deposited strips, with  $d$  corresponding to the gap between gold strips; and gold deposition chamber (right)

### 2.3.3. Electrochemical Impedance Spectroscopy (EIS)

Hydrogels were prepared following the protocol described in section 2.1.2 and casted on cylindrical molds with 1 cm height and 1 cm diameter, containing 400  $\mu\text{L}$  of the sisECM, sisECM + 0.05% PEDOT:PSS and sisECM + 0.1% PEDOT:PSS solutions and stored in DI water until measurement. Five replicates per bioink were prepared. EIS measurements were performed at room temperature on a homemade electrochemical setup, Figure 13. The wet samples were sandwiched between two copper electrodes for the measurements, that were used in a two-electrode configuration (schematic of this set up in Figure 6). EIS analysis was performed using a PalmSen4 potentiostat. Data analysis was done using PSTrace software from PalmSens. The



frequencies applied ranged between 0.1Hz and 10 MHz and the number of frequencies applied was 71.

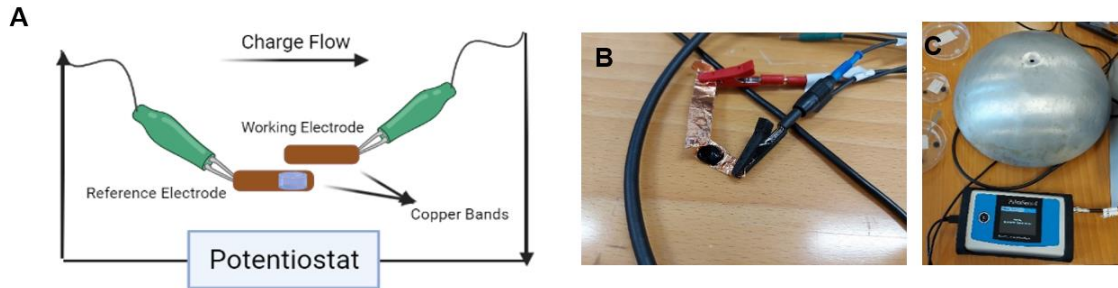


Figure 5 – A: Schematic for the two electrode set up for EIS measurements; B: Copper bands for sample deposition, with sisECM + 0.1%PEDOT:PSS sample; C: EIS setup with PalmSens4 potentiostat and Faraday cage.

## 2.4. FRESH extrusion printing

### 2.4.1. Bioprinter setup

The bioprinter used was a F4200N.2 Compact Benchtop Robot, Fisnar, Figure 14. Additional hardware includes a teach pendant to control the printer and a pneumatic dispensing unit (Fisnar DC100 high precision dispenser) connected to a compressed air hose. The bioprinter was maintained in a laminar hood flow to preserve sterility during the printing process.



Figure 14 - Bioprinter setup; A: Fisnar Compact Desktop Robot; B: Teach Pendant; C: Air dispensing Unit

Additional materials used for bioprinting include cartridges (QuantX™ syringe barrels, 5cc), pistons (Evenpress™ low viscosity pistons, 5 cc), needles (Blunt End Dispensing Tips, 0.3-0.6 mm), barrel adapter (QuantX™ Syringe Barrel Adapters with Hose) and end caps (QuantX™ Syringe Barrel End Caps), Figure 15.

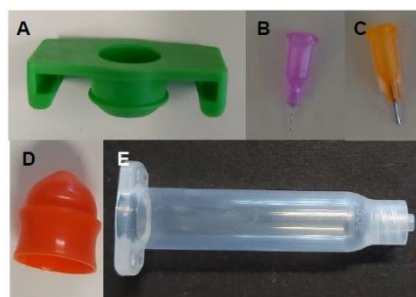


Figure 15 - Materials for bioprinting; A: 5 cc end cap; B: 0.3 mm diameter needle; C: 0.6 mm diameter needle; D: 5 cc piston; and E: 5 cc ink cartridge.

## 2.4.2. Scaffold Design

The scaffolds were designed using Fisnar robot edit v2.6 software. The overall design of the scaffold consists of a 2D geometry, deposited layer-by-layer, moving in the z axis, to reach a 3D scaffold. The geometries tested were squares and circles of different dimensions, Table 7, as well as more complex geometries that are represented on Figure 16.

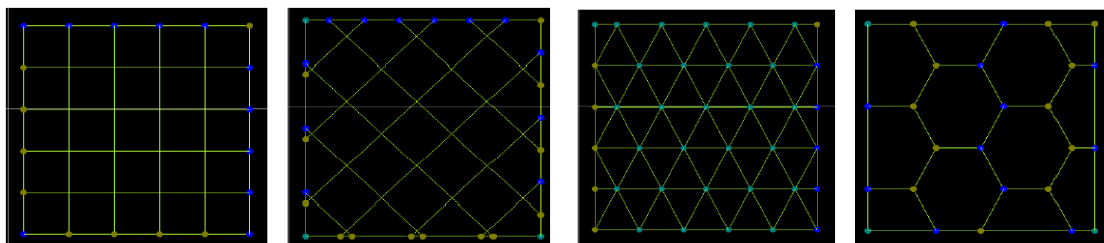


Figure 16 - Fisnar Robot Edit software interface, with a square mesh geometry, diagonal mesh geometry, triangle mesh geometry and honeycomb mesh geometry, from left to right, respectively.

Table 7 - Overall dimensions for the different geometries used for bioprinting

| Geometries | Ranges               |
|------------|----------------------|
| Square     | L = 5 mm; L = 10 mm  |
| Circle     | R = 2.5 mm; R = 5 mm |
| Mesh       | L = 10 mm; L = 20 mm |

## 2.4.3. Optimization of printing parameters

For the optimisation of the printing, different parameters were tested. On Table 8 a summary of the parameters used can be found.

Table 8 - Printed structures attributes and the intervals they were varied to achieve optimal conditions

| Attributes              | Ranges         |
|-------------------------|----------------|
| Printing Speed          | 2 – 45 mm /s   |
| Dispensing Pressure     | 0.1 – 5 psi    |
| Number of Layers        | 1 - 10         |
| Distance between layers | 0.02 – 0.05 mm |
| Needle Diameter         | 0.3-0.6 mm     |

## 2.5. Bioink Characterisation

### 2.5.1. Rheology – oscillating time sweep

A rheometer (model MCR92, Anton Paar) equipped with a 1 ° cone plate with a diameter of 50 mm was used to characterize the rheological properties of the bioinks. 500 µL of prepolymer solutions were prepared, with three replicates per bioink, and were then pipetted onto the rheometer. Initial plate temperature was kept at 4 °C. Viscosity was then determined through an oscillating time sweep under an amplitude of 1% and frequency of 1 Hz, for 20 minutes at 37 °C.



### 2.5.2. Printability

Printability was evaluated after the printing of a square mesh, Figure 16, left image, with L= 20 cm. Photographs of the strands for each condition were taken using a Fischer magnifying lens, with 0.63x magnification, and measures were manually taken using the ImageJ software.

## 2.6. Cell Culture

### 2.6.1. hiPSCs culture and passaging

A REBL-PAT hiPSC cell line derived from a skin punch biopsy from a male subject was used. hiPSCs were cultured on Matrigel-coated plates and incubated at 37°C in a 5% CO<sub>2</sub> atmosphere. The passaging number of the cells were 38-39. For the coating, culture plates were coated with Matrigel (Corning) 1:100 in DMEM (Dulbecco's Modified Eagle Media; ThermoFischer) for 45 minutes at room temperature or overnight at 4°C. Cells were cultured on E8 culture media (Essential 8 (Lifetech Cat no. A1517001); ThermoFischer) and media was changed on a daily basis.

For hiPSCs passaging, culture media was aspirated, and cells were washed in PBS. After this, cells were incubated in TrypLE (TrypLE Select (Life Tech #12563-029); ThermoFischer) for 3 min at 37°C. TrypLE was aspirated and cells were carefully detached from the bottom of the plate using the E8 solution. The desired concentration of cells was then transferred to a fresh Matrigel-coated plate containing 1:1000 of Rock inhibitor (Y27632, Tocris). For cell maintenance, media was changed every 2 days.

### 2.6.2. hiPSCs differentiation towards cardiomyocytes

Differentiation of hiPSCs into cardiomyocytes was induced when cell confluence reached 90%, as previously reported<sup>170,171</sup>. Cells were preconditioned using E8 media supplemented with 1:1000 ROCK inhibitor. Media was changed in the subsequent two days with E8 and approximately, 60 hours after the preconditioning process started, media was changed to StemPro 34 SFM (1X) media (2% StemPro™-34 Nutrient Supplement + 1% L-Glutamine (Lifetech Cat no. 10639011)), supplemented with 1:10000 BMP4 (R&D Systems Cat no. 314-BP-010) and 1:100 Matrigel.

On day 0 of differentiation, media was changed Stem Pro 34, supplemented with 1:1000 BMP4 and 1.6:1000 activin A (Lifetech Cat no. PHC9561). On day 2, media was changed to RPMI/B27 minus insulin (RPMI base media with B27 (Ins-) Lifetech Cat No. A1895601), supplemented with 1:1000 KY02111 and 1:1000 XAV939. On day 4, media is changed to RPMI/B27 (with insulin), supplemented with 1:1000 KY02111 (R&D Systems Cat Nos. 4731) and 1:1000 XAV939 (R&D Systems Cat Nos. 3748). From days 6 to 13, media is changed every 2 days to RPMI/B27 media (RPMI base media with B27 Lifetech Cat No. 17504044). After, media is changed twice a week with RPMI/B27 for cell maintenance. All the different types of media used contained 1% Penicillin-Streptomycin (5,000 U/mL; Cat No. 15070063; ThermoFischer).

Cardiomyocytes were dissociated 10 weeks after differentiation following an existing protocol<sup>170,171</sup>. A dissociation solution was prepared with 1:2 Collagenase II (200 U/ml) solution

in Ca<sup>2+</sup> free HBSS (Hanks' Balanced Salt Solution; ThermoFischer), 1:1000 HEPES ((4-(2-hydroxyethyl)-1-piperazineethanesulfonic acid )), 1:1000 ROCK inhibitor and 1:1000 30 mM BTS (N-Benzyl-p-toluenesulphonamide). Cells were washed twice with warm HBSS solution and dissociation solution was then added and incubated for 3 hours at 37°C. After incubation, cell suspension was removed from the plates and transferred to a 50 mL falcon tube, followed by the addition of a blocking buffer (prepared with plain RPMI media and 1:500 Dnase). Falcon tube contents were centrifuged for 15 minutes at 100 G, and then cells were resuspended in suspending media, prepared with RPMI/B27 media, 1:10 FBS (Fetal Bovine Serum) and 1:100 ROCKi.

Cells are then prepared to be counted and plated. Harvested cells are resuspended in 1 mL of fresh media and 100 µL of this cell suspension is transferred to a new tube. 10 µL are removed and resuspended in 10 µL of Trypan Blue. The haemocytometer is prepared with coverslip and 10µL of Trypan Blue + cell suspension is added to the chamber. Viable (seen as bright cells) and non-viable cells (stained blue) are counted under the microscope and final cell concentration is determined using Equation 4.

$$\frac{\text{cells}}{\text{mL}} = 2 \times 10 \times 10.000 \times 1\text{mL} \quad (4)$$

### 2.6.3 Mouse fibroblast culture

L929 mouse fibroblasts with passaging numbers 11-14 were used. Culture media consisted of complete DMEM media supplemented with 10% FBS and 1% antibiotic. This media was changed every 3-4 days. In this case, a Trypsin-EDTA solution was used for cell passaging by incubation for 7 minutes followed by centrifugation for 7 minutes at 1250 RPM. Supernatant was removed and disposed, and cell pellet was resuspended with 1 mL of DMEM-media. Cells were then plated on a new flask to the desired concentration and/or used for bioprinting assays.

### 2.6.4 Imaging of cells.

All the bright-field and fluorescence images were taken using a Leica DMI3000B microscope, with 4x, 10x and 20x magnifications. At least 3 images were taken for each of the samples and analyzed using ImageJ software.

## 2.7. Viability assays

### 2.7.1. Live/Dead Assay

To analyse and quantify the viability of cells, live/dead fluorescence probes were used. For the staining of viable cells, a solution of 1:1000 in PBS of Calcein-AM (Sigma-Aldrich) was prepared. For dead cells, the solution consisted of 2:1000 in PBS of Ethidium-homodimer-1 (Sigma Aldrich). After media removal from the wells with the target cells, the prepared solution was added to each sample and left to incubate for 20-30 minutes. Culture plates were protected from direct light to prevent photobleaching events.

For cell seeding assays, sisECM, sisECM + 0.05% PEDOT:PSS and sisECM + 0.1% PEDOT:PSS bioink solutions were added to a 96-well plate and incubated at 37°C for 30 minutes until gellification was complete. To sterilise the hydrogels, a solution of 5% penicillin-streptomycin (Pen-Strep) in PBS was added and left overnight at 4°C. The prepared hydrogels can be seen in Figure 17.

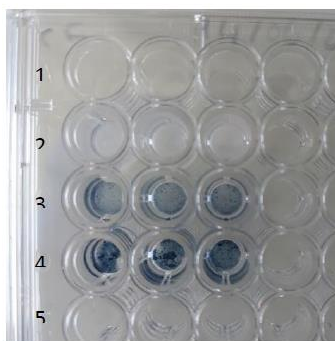


Figure 17 - 96-well plate for cell seeding assays; 1 - positive control; 2 - sisECM; 3 - sisECM + 0.05% PEDOT:PSS; 4 - sisECM + 0.1% PEDOT:PSS; 5 - negative control

### 2.7.2. Cardiomyocyte's immunostaining

Cells were fixed with a 4% paraformaldehyde (PFA) solution in PBS and left to react for 20 minutes. PFA was removed and wells were washed with PBS and stored at 4°C when immunostaining was not immediately proceeded.

After cell fixation, cardiomyocytes were immunostained. The first step was permeabilization, by the addition of 0.1% Triton x100 in PBS for 8 min at room temperature. After washing with PBS, 4% FBS in PBS was added for 1 h at room temperature for the blocking of non-specific binding. After washing with PBS, 1:1000 anti-TNNI3 (primary antibody, produced in mouse) in PBS was added and left overnight at 4°C and washed with 0.05% Tween 20 in PBS. 1:1000 anti-mouse FITC in PBS was added for 1h at room temperature and washed with 0.05% Tween 20 in PBS. The nucleus was stained using Hoescht 5 µL/mL in PBS at 37°C, followed by the washing with PBS. Finally, for actin staining, 1:150 phalloidin in PBS was added for 30 minutes at room temperature and washed with PBS.

## 2.8. Bioinks formulation and bioprinting

### 2.8.1. Bioink and gelatin sterilization for bioprinting

All materials, including tubes, pipette tips, needles and other support materials were sterilized on the laminar flow hood with UV light for 30 minutes prior to bioprinting.

For bioinks preparation, PEDOT:PSS and neutralization buffer were filtered with 0,22 µm filter (Millex-GV Syringe Filter Unit). All bioinks were then prepared under sterilized conditions on the laminar flow hood.

In the case of the gelatin support bath, the previous procedure described in section 2.1.3. was followed. After gelatin and CaCl<sub>2</sub> dissolution on heated sterilized water, the solution was filtered

using a 0.45  $\mu\text{m}$  filter (Millex-GV Syringe Filter Unit), on the laminar flow hood. The 0.16%  $\text{CaCl}_2$  solution was filtered using a 0,22  $\mu\text{m}$  filter (Millex-GV Syringe Filter Unit).

### 2.8.2. Bioink preparation for bioprinting

For cell bioprinting assays, L929 mouse fibroblasts were cultured according to section 2.7.3. For this, 2 mL of each bioink was prepared following the previously described protocol in sections 2.1.2 and 2.1.5 of this chapter. Cell suspension media was added to each bioink at a concentration of  $0.5 \times 10^6$  cells/mL. Structures of circular geometry ( $r=2.5$  mm) were printed. Bioink composition and printing parameters are described in Table 9. A schematic of this procedure can be found in Figure 18.

Table 91 - Printed structures attributes used for mouse fibroblasts' bioprinting.

| Attributes              | Values   |
|-------------------------|----------|
| Printing Speed          | 45 mm /s |
| Dispensing Pressure     | 0.1 psi  |
| Number of Layers        | 5        |
| Distance between layers | 0.05 mm  |
| Needle Diameter         | 0.57 mm  |

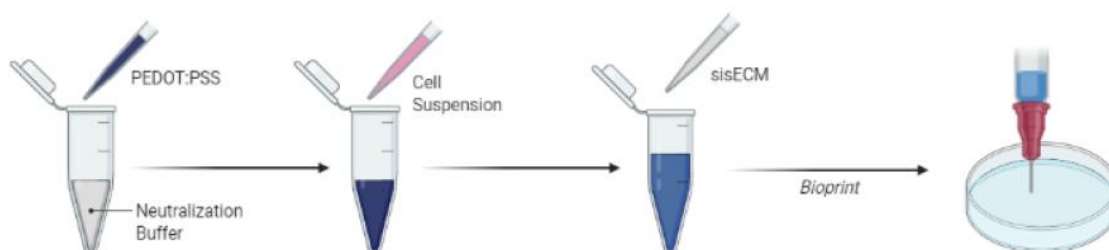


Figure 6 -- Bioink preparation for bioprinting schematic

## 2.9. Statistical analysis

Data is shown as mean  $\pm$  standard deviation of independent measurements or assays (at least  $n=3$  replicates were considered), and statistical analysis was performed using Microsoft Excel Software. Differences between experimental groups was analyzed by Student's T test. P values  $< 0.05$  were considered significant for all statistical tests.

## Chapter 3 - Results and Discussion

### 3.1. Optimization of bioinks composition

In the process of designing the bioinks, several PEDOT:PSS concentrations were tested according to results found in previous published studies<sup>109,110,112,172,173</sup>. It is important to note that the protocol that was followed to produce the sisECM hydrogels only works for final sisECM concentrations ranging from 6 to 8 mg/mL, which is why those were the limit concentrations that were tested (below 6 mg/mL gelation of the hydrogel did not allow for the self-support of the structures, leading to their collapse). On Table 10 an evaluation of all PEDOT:PSS concentrations used to cast hydrogels is presented, for an incubation time of 30 minutes at 37 °C for all conditions.

All hydrogels were evaluated based on an arbitrary scale taking into account three parameters: circularity, PEDOT:PSS dispersion and gelation:

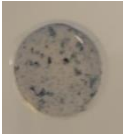
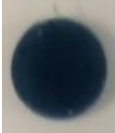
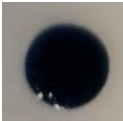
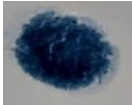
**A) Circularity:** The circularity of the hydrogels is related to the roundness of the structures as this was the shape of the mould, described in the Materials and Methods chapter. It can vary between 0.0 and 1.0, with 1.0 corresponding to a perfect circle and 0.0 to a non-circular shape. In our case, rounder samples indicate better self-support of the structures, as they have retained the shape of the mould. These values were calculated with ImageJ. To simplify the evaluation, an arbitrary scale was set from 1 to 3, with 1 being a non-circular shape (with circularity <0.5), 2 corresponding to an acceptable circularity (between 0.5-0.85) and 3 being a perfectly circular shape (0.85-1.0). Our results showed that for condition D, circularity was bad as the structure did not hold shape. Similarly, structures E and F showed low circularity. This is due to the higher PEDOT:PSS content and low sisECM concentration (6.01 and 6.00 mg/mL, respectively). On the other hand, conditions A, B and C showed high circularity results, not only due to lower PEDOT:PSS content but also high sisECM concentrations.

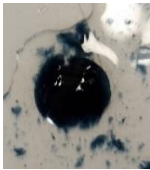
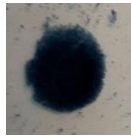


**B) PEDOT:PSS dispersion:** This is related to the homogeneity of the PEDOT:PSS aggregates on the hydrogels. These clusters are formed because the polymer chains are too big and due to the use of a simple mixing method that doesn't allow for perfect incorporation of the PEDOT:PSS in the sisECM. A hydrogel with low PEDOT:PSS dispersion will be discarded, whereas a highly homogeneous hydrogel can be selected for further testing. A scale was set from 1 to 3, with 1 corresponding to a badly dispersed hydrogel, 2 admissible distribution of clusters and 3 a very well homogenized hydrogel. As observed in Table 1, PEDOT:PSS dispersion was considered 1 for condition A, 2 for conditions D and F and 3 for the remaining conditions. It is verified that for conditions that had poor results in circularity, their PEDOT:PSS dispersion mark is also low. The same is verified with gelation results.

**C) Gelation:** Finally, the gelation outcome is related to formation of a self-sustaining gel after incubation for 30 minutes at 37°C and removal of the cast. A scale from 1 to 3 was set, with 1 relating to the lack of structural maintenance and lack of any type of gel after incubation, 2 being a structure that holds up the shape after cast removal, despite some dispersion due to

incomplete gelation and 3 corresponding to a completely gelled structure and the preservation of its shape. Gelation was considered incomplete for condition D due to a formulation with a higher PEDOT:PSS concentration, that led to a decrease in sisECM concentration in the final gel (6.4 mg/mL), and therefore the gelation process was not complete. Gelation was partially complete for conditions E and F and complete once again due to the higher PEDOT:PSS content and low sisECM concentration (6.01 and 6.00 mg/mL, respectively). On the other hand, for conditions A, B and C gelation was complete, not only due to lower PEDOT:PSS content but also because the sisECM concentration was above 7 mg/mL. To verify whether it was the PEDOT:PSS addition or the low sisECM concentration that was causing an under-gelation of the structures, condition G was prepared. As observed, the high PEDOT:PSS content did gelation. This means that for a complete gelation, sisECM concentration must be above 7 mg/mL. These results are in accordance with circularity results (Table 1). For the purpose of this study, two conditions were selected, sisECM + 0.05% PEDOT:PSS (B) and sisECM + 0.1% PEDOT:PSS (C). A control condition, sisECM, is also analyzed and compared with PEDOT:PSS hydrogels.

Table 10 - Different PEDOT:PSS and sisECM concentrations in final hydrogel tested; parameters classification scale: 1 – discarded; 2 – acceptable; 3 – ideal.

| Conditions | PEDOT:PSS content (%) | sisECM concentration (mg/ml) | Circularity | PEDOT:PSS dispersion | Gelification outcome | Results   |
|------------|-----------------------|------------------------------|-------------|----------------------|----------------------|---|
| A          | 0.01                  | 7.9                          | 3           | 1                    | 3                    |  |
| B          | 0.05                  | 7.6                          | 3           | 3                    | 3                    |  |
| C          | 0.1                   | 7.3                          | 3           | 3                    | 3                    |  |
| D          | 0.2                   | 6.4                          | 1           | 2                    | 1                    |  |

|   |      |      |   |   |   |   |
|---|------|------|---|---|---|---|
| E | 0.25 | 6.01 | 2 | 3 | 2 |  |
| F | 0.1  | 6.00 | 2 | 2 | 2 |  |
| G | 0.2  | 7.3  | 3 | 3 | 3 |  |
| H | -    | 8.0  | 3 | - | 3 |  |

---

### 3.2. Hydrogel characterization

After choosing the conditions for the rest of the experimental work, a series of tests were performed to understand if the hydrogels were suitable for cell viability.

#### 3.2.1 Hydrogel properties

##### 3.2.1.1 Water Content

Water content of the hydrogels was analysed. A high water-content is important in a hydrogel so that it better represents the *in vivo* natural environments (~70%)<sup>174</sup>. Results of water content of the 3 materials previously selected are presented in Figure 19. As expected, the higher the PEDOT:PSS concentration on the bioink, the lower the water content is on the respective hydrogel. However, even for the sisECM + 0.1% PEDOT:SS condition, water content is considerably high, mimicking more accurately the tissue microenvironment (97.25%). The water content of sisECM, sisECM + 0.05% PEDOT:PSS and sisECM + 0.1% PEDOT:PSS corresponded to  $98.10 \pm 0.10\%$ ,  $98.04 \pm 0.04\%$  and  $97.25 \pm 0.04\%$ , respectively.

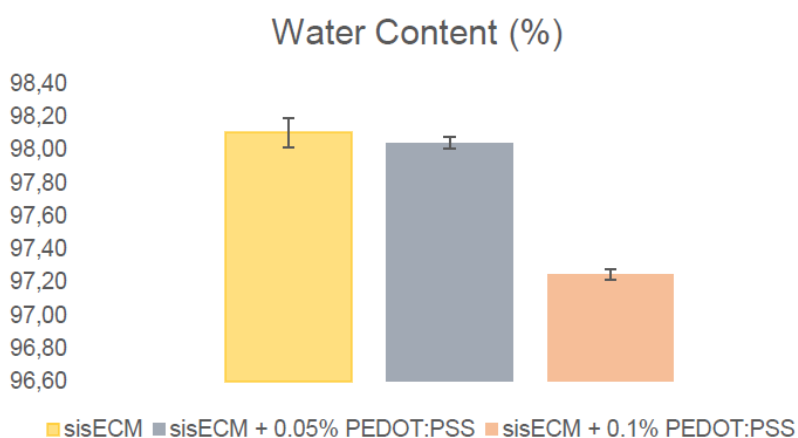


Figure 19 - Water content results for all three hydrogels; n= 3.

### 3.2.1.2. Stability of the casted structures

Hydrogel stability was evaluated through a period of 30 days. For this, casted hydrogels of all bioinks were stored at room temperature with PBS. During this time period, no observable deterioration of the structures was noticed, Figure 20, as confirmed by the calculation of their circularities, where variations are negligible (Table 11), making these hydrogels suitable for long term cell culture.

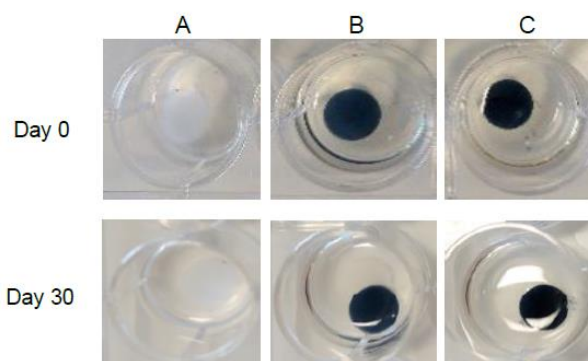


Figure 20 - Stability assay results for days 0 and 30 for all bioinks; A: sisECM; B: sisECM + 0.05% PEDOT:PSS; C: sisECM + 0.1% PEDOT:PSS.

Table 11 - Circularity values for sisECM, sisECM + 0.05%PEDOT:PSS and sisECM+0.1%PEDOT:PSS for days 0 and 30 of the stability assay for the casted structures.

| Condition | sisECM | sisECM + 0.05%<br>PEDOT:PSS | sisECM + 0.1%<br>PEDOT:PSS |
|-----------|--------|-----------------------------|----------------------------|
| Day 0     | 0.952  | 0.963                       | 0.968                      |
| Day 30    | 0.947  | 0.955                       | 0.962                      |

### 3.2.2 Electrical characterization

#### 3.2.2.1 Four-probe Method

For an evaluation of electrical conductivity of the materials, a four-probe method assay was performed on dry samples. Results are presented in Figure 21, where conductivity values



corresponded to  $7.87 \times 10^{-2} \pm 1.72 \times 10^{-3}$  S/cm,  $0.11 \pm 0.07$  S/cm,  $1.25 \pm 0.29$  S/cm for sisECM, sisECM + 0.05% PEDOT:PSS and sisECM + 0.1% PEDOT:PSS, respectively. As expected, conductivity of the materials increases with higher PEDOT:PSS concentrations. It is important to note however, that this assay is not the most accurate since it was performed on dry samples, rather than wet samples that are closer to the real conditions, where a combination of electronic and ionic currents is taking place. Nevertheless, it allows us to understand the contribution of PEDOT:PSS to increase the conductivity of the materials. This values, when compared to pure PEDOT:PSS (0.2-0.5 S/cm; 28 S/cm (wet) and 155 S/cm (dry)) or other conductive polymers (PANI: 0.1-0.2 S/cm; PPy: 0.02 S/cm) are within the range of values already recorded on previous works<sup>175</sup>.

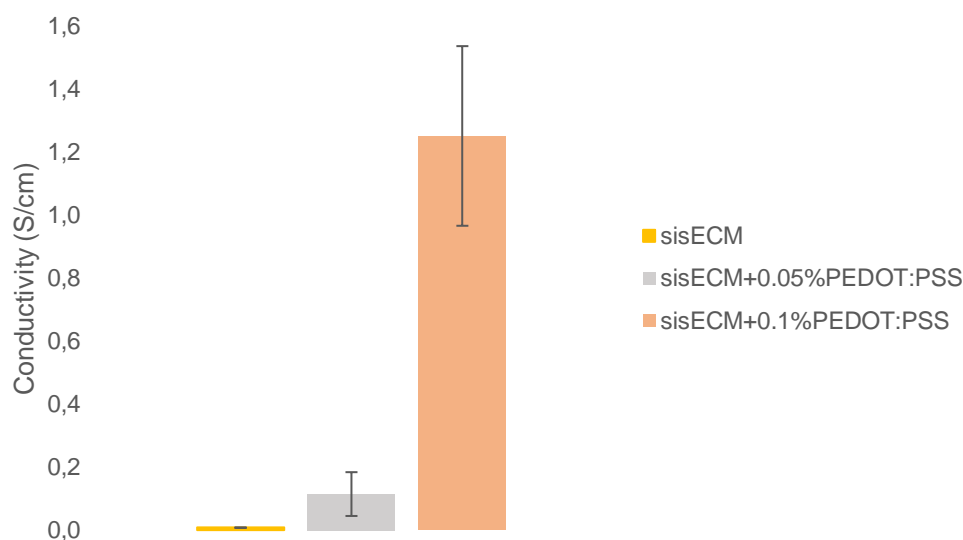


Figure 21 - Four-probe method results for conductivity for all hydrogels;  $n=5$ ;  $p < 0.05$  for Student's *t*-test

### 3.2.2.2. Preliminary conductivity assay

Electrical characterization of wet samples is more accurate, as this represents the whole complexity of the hydrogel microenvironment. A preliminary conductivity assay was performed on wet hydrogels, by using a multimeter with a fixed distance between tips. Results are presented in Figure 22. As expected, and as we observed in dry samples, the higher the PEDOT:PSS concentration on the hydrogel, the higher the conductivity. It is important to note that the conductivity of the sisECM hydrogel was also measured but was out of the multimeter limit. We could also observe that even the lowest PEDOT:PSS concentration of 0.01% possesses a quantifiable conductivity.

The values corresponded to  $0.17 \pm 0.01$  S/cm,  $0.24 \pm 0.02$  S/cm,  $0.63 \pm 0.13$  S/cm for sisECM + 0.01% PEDOT:PSS, sisECM + 0.05% PEDOT:PSS and sisECM + 0.1% PEDOT:PSS, respectively. The differences observed from this case to values in Figure 21, where electrical conductivity is lower for dry samples is related to the water content on wet samples, where water undergoes self-ionization that generates constant ionic flow on the hydrogels<sup>50</sup>.

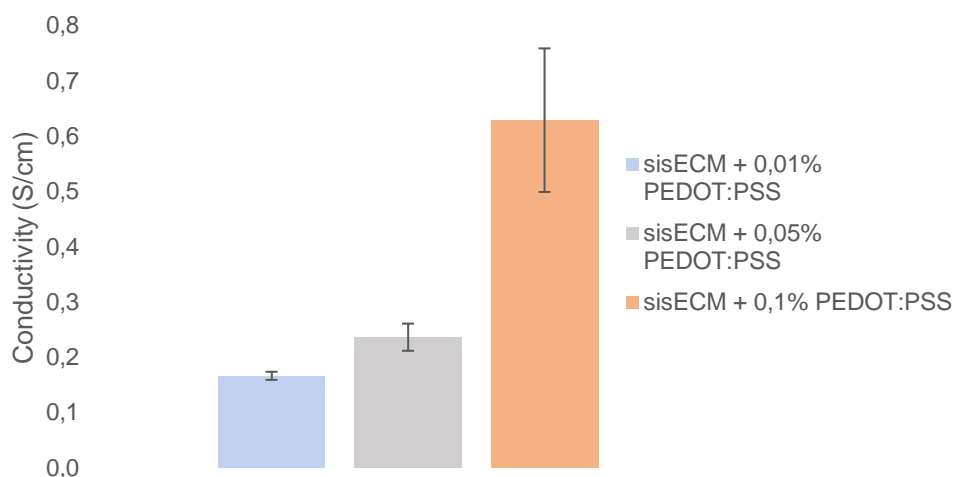


Figure 7 - Results for conductivity obtained for hydrogels with PEDOT:PSS concentrations of 0.01%, 0.05% and 0.1%; n= 5.

### 3.2.2.3. Electrochemical Impedance Spectroscopy (EIS)

EIS was performed to measure the electrical impedance of the hydrogels over frequencies between 0.1 Hz and 10 MHz. Besides the hydrogels, impedance of copper bands was also measured as a positive control for total passage of electrical current. Results can be found on Figures 23 and 24.

As expected, the higher the PEDOT:PSS concentration on the hydrogels, the lower the impedance to the passage of current. For example, at 10 Hz, the values of impedance corresponded to  $7767.5 \pm 4097.8 \Omega$ ,  $6309.6 \pm 1937.9 \Omega$  and  $5492.2 \Omega$  for sisECM, sisECM + 0.05% PEDOT:PSS and sisECM + 0.1% PEDOT:PSS. Impedances on the lower frequency range (until approximately 1000 Hz) usually correspond to the capacitive behaviour of the hydrogel and diffusion natural processes occurring within the biomaterial<sup>176,177</sup>. Electrochemical capacitors are electrochemical devices with fast and highly reversible charge-storage and discharge capabilities and are important for energy storage devices. For this study, a copper strip was used as a control, considering that this material behaves as a fully conducting material.

PEDOT:PSS presence causes a shift in the measured impedance for hydrogels where the polymer is present. However, for higher frequencies, impedance of all hydrogels converges towards a stable value (that is higher with increasing PEDOT:PSS concentrations), meaning that it no longer has the capacity to accumulate charge and all electrical current passes through and behave like resistors (materials that oppose to the passage of current). For frequencies higher than 10 000 Hz, values stabilize towards  $161.67 \pm 4.17 \Omega$ ,  $105.22 \pm 2.31 \Omega$  and  $89.60 \pm 3.67 \Omega$  for sisECM, sisECM + 0.05% PEDOT:PSS and sisECM + 0.1% PEDOT:PSS, respectively.

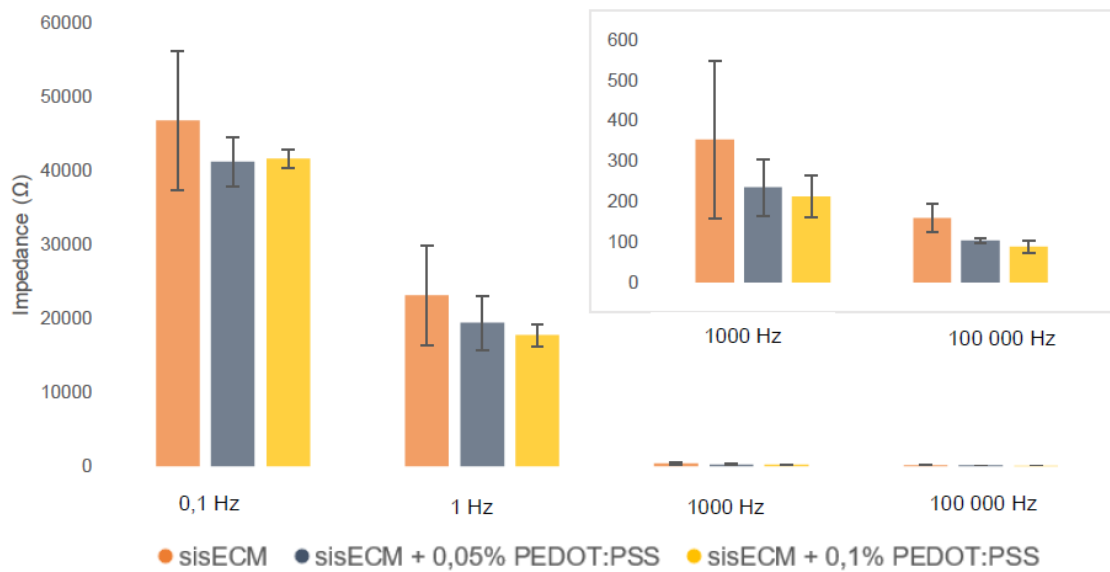


Figure 23 - Impedances for frequencies 0.1; 1; 1000 and 100000 Hz for sisECM, sisECM + 0.05% PEDOT:PSS and sisECM + 0.1% PEDOT:PSS hydrogels; n=6.

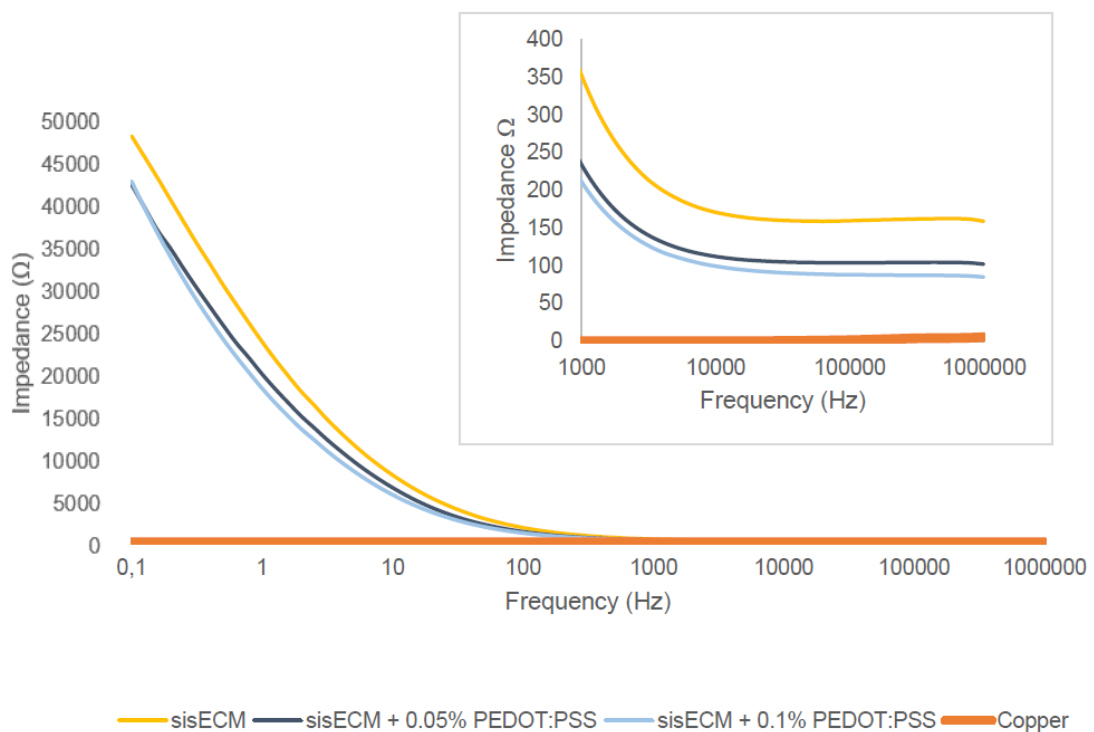


Figure 24 – Impedances measured of all hydrogels and copper

### 3.3. Optimization of the bioprinting conditions

#### 3.3.1 Rheological Characterization of the bioinks

A rheological analysis was performed through an oscillating time sweep assay to evaluate the bioink properties, including storage and loss modulus,  $G'$  and  $G''$  respectively, loss factor ( $\tan \delta$ ) and viscosity,  $\eta$ .

Results for storage and loss moduli can be found in Figure 25. As expected, for all conditions, it was observed that the storage modulus (elastic/solid state portion of the viscoelastic behavior) is higher than the loss modulus (viscous/liquid-state portion of the viscoelastic behavior), meaning that the transition from a solution to a gel was completed. Also, the higher the PEDOT:PSS concentration, the higher the initial and final values for both moduli. For the storage modulus,  $G'$ , the initial values correspond to  $0.31 \pm 0.13$  Pa,  $9.09 \pm 2.35$  Pa and  $44.90 \pm 26.88$  Pa and the final values correspond to  $95.68 \pm 22.69$  Pa,  $112.04 \pm 32.72$  Pa and  $125.34 \pm 32.87$  Pa for sisECM, sisECM + 0.05% PEDOT:PSS and sisECM + 0.1% PEDOT:PSS, respectively. For the loss modulus,  $G''$ , the initial values correspond to  $0.64 \pm 0.16$  Pa,  $3.06 \pm 0.38$  Pa and  $11.56 \pm 6.69$  Pa and the final values correspond to  $13.77 \pm 2.74$  Pa,  $16.66 \pm 5.74$  Pa and  $18.54 \pm 6.46$  Pa for sisECM, sisECM + 0.05% PEDOT:PSS and sisECM + 0.1% PEDOT:PSS, respectively.

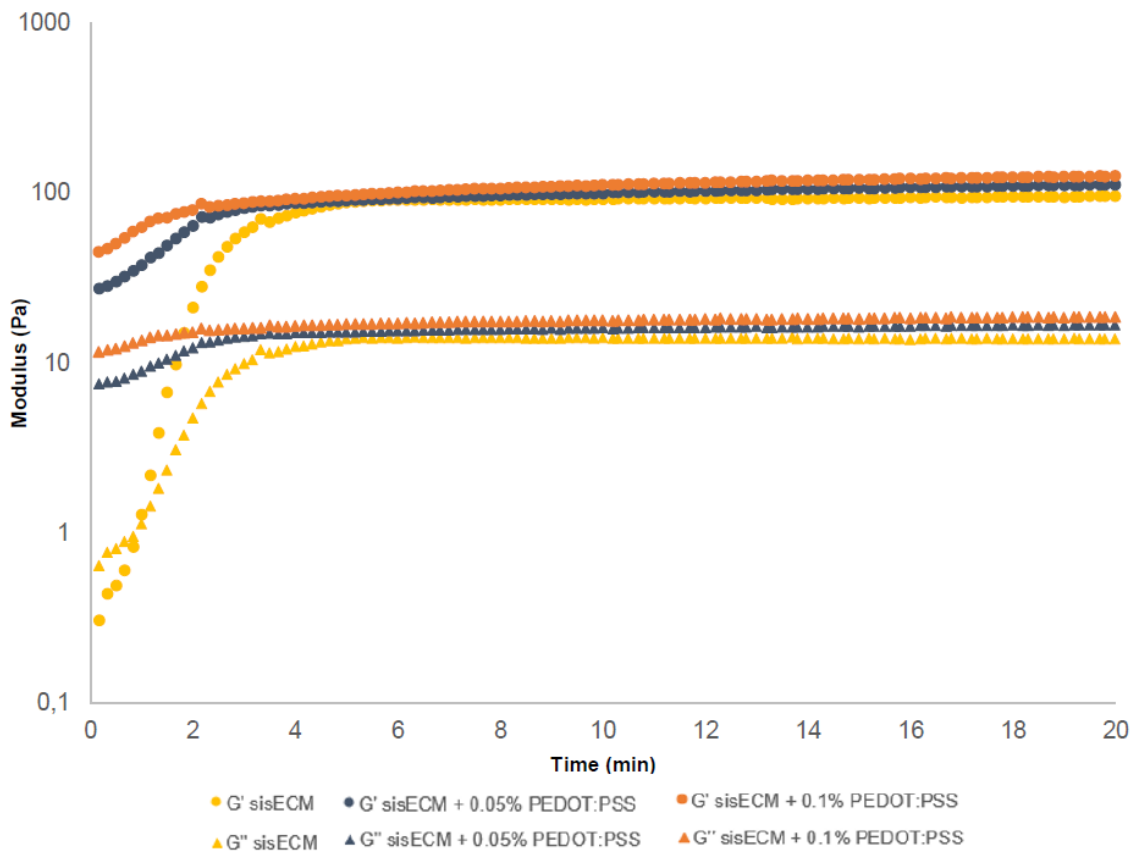


Figure 258 - Oscillating time sweep results for all bioinks; Variation of storage and loss modulus through time;  $n=3$ ;  $p < 0.05$  for Student's  $t$ -test.

The gel point can be defined as the time at which the system loses fluidity and increases in viscosity and the fluid becomes solid like. It can be determined by the intersection of storage and loss modulus' curves. We could observe that in bioinks containing PEDOT:PSS the gelation process was faster than in plain sisECM inks. In the sisECM bioink the gelation point corresponds to 0.833 minutes as can be seen in Figure 26. For the other two bioinks, the gelation point was taking place before the measurement was taking place, indicating that the gelation started almost immediately after the addition of the different elements of the bioink at 4°C. This is theorized to happen due to mixing of PEDOT:PSS on the bioinks, that due to the low volume prepared increases temperature that contributes to gelation. Also, PEDOT:PSS might bond immediately with the ECM and promoting polymerization.

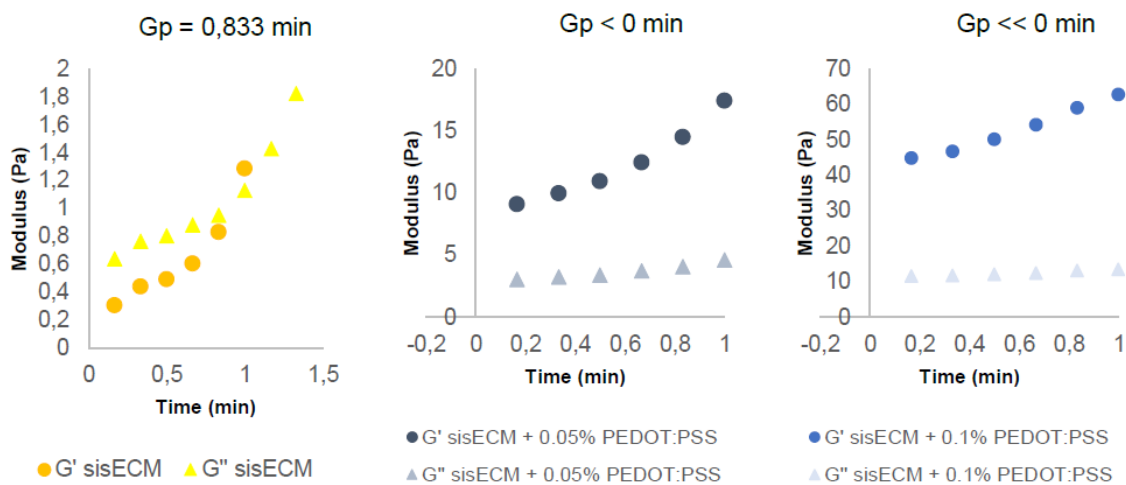


Figure 26 - Gel point graphs for each bioink

Loss factor ( $\tan \delta$ ) and complex viscosity were also obtained. Loss factor relates to the energy dissipated during the sol-gel conversion and gives us information about the relation between potential energy and kinetic energy<sup>47,178</sup>. It can be calculated by the ratio between loss modulus  $G''$ , that characterizes the deformation energy lost through internal friction when flowing, and the storage modulus  $G'$ , that represents the stored deformation energy. As expected, at time point 0 and until 2 minutes, the sisECM bioink portraits a  $\tan \delta$  higher than the bioinks with PEDOT:PSS ( $2.25 \pm 0.57$ ,  $0.36 \pm 0.05$  and  $0.26 \pm 0.01$  for sisECM, sisECM + 0.05% PEDOT:PSS and sisECM + 0.1% PEDOT:PSS, respectively for time point 0). This result indicates that the material behaves more liquid-like (as validated by previous results where it takes more time for gelation to occur) and the higher the PEDOT:PSS concentration, the lower the initial loss modulus, meaning that the sample is closer to a gel than a fluid (confirmed by gel point results). After complete gelation of all bioinks,  $\tan \delta$  stabilizes towards the same value ( $0.14 \pm 0.01$ ,  $0.15 \pm 0.01$  and  $0.15 \pm 0.01$  for sisECM, sisECM + 0.05% PEDOT:PSS and sisECM + 0.1% PEDOT:PSS, respectively).

An analysis of the complex viscosity of the bioinks is important in bioprinting, as excessive viscosity values are directly related to a higher shear stress that could cause some harm to cells

and reduce their viability values. Complex viscosity is a measure of the total resistance to flow as a function of angular frequency<sup>179,180</sup>. The initial viscosity values of the sisECM, sisECM + 0.05% PEDOT:PSS and sisECM + 0.1% PEDOT:PSS corresponded to 0.11±0.03 Pa.s, 1.53±0.37 Pa.s and 7.38±4.41 Pa.s, respectively. These values stabilized after 5.67 minutes in sisECM, 3.5 minutes in sisECM + 0.05% PEDOT:PSS and 4.0 minutes in sisECM + 0.1% PEDOT:PSS reaching the final values of viscosity of 15.39±3.64 Pa.s, 18.03±5.28 Pa.s and 20.17±5.32 Pa.s for sisECM, sisECM + 0.05% PEDOT:PSS and sisECM + 0.1% PEDOT:PSS, respectively. The average values obtained for complex viscosity range from 2.5-15 Pa.s<sup>181-183</sup>, and so the values obtained are acceptable in bioprinting and should not cause a shear stress that would compromise the viability of the bioprinted cells. Results for loss factor and complex viscosity are presented in Figure 27.

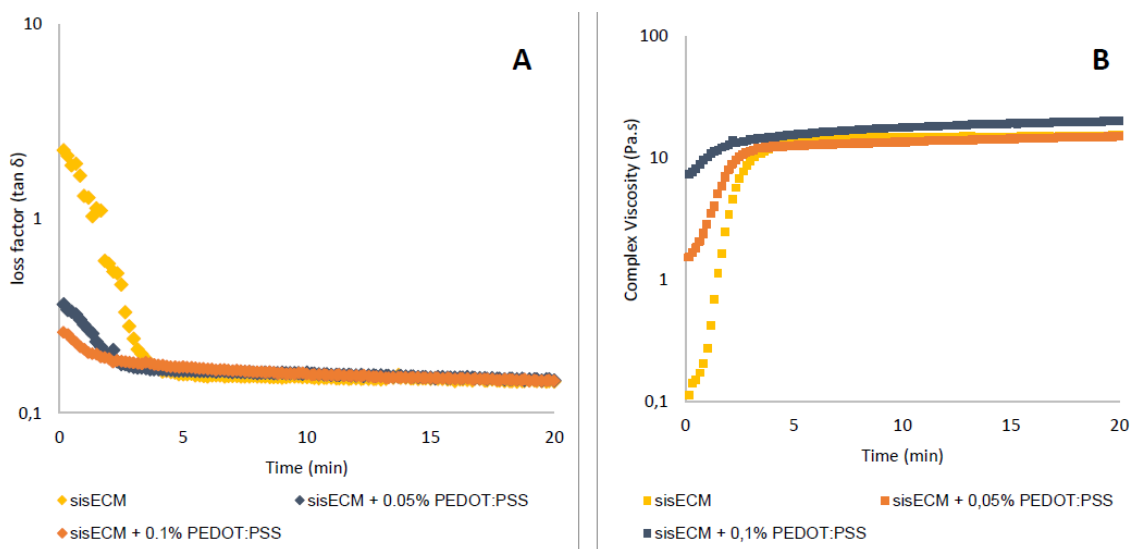


Figure 27 - Results for A: loss factor  $\tan \delta$  and B: complex viscosity through time for all bioinks;  $n=3$ .

### 3.3.2. Tuning of bioprinting parameters

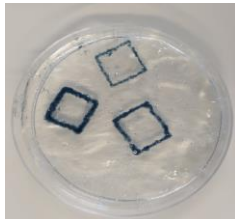
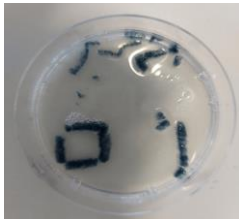
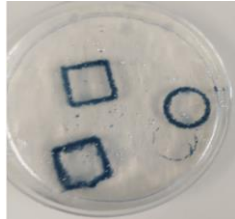

When printing there are some parameters that need to be considered and adjusted for optimal printing conditions that include: needle diameter to control resolution and levels of stress that cells might endure during the printing process; printing speed and dispensing pressure to control the amount of material being extruded (high pressures and low printing speeds cause too much material to be extruded limiting the final structure resolution); distance between layers to guarantee a compact structure (higher distance between layers can produce a structure that is not connected, and low distance between layers can cause an overlap between layers, leading to a deformed structure); number of layers to make sure that the printing structure is self-standing but does not collapse; and temperature to prevent gelation before printing.

First of all, simple structures were printed to understand the printability conditions of the bioinks. The selection of the preliminary parameters was based on previous works<sup>181,184-186</sup> for example, dispensing pressures lower than 10 psi and printing speeds varying between 1 – 10 mm/s.

It was observed that the higher the PEDOT:PSS concentration on the bioink, the higher the dispensing pressure during the printing process. This is due to the inability to perfectly homogenize and disperse the PEDOT:PSS on the bioink, and so some clogging happened, leading to the use of higher pressures. Also, as verified with rheology assays (section 3.2.3), viscosity increased with the addition of PEDOT:PSS, leading to increased dispensing pressures.

For bioinks gelification and gelatin removal, the printed structures were incubated at 37°C until gelatin was completely melted. Then, liquid gelatin was removed, and PBS solution was added to keep the printed structures hydrated during storage. However, despite the printing process being successful, when we proceeded to remove the gelatin some damaged was caused to the structures due to the fragility of the sisECM hydrogels. Some results of the optimal printing parameters used and structures before and after gelatin removal are presented in Table 12.








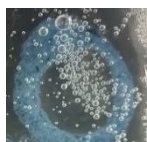


Table 12 - Printing attributes for sisECM + 0.1% PEDOT:PSS bioink; results before and after gelatin removal.

| Parameters   | Before gelatin removal  | After gelatin removal   |
|--|---|---|
| Printing Speed: 1-2.5 mm/s<br>Dispensing Pressure: 1-2.5 psi<br>Number of Layers: 5<br>Distance between layers: 0.05 mm<br>Needle Diameter: 0.3 mm<br>Geometry: square (L=10 mm); circle (r=5mm) |   |   |
|  |  |  |

As mentioned before, the process of removing the gelatin was not allowing for the maintenance of printed structures. Because of this, several changes were introduced. First, all the plasticware required (needles, tubes, petri dish) was kept in the freezer at -20°C until immediately before printing to prevent gelation of the bioinks due to a lack of temperature control on the bioprinter. All reagents used, including the gelatin, sisECM, neutralization buffer and CaCl<sub>2</sub> solution were also kept at low temperatures (at 4°C) until immediately prior to use. Then, after printing, a 1% CaCl<sub>2</sub> solution was added on top of the gelatin to aid with the crosslinking of the sisECM hydrogel, as calcium is important in the assembly of ECM and binds to many ECM proteins, including laminin, fibrillin and collagen, forming tightly held junctions between the calcium ions and α-L-galuronic acid monomers (Chapter 1, section 1.4.). During the melting process of the gelatin, the printed structures were placed in the incubator at 37°C instead of the heating plate, to ensure homogeneous melting of the gelatin and complete polymerization of the hydrogel. Finally, PBS was added simultaneously to the removal of the liquified gelatin, to avoid an overstretching the structures that could compromise their structural integrity.

For the printing of the structures, instead of using a needle with 0.3 mm diameter, a 100 mL pipette tip was used, with a diameter of 0.57 mm. This improved the robustness of the printed constructs, especially for the bioinks with PEDOT:PSS, because aggregates of PEDOT:PSS were clogging the needle and compromising the printing process, and consequently the dispensing pressures lowered, and printing speeds increased (printing parameters can be found in Table 13). Also, because the corners of the structures were more prone to damage, structures with circular geometry were printed. Finally, distance between layers was also decreased, from 0.05 mm to 0.02 mm.

Table 13 - Printing speeds and dispensing pressures optimization for sisECM + 0.1% PEDOT:PSS bioink; circular geometry ( $r=5\text{mm}$ ).

| Dispensing Pressure (psi) | Printing Speed (mm/s) | Before gelatin removal   | After gelatin removal   |
|---------------------------|-----------------------|--|---|
| 0.1                       | 15                    |    |    |
| 0.5                       | 25                    |  |  |
| 0.5                       | 35                    |  |  |
| 0.5                       | 45                    |  |  |
| 0.5                       | 55                    |  |  |

Therefore, besides the changes in the printing process and gelatin removal mentioned above, the optimal printing speeds were considered to be 25-55 mm/s and dispensing pressure of 0.5



psi. With maintained dispensing pressure, the lower the printing speed, the more bioink was extruded and less resolution the printed structure had (as seen in Table 4, where a printing speed of 25 mm/s resulted in a structure with a thicker border – 1.52 mm - and using a printing speed of 55 mm/s lead to a structure with a thinner border – 0.92 mm. When compared to the expected value – 0.57 mm (diameter of the pipette tip), we can verify that the higher the printing speed, the more accurate the final structure, due to a more controlled printing process.

### 3.3.3. Evaluation of the printability

The printability of a bioink is directly related to the ability to control the bioink deposition and structural performance of the extruded bioinks. In the next section, an analysis on shape maintenance and filament characterization was performed.

#### 3.3.3.1. Uniformity factor

The uniformity factor (U) was used to determine the uniformity between the printed strands and a theoretical perfectly uniform strand. For comparison, printed structures only had one layer. Each bioink was printed at 25 mm/s printing speed and 0.1 psi extruding pressure.



Figure 28 - Pictures of singles strands of sisECM (left), sisECM + 0.05% PEDOT:PSS (center) and sisECM + 0.1% PEDOT:PSS (right); scale bar 5 mm.

The uniformity factor was determined by dividing the length of the printed strand by the length of a uniform strand - in this case measured as a straight line on both sides of the printed strand, Equation 3. A uniform strand will have a uniform factor  $U=1$  and a nonuniform strand will have a uniformity factor  $U>1$ . In our case, the measurements were taken before the gelatine removal in order to avoid the deformation of the structures when gelatine is removed. This may lead to a loss in the quality of the images obtained. In the future, additional images might be taken to correct this.

As seen in Figure 28, no structures are completely uniform, with values corresponding to a uniformity factor of  $1.12 \pm 0.07$  for sisECM,  $1.07 \pm 0.07$  for sisECM + 0.05% PEDOT:PSS and  $1.06 \pm 0.01$  sisECM + 0.1 % PEDOT:PSS, where the uniformity factor got closer to 1 with increasing PEDOT:PSS content (Figure 29).

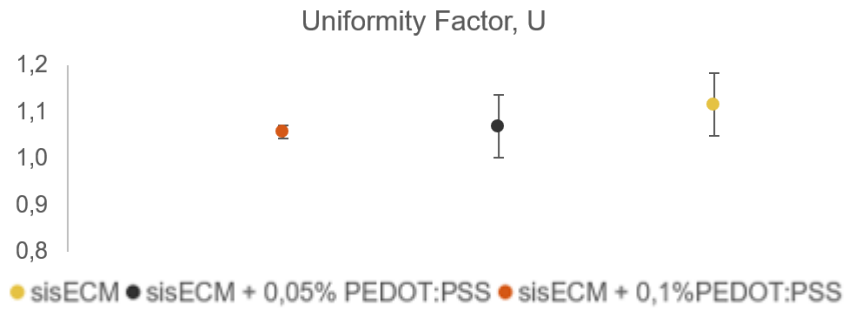


Figure 29 - Uniformity factors for all three bioink conditions;  $n=6$ .

This can be expected as sisECM has higher water content and lower viscosity that leads to a loss in printing resolution and consequently does not allow for the maintenance of form and the ink disperses in the gelatin.

However, because the uniformity factor values of all conditions are still close to 1, the bioprinted structures were still considered adequate.

$$U = \frac{\text{length of printed strand}}{\text{length of straight strand}} \quad (3)$$

### 3.3.3.2 Pore factor

The pore factor (Pr) was used to compare the printed structures to the CAD designs and how well they matched. For comparison, printed structures only had one layer. Each bioink was printed at 25 mm/s printing speed and 0.1 psi extruding pressure. Due to bioink dispersion on the gelatin, it is visible some deformity of the squares, with some pores even resembling a circular geometry rather than a square one (Figure 30).

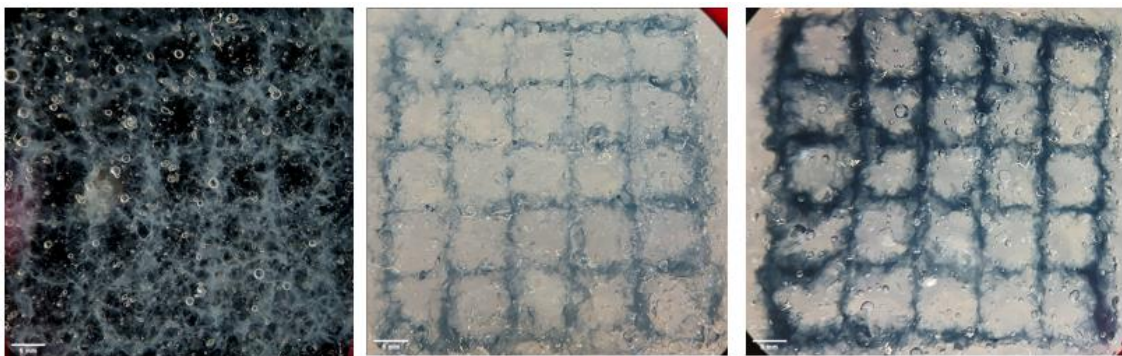


Figure 9 - Pictures of printed square meshes of sisECM (left), sisECM + 0.05% PEDOT:PSS (center) and sisECM + 0.1% PEDOT:PSS (right); scale bar 5 mm.

The pore factor was determined using Equation 2. Under-gelated bioinks will have a  $Pr < 1$ , properly gelated bioinks will have  $Pr = 1$  and over-gelated bioinks will have a  $Pr > 1$ . Contrary to what is expected to happen, the lower the PEDOT:PSS concentration on the bioink the closer the Pr is to 1, as verified through the results in Figure 31, though this variation is not very noticeable. However, the higher the PEDOT:PSS concentration is in the bioink, more particles are present in the bioink and the more difficult it is to print, resulting in a more irregularly

consistent final printed structure. As observed in Figure 30, for sisECM the pores are mostly equal to each other – also verified by the results for area and perimeter of each pore – whereas for sisECM + 0.1% PEDOT:PSS not all pores are equal – area and perimeter of pores on the left of the mesh vary substantially from those on the right of the mesh, for example . The pore factor for sisECM, sisECM + 0.05% PEDOT:PSS and sisECM + 0.1% PEDOT:PSS are  $1.006 \pm 0.01$ ,  $1.009 \pm 0.01$  and  $1.011 \pm 0.01$ , respectively (Figure 24). Therefore, variability and deformity of the square pore is greater in the sisECM + 0.1% PEDOT:PSS bioink.

$$Pr = \frac{(pore\ perimeter)^2}{16 * pore\ area} \quad (2)$$

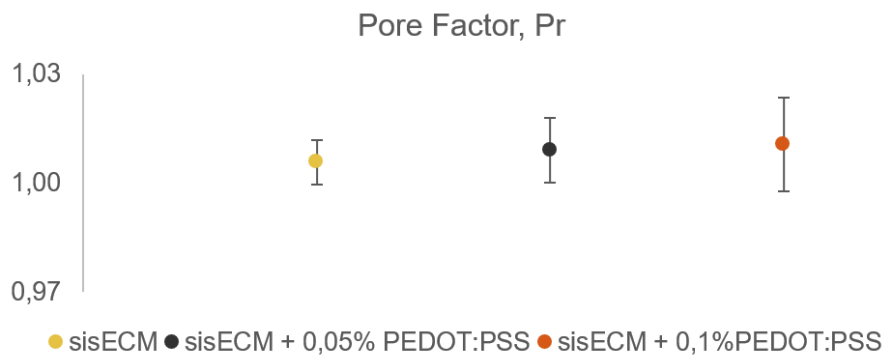


Figure 31 - Pore factors for all three bioink conditions; n=25.

### 3.3.3.3. Wall thickness and Pore size

Wall thickness and pore diameter were also determined for each printed structure and compared to the dimensions of the original design. The printed structures used were the same as the ones used for pore factor determination. The results are presented in Table 14 and show that the higher the PEDOT:PSS concentration, the lower the wall thickness is and the higher the pore diameter is. These results are in accordance with what was expected, because the higher the PEDOT:PSS concentration, the higher the viscosity and the less the bioink disperses in the gelatin, and so there is less variation to the intended dimensions, with wall thickness of 0.57 mm and pore diameter of 16 mm.

Table 24 - Results for wall thickness and pore diameter for each bioink, as well as their respective deviations to the intended dimensions.

| Bioink              | sisECM +<br>0.1% PEDOT:PSS | sisECM +<br>0.05% PEDOT:PSS | sisECM       |
|---------------------|----------------------------|-----------------------------|--------------|
| Wall Thickness (mm) | 1.02 ± 0.29                | 1.06 ± 0.32                 | 1.44 ± 0.35  |
| Pore Diameter (mm)  | 11.45 ± 1.17               | 11.37 ± 0.99                | 10.86 ± 1.01 |
| WT (%)              | 78.9                       | 85.4                        | 152.4        |
| PD (%)              | 28.4                       | 28.9                        | 32.1         |

### 3.4. Preliminary cell viability studies on the different hydrogel materials

In this part of the work, the main goal was to establish the scaffolds as viable platforms for cell proliferation and maintenance. For that purpose, proof-of-concept studies were performed using mouse fibroblasts. Once the viability of the fibroblasts was confirmed, this was also performed on hiPSC-CMs.

#### 3.4.1. Mouse fibroblasts

Initially, these cells were selected as they are frequently used in cytotoxicity evaluations, and they can be easily cultured and grown.

L929 mouse fibroblasts were seeded on the different hydrogels to discard any cytotoxic effects derived from the materials. Cells cultured on a control material (96-well plate) were used as a positive control. Hydrogels were casted in 96-wells and incubated to induce their gelation. These were then sterilised following the previously described protocols (See section 2.2.7. of Chapter 2). 10 000 cells were seeded per well for all conditions and at least 5 wells per condition were used.

After cells were seeded on the different materials, their growth was followed throughout a week. Images were taken of the different samples and cells were counted. Images of the cells cultured on the different materials can be seen in Figure 32. On day 0, cells cultured on all conditions exhibited a rounded morphology, a characteristic of Trypsin-EDTA action for cell detachment. For cells cultured on the control material, from day 1 onwards the cells take a fusiform and spindle-shape typical of fibroblasts. The same morphology is observed for cells cultured on sisECM and sisECM + 0.05% PEDOT:PSS from day 3 onwards. However, for cells cultured on sisECM + 0.1% PEDOT:PSS hydrogels, cells always maintain a round morphology. The round shape is a characteristic of the early stages of cellular adhesion but this morphology at longer time is associated with low attachment of cells to the surface. Also, for all conditions, cell division started on day 1 of cell culture.

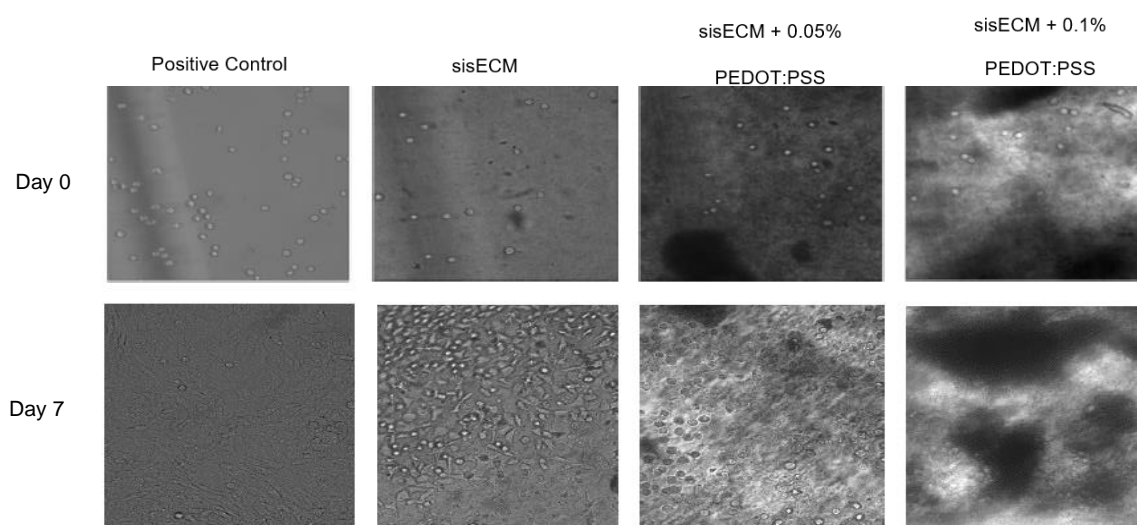


Figure 32 - Pictures taken with Leica microscope (10x magnification) of fibroblasts seeded on the 3 different hydrogels and positive control. Days 0 and 7 of cell culture.

From the previous images, a growth curve and fold increase curves were elaborated, Figure 33.

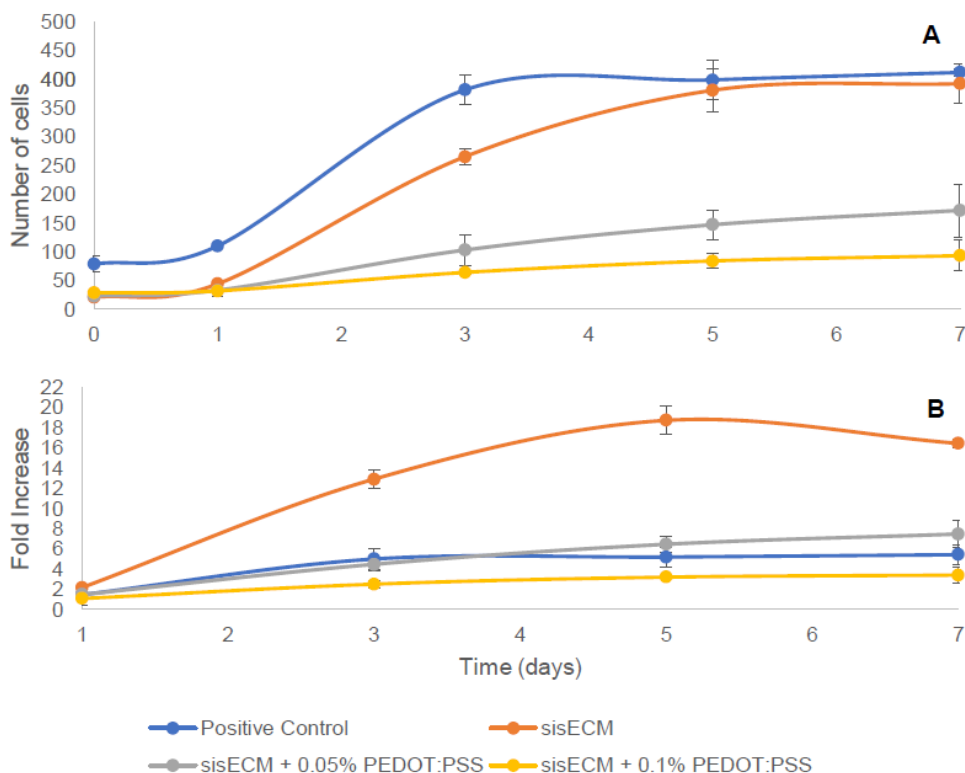


Figure 10 - Cell viability assays for mouse fibroblasts, culture for 7 days, for cell seeding in sisECM, sisECM+0.05% PEDOT:PSS and sisECM+0.1%PEDOT:PSS hydrogels; A: growth curve; B: Fold-increase curve; n=6.

In all cases, the cell number increased after 7 days of culture, however this increase was more pronounced in the sisECM, where the final values in cell numbers were similar to the controls corresponding to 412 and 392, respectively. As observed on the growth curve (Figure 33, A), there is a difference in the initial number of cells seeded on day 0 for the control condition and the hydrogels (10.000 cells were seeded per well in all conditions). This difference relates to the fact that the cells that were counted on the hydrogels only relate to a portion/plane of the hydrogel, that is a 3D structure, and not all cells dispersed on the hydrogel, whereas for the positive control condition, the cell culture was 2D and this effect doesn't happen. This effect can be observed on the images in figure 16, particularly on the sisECM hydrogel for day 7, and also affect the number of cells counted for all hydrogel conditions, where the images are out of focus, limiting the quality of the images compared to 2D cultures. Also, it is to note that from day 3 until day 7, the number of cells for the control conditions plateaus. This happens because cells reached full confluence and there was no more space for cells to grow.

In the materials containing PEDOT:PSS, the growth of cells was more limited. This is hypothesised to be caused by the lower cell adhesion on the conditions where PEDOT:PSS was present. Also, as seen in Figure 15, for conditions with PEDOT:PSS, the cells that adhered to the hydrogel did so in the sisECM part of the hydrogel, staying away from the PEDOT:PSS aggregates (the higher the PEDOT:PSS content, the lower the cell growth). This coupled with

the limitation of only being able to capture some planes of the hydrogels lead to a lower cell count.

Cell viability was also analysed with a LIVE/DEAD assay on day 7. The LIVE/DEAD assay is a quantitative assay for assessment of cell death. Living cells can be distinguished from dead cells by the accumulation of calcein AM, which is only retained in live cells and produces an intense green fluorescence. On the other hand, dead cells are identified using ethidium homodimer, that only infiltrates on cells with damaged plasma membrane, and can be identified by its red colour under fluorescence microscope (Figure 34). The results for sisECM, sisECM + 0.05% PEDOT:PSS and sisECM + 0.1% PEDOT: are  $96.7\pm0.39\%$ ,  $98.1\pm0.42\%$  and  $98.7\pm0.21\%$ , respectively. For the positive control, cell viability is  $99.40\pm0.09\%$  (Figure 35). As observed, the higher the PEDOT:PSS concentration, the higher the cell viability. This is theorized to happen due to high cell number in the sisECM hydrogels (from days 1 to 7) when compared to PEDOT:PSS hydrogels, where cell confluence and limited nutrients might have led to cell death by the end of the 7 days. However, viabilities in all conditions are very high, with value of for sisECM, sisECM + 0.05% PEDOT:PSS and sisECM+0.1% PEDOT:PSS, respectively, confirming that not only do the scaffolds allow for cell proliferation, but also cell maintenance.

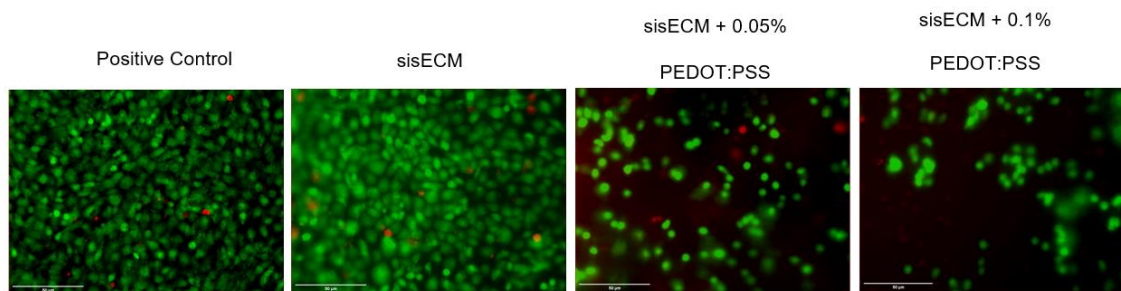


Figure 34 - Pictures taken with Leica fluorescence microscope (20x magnification) of fibroblasts seeded on the 3 different hydrogels and positive control on day 7 of cell culture. Green cells (alive) are stained with calcein-AM red cells (dead) with ethidium homodimer-1; scale bar 50  $\mu$ m

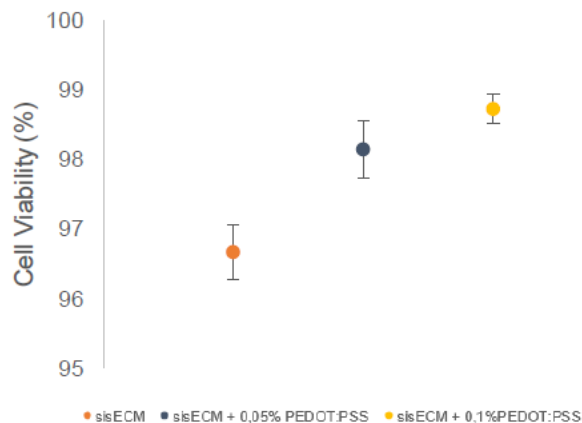


Figure 35 - Viability results for cell seeding of fibroblasts for all 3 hydrogels; n=6



### 3.4.2. hiPSC-CMs

After establishing that the hydrogels are suitable for cell viability, experiments with cardiomyocytes were performed. Cardiac cells were used in this study because of the potential of this material in cardiac tissue engineering, not only due to the hydrogels' suitable electrical conductivity (described in section 1.3.3. of Chapter 1 and section 3.2.2. of Chapter 3), but also because of their similarity to natural tissue biological and chemical properties. Therefore, their tunable properties and cell adhesion and growth support make them an ideal material for directing cells into functional cardiac tissues.

These cells were differentiated from hiPSCs following previous protocols. The differentiation process consists on a monolayer differentiation approach based on the use of growth factor and small molecules added to the medium, where hiPSCs are grown in a 2D monolayer, allowing for the scalable differentiation of a large quantity of cells. This process can be divided into 4 parts: preparation, pre-conditioning, differentiation, and maintenance of cells until dissociation. Day 0 is considered to be on the first day of the differentiation step, and so preparation happens on days -3 and -2, and pre-conditioning happens on day -1. On the preparation step, cells are seeded on a Matrigel coated surface containing Essential 8 (E8)-ROCK inhibitor media (Figure 36) . Matrigel is a solubilized basement membrane preparation extracted from the Engelbreth-Holm-Swarm (EHS) mouse sarcoma, rich in several ECM proteins and growth factors, that promotes attachment and differentiation of cells. E8 media is xeno-free and feeder-free media tailored for hiPSCs growth and expansion. Rock inhibitor (Rho-associated protein kinase) is added to prevent dissociation-induced apoptosis by phosphorylating and activating the myosin II pathway.



*Figure 36 - hiPSC cells on day -2 of the preparation step of cardiomyocyte differentiation. Photo taken with Leica microscope, at x10 magnification; scale bar 100 μm*

On the pre-conditioning step, media is replaced by StemPro34 media, a serum-free media formulated to support the development of human hematopoietic cells in culture, supplemented with BMP4 and Matrigel (Figure 37). The BMP4, bone morphogenic protein, is a human recombinant protein used to activate different signaling pathways related to the stimulation of some inhibitor of differentiation genes (at an early stage of the differentiation process) and also the up regulation of cardiac transcription factors, promoting cardiomyocytes differentiation (later stage of the differentiation stage)<sup>187</sup>.

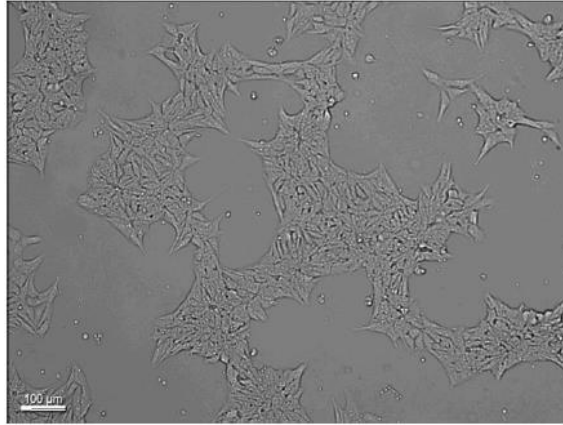


Figure 37 - hiPSC cells on day -1 of the pre-conditioning step of cardiomyocyte differentiation, presenting cheese-like morphology. Photo taken with Leica microscope, at x10 magnification; scale bar 100  $\mu\text{m}$

On the differentiation step, cells are initially cultured for two days with StemPro 34 media with L-glutamate, supplemented with BMP4 and Activin A, that induces cardiomyogenic and appearance of rhythmically beating cells<sup>188</sup>. At this point, cells start to have a cheese-like morphology (Figure 38).

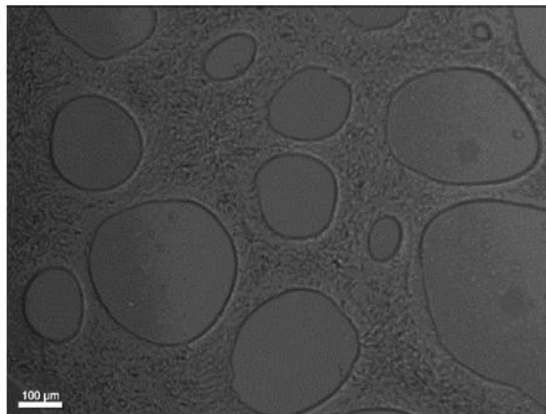


Figure 11 - Cells on day 0 of the differentiation step of cardiomyocyte differentiation. Photo taken with Leica microscope, at x10 magnification; scale bar 100  $\mu\text{m}$

The media is then changed to RPMI media, that has high concentrations of vitamins, and no proteins, lipids, or growth factors, without insulin (insulin inhibits cardiomyocytes yield during the first 5 days of hiPSCs differentiation<sup>189</sup>), supplemented with KY02111 and XAV939, WNT inhibitors that promote hiPSCs differentiation into cardiomyocytes. At this stage, cells started spreading across the surface area and changed morphology (Figure 39A) . From day 6 onwards, media is be changed every two days with RPMI-B27 media (with insulin) (Figure 39B). From day 8 or 9 cells may start beating (this can happen later).



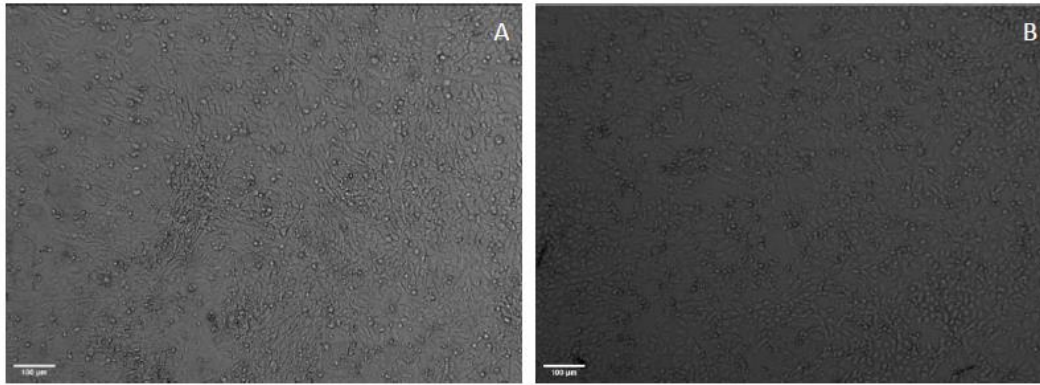


Figure 39 - Cells on days 4 (A) and 6(B) of the differentiation step of cardiomyocyte differentiation. Photos were taken with Leica microscope, at x10 magnification; scale bar 100 µm

Three different batches of cardiomyocytes were prepared. The yield of the first differentiation, meaning the % of cells on the plate that were actually cardiomyocytes (fibroblasts can easily be differentiated from hPSCs) was calculated, and a value of  $86\pm 3\%$  of cardiomyocyte purity was achieved (Figure 40).

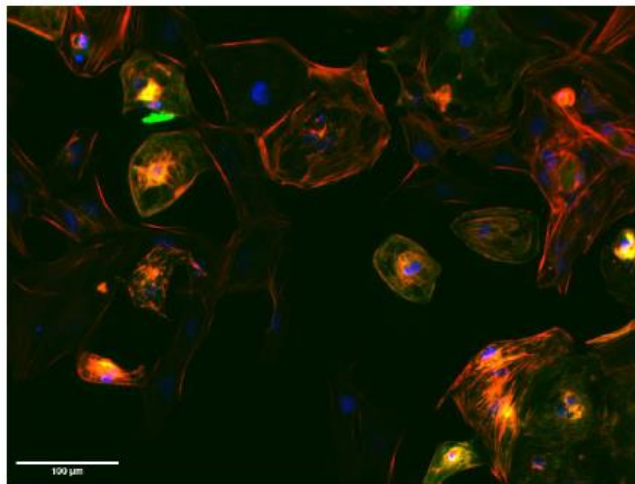


Figure 40 – Cardiomyocytes from the first differentiation batch. Immunostaining of these cells was performed using Hoechst 33258 – blue, Alexa Fluor-phalloidin - red and anti-TNNI3 – green). Photo taken with Leica microscope, at x10 magnification; scale bar 100 µm

Once we have confirmed the success of the differentiation protocol, hiPSC-CMs were seeded on the different materials as we have previously done with the fibroblasts. In this case, the main difference between both cell types is that cardiac cells are non-proliferative cells and growth curves cannot be elaborated. For this reason, an immunostaining assay was carried out to determine the expression of cardiac-specific proteins. Immunostaining of these cells was performed using different fluorescence markers to identify the intracellular structures: cell nuclei (blue, Hoechst 33258), cytoskeleton actin fibres (red, Alexa Fluor-phalloidin) and cardiac sarcomeres (green, anti-TNNI3 specific antibody).

In Figure 41 we can see the results of the immunostaining. It can be concluded that, due to the high purity of the differentiation of hiPSCs into cardiomyocytes, the majority of the cells are cardiomyocytes. The main conclusion that can be drawn from this assay is that cell density is higher on the positive control condition and decreases in the hydrogels, especially with the addition of PEDOT:PSS – decreasing amount of nucleus - as previously seen with fibroblasts

cell seeding. This might be happening due to a lower cell adhesion of the cells on the hydrogels, specially those with PEDOT:PSS. Also, the higher the PEDOT:PSS content, the more aggregates it forms and, similarly to what was observed for fibroblasts, the less space it has for cardiomyocytes to adhere, as it looks like cells don't seed directly on top of a PEDOT:PSS aggregate. Compared to cardiomyocytes seeded in the control condition (Figure 41A), these cardiomyocytes present a rounder morphology, and a significantly lower size.

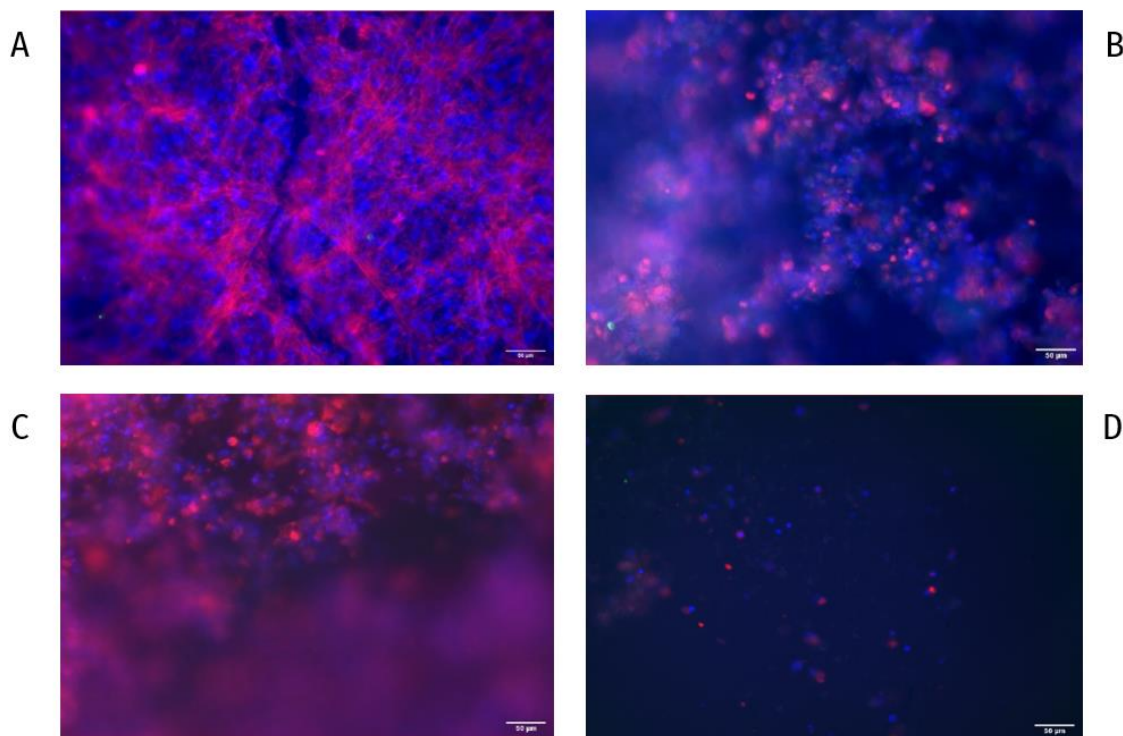


Figure 41 - Cardiomyocyte immunostaining results, on two different regions of the well plate; A: positive control; B: sisECM; C: sisECM + 0.05% PEDOT:PSS; D: sisECM + 0.1% PEDOT:PSS; scale bar 50  $\mu\text{m}$

### 3.5. Cell bioprinting

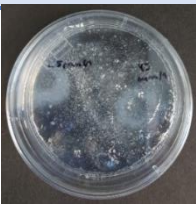
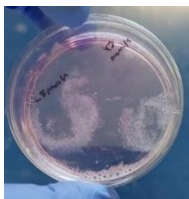



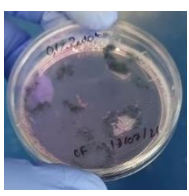
Once it was determined that cells could grow on the different materials, we proceeded with the bioprinting experiments. For this, the cells were added to the previously prepared bioinks.

#### 3.5.1 Mouse Fibroblasts

Firstly, 2 mL of each bioink was prepared following the previously described protocol (see section 2.1. of chapter 2), to which 200  $\mu\text{L}$  of cell suspension media was added at a concentration of  $0.5 \times 10^6$  cells/mL. In accordance to the optimal printing conditions determined in section 3.1.2, structures of circular geometry ( $r=2.5$  mm) were printed. Bioink composition and printing parameters are described in Table 15.

On day 0, pictures of the printed structures were taken before and after gelatin removal. Their structural maintenance was not achieved mainly due to the decreased concentration of sisECM on the final hydrogel as it lowered with the addition of the cell's suspension.

Table 15 - Bioink formulation for fibroblasts bioprinting

| $C_{\text{PEDOT:PSS}}$<br>(%) | $C_{\text{sisECM}}$<br>(mg/mL) | Printing Parameters   | Before gelatin removal   | After gelatin removal   |
|-------------------------------|--------------------------------|---|--|---|
| 0                             | 7.3                            | Printing speed: 45 mm/s<br>Dispensing pressure: 0.1 psi<br>Number of layers:3<br>Distance between layers: 0.05 mm |  |  |
| 0.05                          | 6.9                            | Printing speed: 45 mm/s<br>Dispensing pressure: 0.1 psi<br>Number of layers:3<br>Distance between layers: 0.05 mm |  |  |
| 0.1                           | 6.6                            | Printing speed: 45 mm/s<br>Dispensing pressure: 0.1 psi<br>Number of layers:3<br>Distance between layers: 0.05 mm |  |  |

Also, it was not possible to control the temperature as accurately as before since once of the materials were sterilized it was not possible to keep needles and tubes at 4°C. This triggered certain gelation before the materials were extruded, causing some clogging in the needle tip and limiting the printability of the materials.

After gelatin removal, the printed structures were left in the incubator at 37°C with DMEM-media, replaced every 2 days. Pictures with a x10 magnification were taken with the Leica microscope, Figure 42. Until day 3, for PEDOT:PSS hydrogels conditions, cells exhibited a small and round morphology, whereas for the sisECM hydrogels, from day 1 onwards, cells presented a spindle shape morphology. From day 5 onwards, cells in sisECM+0.05% PEDOT:PSS exhibited also presented a spindle shape morphology, and cells cultured on sisECM + 0.1%PEDOT:PSS hydrogels still presented a round morphology (in accordance with cell seeding results). This means that cell adherence might take longer to occur on printed hydrogels.

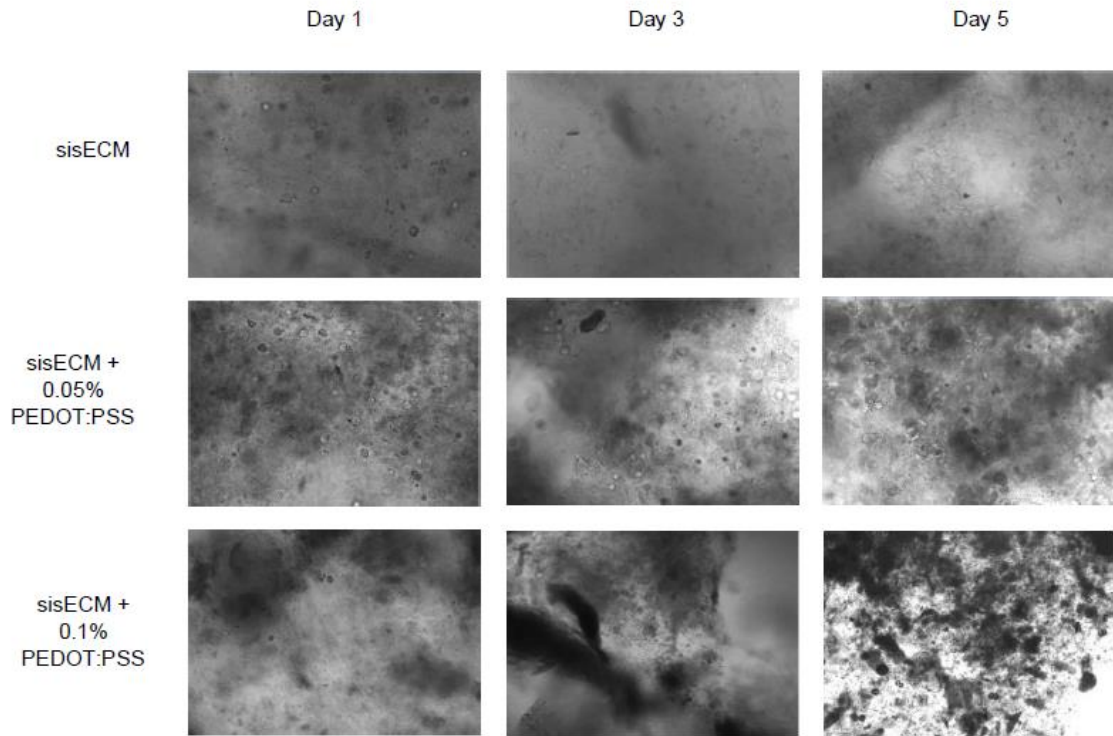


Figure 12 - Pictures taken with Leica microscope (10x magnification) of fibroblasts containing printed structures of the 3 different hydrogels. Days 1, 3 and 5 of cell culture.

Finally, a viability assay was performed as shown in previous sections . The results are presented in Figure 43.

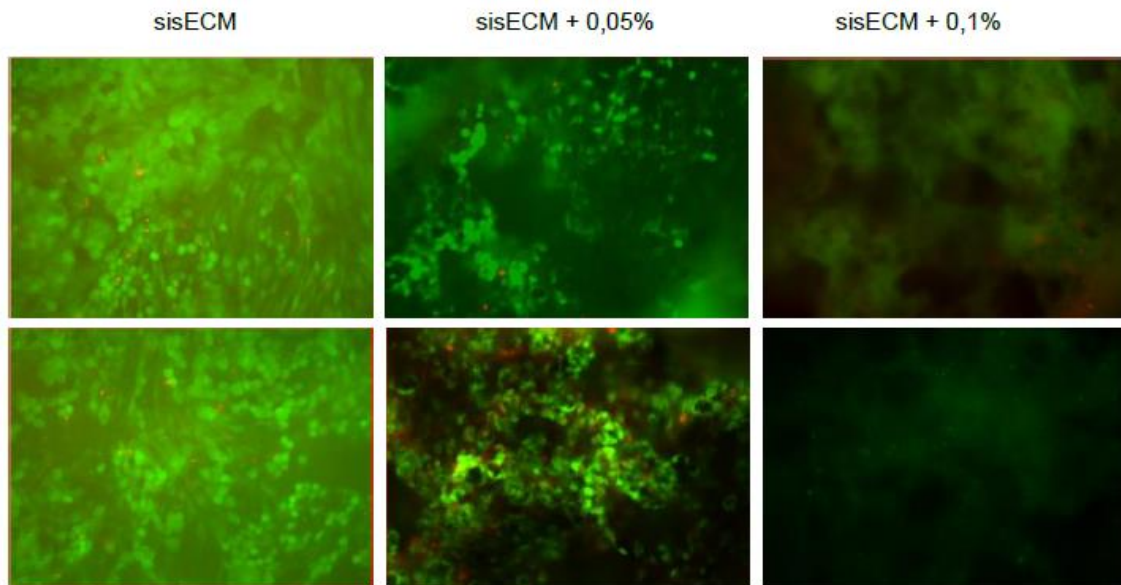


Figure 43 - Pictures taken with Leica fluorescence microscope (20x magnification) of fibroblasts printed with sisECM, sisECM + 0.05% PEDOT:PSS and sisECM+0.1% PEDOT:PSS hydrogels on day 7 of cell culture. Green cells (alive) are stained with calcein-AM red cells (dead) with ethidium homodimer-1

As expected, cell viability is higher in the cell seeding assay, Figures 44 and 45, although cell viability for printed structures is > 95%. For sisECM, sisECM + 0.05% PEDOT:PSS and sisECM + 0.1% PEDOT:PSS cell viabilities are  $95.21 \pm 1.0\%$ ,  $95.09 \pm 1.3\%$  and  $99.57 \pm 0.6\%$ , respectively (Figure 27). This difference can be explained by the exposure of the cells to the printing process. It is important to note that cells undergo mixing with the bioink, that even though was a gentle mixing, it was not possible to guarantee integrity of all cells. Also, the bioinks were kept at 4°C, meaning that cells were exposed to thermic shock. However, as explained in the beginning of this section, materials were not kept at 4°C, which led to early gelation of the bioinks and higher extruding pressures. This might have also impacted cell integrity during the printing process.

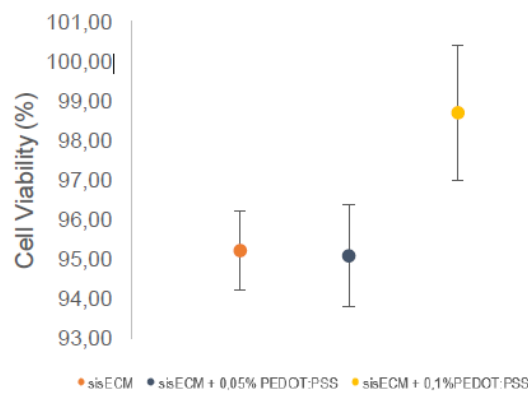


Figure 44 - Viability results for cell bioprinting of fibroblasts for all 3 hydrogels; n=4.

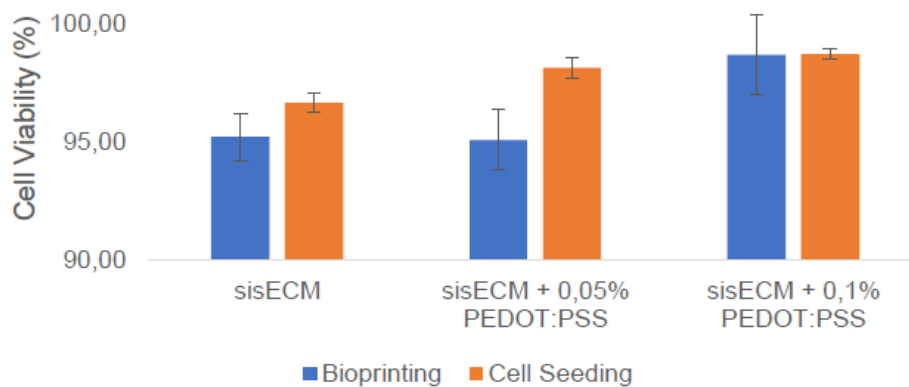


Figure 45 - Viability results for bioprinting and cell seeding of fibroblasts; n=4

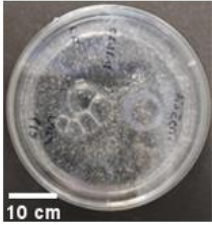
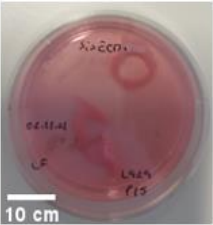
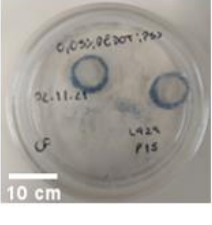
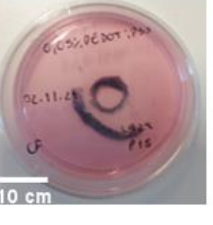
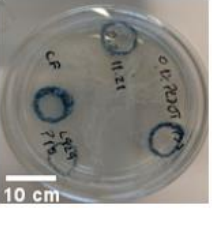
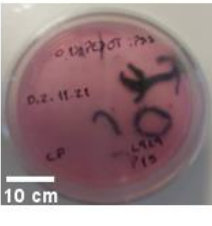
To solve the problem of structural integrity not being maintained after gelatin removal, an adjustment in sisECM concentration was performed, where sisECM was kept at 8.0 mg/mL in the final bioink preparation after addition of 200 µL of cell suspension at a concentration of



0.5x10<sup>6</sup> cells/mL. Also, the number of layers of the printed structure was increased from 3 to 5. Bioink composition and printing parameters are described in Table 16.

On day 0, pictures of the printed structures were taken before and after gelatin removal. Their structural maintenance was achieved, with exception of some constructs of sisECM + PEDOT:PSS conditions due to inconsistencies in the printing process, related to clogging of the needle due to the formation of PEDOT:PSS aggregates, causing some of some of the layers to not be properly printed. The structural integrity was also maintained after 7 days of cell culture at 37°C, with media changes every two days.

Table 16 - Bioink formulation for fibroblasts bioprinting after sisECM concentration adjustments.

| C <sub>PEDOT:PSS</sub> (%) | C <sub>sisECM</sub> (mg/mL) | Printing Parameters   | Before gelatin removal   | After gelatin removal   |
|----------------------------|-----------------------------|---|--|---|
| 0                          | 8.0                         | Printing speed: 45 mm/s<br>Dispensing pressure: 0.1 psi<br>Number of layers:5<br>Distance between layers: 0.05 mm |   |   |
| 0.05                       | 8.0                         | Printing speed: 45 mm/s<br>Dispensing pressure: 0.1 psi<br>Number of layers:5<br>Distance between layers: 0.05 mm |  |  |
| 0.1                        | 8.0                         | Printing speed: 45 mm/s<br>Dispensing pressure: 0.1 psi<br>Number of layers:5<br>Distance between layers: 0.05 mm |  |  |

Regarding cell morphology, the behaviour verified for the previous bioprinting experiments was observed, with until day 3, for PEDOT:PSS hydrogels conditions, cells exhibiting a small and round morphology, whereas for the sisECM hydrogels, from day 1 onwards, cells presented a spindle shape morphology. From day 5 onwards, cells in sisECM+0.05% PEDOT:PSS exhibited also presented a spindle shape morphology, and cells cultured on sisECM + 0.1%PEDOT:PSS hydrogels still presented a round morphology (in accordance with cell seeding results).

However, it was also observed that despite lower cell adhesion to the PEDOT:PSS hydrogels, cells started to form cell aggregates, promoting cell proliferation, Figure 46.

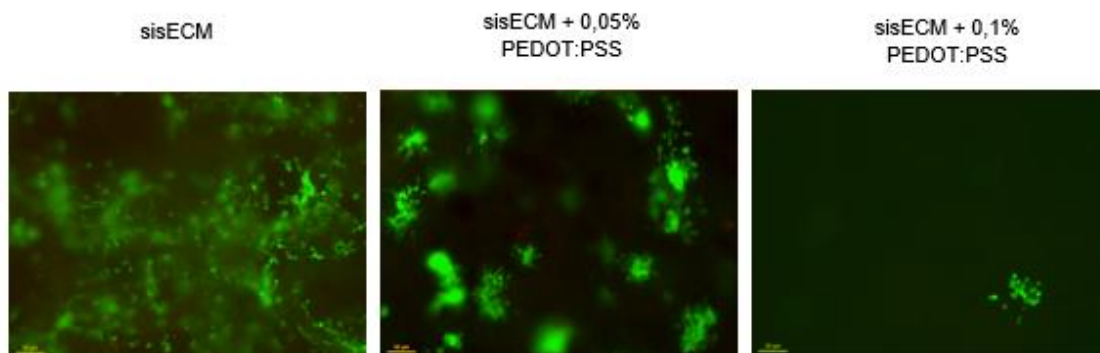


Figure 46 - Pictures taken with Leica fluorescence microscope (20x magnification) of fibroblasts printed with sisECM, sisECM + 0.05% PEDOT:PSS and sisECM+0.1% PEDOT:PSS hydrogels on day 7 of cell culture. Green cells (alive) are stained with calcein-AM red cells (dead) with ethidium homodimer-1; scale bar 50  $\mu$ m.

### 3.6. Alternative bioinks explored

#### 3.6.1 Alginate and Gelatin bioink




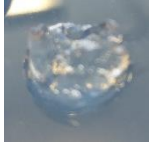
##### 3.6.1.1 Bioink formulation and hydrogel testing

An alginate + gelatin (alg-gel) hydrogel was prepared to evaluate and compare to the conductive properties and biocompatibility of the sisECM bioinks. The formulation of this ink was based on previous works<sup>168</sup> and consisted on alg-gel solution with 1:1 proportion of 7.5% alginate and 15% gelatin was prepared, resulting in an 3.75%-7.5% alg-gel bioink.

Due to the extremely high viscosity of the 7.5% alginate solution, which made it very difficult to extrude and manipulate, the alginate concentration was reduced to 5%. The final formulation of the alg-gel bioink was 2.5%/7.5%. Proportions of 2:1 and 1:2 of 5% alginate and 7.5% gelatin were also tested. These formulations were then casted in the molds previously used for sisECM experiments. On top of the mold, 0.16%  $\text{CaCl}_2$  was added to allow for alginate crosslinking, and the structures were left to gelate at room temperature for 20 minutes. After this, the casts were removed.

The same parameters used to select the sisECM hydrogels were applied, with exception to the PEDOT:PSS dispersion (Table 17). Due to high scores in all parameters for the 2.5%-7.5% alg-gel hydrogel, bioprinting assays were performed.

Table 17 - Different alginate and gelatin concentrations and proportions in final hydrogel tested; parameters classification scale: 1 – discarded result; 2 – acceptable; 3 – perfect result.

| Proportion | Alginate (%) | Gelatin (%) | Circularity | Gelification outcome | Photo   |
|------------|--------------|-------------|-------------|----------------------|---|
| 1:1        | 3.75         | 7.5         | 3           | 3                    |    |
| 1:1        | 2.5          | 7.5         | 3           | 3                    |    |
| 2:1        | 3.3          | 5           | 2           | 1                    |    |
| 1:2        | 1.7          | 10          | 2           | 2                    |  |

### 3.6.1.2 Alg-gel printing

Firstly, some simple structures were printed to understand the printability conditions of the 2.5%-7.5% alg-gel bioink. It is important to note that this bioink, due to its high viscosity, does not need a supporting bath, and so FRESH was not used in the printing process. Also, for crosslinking, 0.16% CaCl<sub>2</sub> was added on top of each structure after printing, and then stored with 0.04% CaCl<sub>2</sub> in PBS. This is necessary because alginate is a polysaccharide composed of repeating units of 4 β-D-mannuronic acid (M) and α-L-guluronic acid (G) and forms a hydrogel by ionic-crosslinking of the G monomers in the presence of a divalent cation. Without this solution, alginate structures will collapse (section 1.4.1., Chapter 1).





The printability process for smaller geometries, with a lower number of layers (until 10 layers) was successfully achieved with this bioinks, with the printed structures exhibiting self-support and not collapsing. However, structures with more than 10 layers or larger geometries were not possible to print due to limitations in the control of temperature in the printer head, since these inks required to be maintained at 37°C, which is not possible in our instrument. Before printing, bioink solutions were kept at 37°C which significantly lower their viscosity, however, the printing process was performed at room temperature. Consequently, the temperature of the alg-gel



lowered, causing the bioink to start to harden inside the cartridge, making the printing process more difficult and resulting in incomplete printed structures.

The printing parameters and results are presented in Table 18. For all structures, the needle diameter was 0.6 mm. In the case of a printing speed of 2 mm/s and distance between layers of 0.05 mm, too much bioink was dispensed, and resolution was poor. To correct this, printing speed was increased to 5 mm/s, distance between layer set to 0.08 mm and extruding pressure lowered from 20 psi to 15 psi, with greater success for structures with 5 and 10 layers. However, for a 20 layered structure, the printing process was not complete due to the hardening of the bioink inside the plastic cartridge.

Table 18 - Printing parameters for the 2.5%-7.5% alg-gel bioink and respective results.

| Parameters   | Photos   |
|--|--|
| Number of Layers: 5<br>Geometry: square; L= 5 mm<br>Pressure: 20 psi<br>Printing Speed: 2 mm/s<br>Distance between layers: 0.05 mm   |    |
| Number of Layers: 5<br>Geometry: square; L= 5 mm<br>Pressure: 15 psi<br>Printing Speed: 5 mm/s<br>Distance between layers: 0.08 mm   |   |
| Number of Layers: 10<br>Geometry: square; L= 10 mm<br>Pressure: 15 psi<br>Printing Speed: 5 mm/s<br>Distance between layers: 0.08 mm |  |
| Number of Layers: 20<br>Geometry: square; L= 10 mm<br>Pressure: 15 psi<br>Printing Speed: 5 mm/s<br>Distance between layers: 0.08 mm |  |

Once the preliminary printing parameters were optimized, PEDOT:PSS was incorporated so that we had bioinks with the same concentrations as those with sisECM (0.05% and 0.1% PEDOT:PSS in final formulations). We could observe that contrary to the sisECM hydrogel, the addition of PEDOT:PSS lowered the viscosity of the 2.5%-7.5% alg-gel bioink, as opposed to what was observed for sisECM bioinks. The lowered viscosity of these alg-gel PEDOT:PSS bioinks could be due to an increase in the water content of the materials, reducing the limiting effect of temperature decrease and facilitating the printing process. The higher the PEDOT:PSS concentration, the lower the viscosity. Results and printing parameters are described in Table 19. The pore factor, as well as wall thickness and pore size were also calculated.

Table 19 - Printing parameters for the 2.5%-7.5% alg-gel, 2.5%-7.5% alg-gel+0.05% PEDOT:PSS and 2.5%-7.5% alg-gel+0.1% PEDOT:PSS bioinks and respective results.

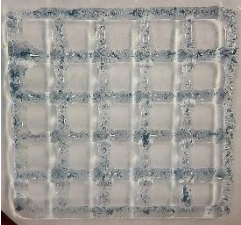
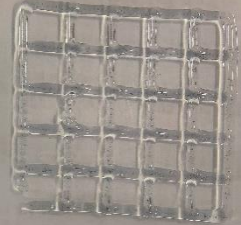

| Conditions                          | Parameters   | Results  |
|-------------------------------------|--|--|
| 2.5%/7.5% alg-gel                   | Number of Layers: 1<br>Geometry: square mesh; L= 20 mm<br>Pressure: 15 psi<br>Printing Speed: 5 mm/s |   |
| 2.5%/7.5% alg-gel + 0.05% PEDOT:PSS | Number of Layers: 1<br>Geometry: square mesh; L= 20 mm<br>Pressure: 10 psi<br>Printing Speed: 5 mm/s |   |
| 2.5%/7.5% alg-gel + 0.1% PEDOT:PSS  | Number of Layers: 1<br>Geometry: square mesh; L= 20 mm<br>Pressure: 7 psi<br>Printing Speed: 5 mm/s  |  |

Table 20 - Results for wall thickness, pore diameter and pore factor for each bioink, as well as their respective deviations to the intended dimensions.

| Bioink              | alg-gel + 0.1% PEDOT:PSS | alg-gel + 0.05% PEDOT:PSS | Alg-gel     |
|---------------------|--------------------------|---------------------------|-------------|
| Wall Thickness (mm) | 2.63 ± 0.79              | 2.46 ± 0.52               | 2.34 ± 0.39 |
| Pore Diameter (mm)  | 5.24 ± 0.87              | 5.77 ± 0.65               | 6.03 ± 0.27 |
| WT (%)              | 338.33                   | 310.0                     | 289.83      |
| PD (%)              | 67.25                    | 63.94                     | 62.3        |
| Pore Factor (Pr)    | 1.07±0.03                | 1.04±0.05                 | 1.01±0.07   |

The results presented in Table 20 show that the higher the PEDOT:PSS concentration, the higher the wall thickness is and the smaller the pore diameter is. These results are in accordance with what was expected, because the higher the PEDOT:PSS concentration, the

lower the viscosity and the more the bioink disperses on the plate, so there is more variation to the intended dimensions, with wall thickness of 0.6 mm and pore diameter of 16 mm. This is in accordance to results for pore factor, where the higher the PEDOT:PSS concentration, the further away the value is to 1 ( $Pr = 1$  is the intended result).

After successful bioprinting tests, other assays were performed to evaluate if the bioink was suitable for cell culture. For this, structures for a 30-day stability assay were prepared and stored in 0.04%  $\text{CaCl}_2$  in PBS. However, at day 3 the structures had started to collapse and by day 5 they had completely collapsed, making this bioink not suitable for long term cell culture, as observed in Figure 47. Therefore, this bioink was discarded in subsequent experiments.

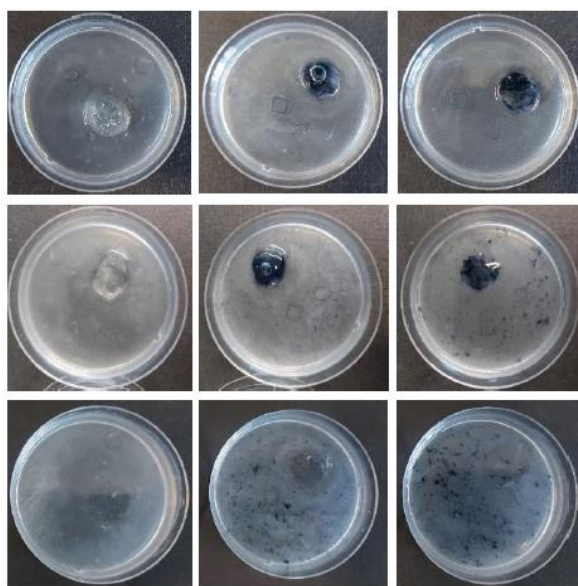


Figure 47 - Stability assay for 2.5%-7.5% alg-gel, 2.5%-7.5% alg-gel+0.05% PEDOT:PSS and 2.5%-7.5% alg-gel+0.1% PEDOT:PSS (left to right, respectively) ; day 0 (top), day 3 (middle) and day 5 (bottom).

### 3.6.2 Magnetic particles and sisECM bioink

Besides electrical stimulation, magnetic stimulation has also been reported to improve cardiomyocyte maturation. For this reason and following the formulation of the electroconductive bioink, an ECM bioink suitable for magnetic stimulation was designed. The magnetic properties were introduced by the addition of non-functionalized iron oxide ( $\text{Fe}_3\text{O}_4$ ) nanoparticles. These nanoparticles have been shown, in combination with hydrogels, to be able to respond to a variation in magnetic field on a fast mode, with reversible changes of their shape and volume. This permits contraction and distention of the hydrogels when a non-uniform magnetic field is applied, making these hydrogels suitable to be applied as mechanical actuators, used for the design of membranes with adjustable pore sizes, as activators of molecular motors to mimic nature systems, and to modulate cell responses at magnetic responsive hydrogel scaffolds<sup>169</sup>. Transmission electron microscopy (TEM) and dynamic light scattering (DLS) assays were performed on these particles, and results are presented in Figures 48 and 49. As observed in Figure 30, the nanoparticles are small and rounded, with

heterogenous size distribution (also confirmed by DLS results) and clustered together (a characteristic of the non-functionalized particles).

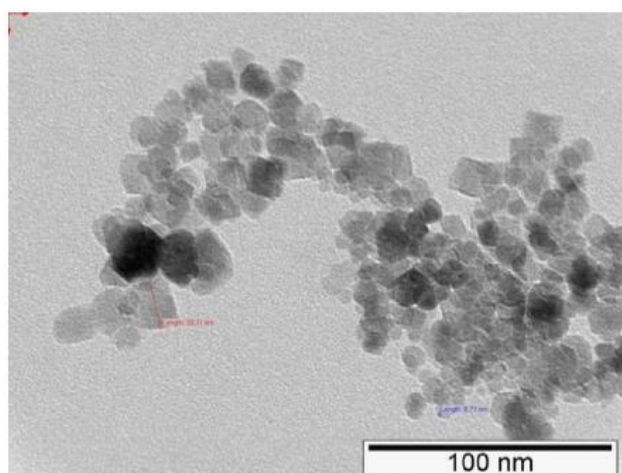


Figure 48 - Transmission electron microscopy for non-functionalized iron oxide ( $\text{Fe}_3\text{O}_4$ ) nanoparticles.

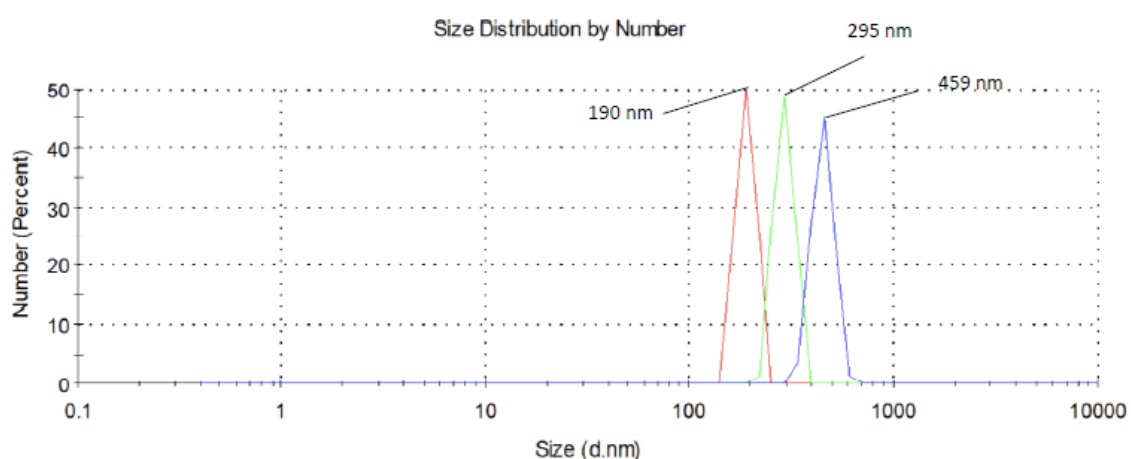


Figure 49 - Dynamic light scattering for non-functionalized iron oxide ( $\text{Fe}_3\text{O}_4$ ) nanoparticles

In the process of designing the bioinks, several  $\text{Fe}_3\text{O}_4$  nanoparticles concentrations were tested, based on the already used concentrations for the previously formulated PEDOT:PSS hydrogels. For the magnetic particles' hydrogels, sisECM concentration was maintained at 8 mg/mL, and the  $\text{Fe}_3\text{O}_4$  particles diluted in neutralization buffer. After preparation, the bioinks were casted in the previously used molds and incubated at 37°C, with varying incubation times depending on the particle's concentration. Finally, after the mold's removal, all hydrogel structures were evaluated on circularity, magnetic particles dispersion and gelification outcome (using the same evaluation parameters that were previously used to characterize sisECM + PEDOT:PSS hydrogels). On Table 21, all the formulations and the results of the evaluation of all  $\text{Fe}_3\text{O}_4$  nanoparticles concentrations used to produce hydrogels is presented, for incubation at 37 °C for all conditions.

Due to top scores in all parameters for the sisECM + 0.2%  $\text{Fe}_3\text{O}_4$  nanoparticles, this bioink was chosen for further testing. A contact angle assay was performed, with results presented in

Figure 50. This assay allows understanding and characterizing of the wettability of the surface by measuring the contact angle between a liquid drop and a solid surface, giving information about the hydrophobicity/hydrophilicity of the surface, surface heterogeneity, roughness, solid surface energy and liquid surface tension. A drop of liquid is deposited on a smooth solid surface and the angle between the solid surface and the tangent to the drop profile at the drop edge is measured. The results for sisECM + 0.2% Fe<sub>3</sub>O<sub>4</sub> are of 24.15±2.47° and 12.13±2.20° for 0T and 0.08T, respectively. This indicates that in the presence of a magnetic field, the contact angle lowers, making the material more wetting (the closer to 0° the more spreading of the liquid; the closer to 180°, the more non-wetting the material is). However, due to time constraints, no more tests were performed.

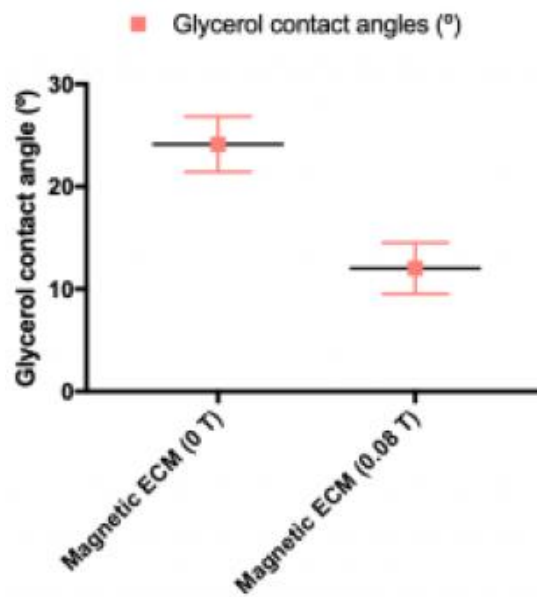




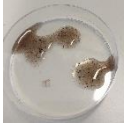


Figure 13 – Impact of the magnetic field on the glycerol contact angle for sisECM + 0.2% Fe<sub>3</sub>O<sub>4</sub> nanoparticles bioink.

Table 21 - Different iron oxide magnetic nanoparticles concentrations in final sisECM hydrogel tested; parameters classification scale: 1 – discarded result; 2 – acceptable; 3 – perfect result.

| Condition | sisECM concentration (mg/mL) | Fe <sub>3</sub> O <sub>4</sub> nanoparticles concentration (%) | Incubation time (h) | Circularity | Fe <sub>3</sub> O <sub>4</sub> nanoparticles dispersion | Gelification outcome | Photo   |
|-----------|------------------------------|--|---------------------|-------------|---|----------------------|---|
| A         | 8.0                          | 0.01   | 2                   | 2           | 3   | 2                    |    |
| B         | 8.0                          | 0.05   | 2                   | 2           | 3   | 2                    |    |
| C         | 8.0                          | 0.1  | 1                   | 2           | 3   | 2                    |    |
| D         | 8.0                          | 0.2  | 1                   | 3           | 3   | 3                    |  |
| E         | 8.0                          | 1.0  | 2                   | 1           | 1   | 1                    |  |

## Chapter 4 - Conclusions and Future Remarks

The main goal of this work was to develop a novel ECM-based conductive bioink for extrusion based bioprinting of biocompatible scaffolds for potential application in cardiac tissue engineering.

Regarding the formulation of the bioink, great success was achieved in PEDOT:PSS addition to a decellularized sisECM solution – though this formulation is limited by the sisECM concentration, that was verified to have to be over 7 mg/mL for complete hydrogel gelation. Also, PEDOT:PSS concentration could not be in excess of 0.1% in final bioink formulation to avoid the formation of polymer aggregates that impeded complete hydrogel gelation.

Hydrogel properties were evaluated, with focus on electrochemical characterization, and allowed the establishment of PEDOT:PSS hydrogels as viable electroconductive polymer-based scaffolds, with conductivity values in accordance to those found in literature. Also, for all sisECM hydrogels, the biomaterial behaved as a capacitor at low frequencies and a resistor at high frequencies (>10000 Hz) regardless of PEDOT:PSS concentration. The capacitive behavior is attractive for potential application as energy storage devices. Also, the hydrogel showed stability in PBS solution for over 30 days, with great potential for long-term cell culture.

With the aim of using these bioinks for 3D bioprinting, a rheological characterization was performed, and the bioinks were considered to be suitable for extrusion bioprinting, making use of the FRESH technique. Printability of the scaffolds was evaluated, with satisfactory resolution, but mechanical stability and shape-fidelity were hindered by the limitation of temperature control, due to early polymerization of the sisECM with the addition of PEDOT:PSS.

Furthermore, proof-of-concept cell-based experiments allowed the verification of the bioink compatibility with both mouse fibroblasts and hiPSC-CMs. However, despite great results for cell viability in both cell seeding assays and cell bioprinting, the 3D nature of the hydrogels was incompatible with the microscope used. In future experiments, the use of a confocal microscope is advised. Also, viability was verified just with immunoassays. In future work, DNA content analysis and imaging of cardiac cell markers could be employed. Regarding cell bioprinting, sisECM concentration adjustment needs to be done to improve bioprinted constructs mechanical stability. Also, the bioprinting of cardiomyocytes and electrical stimulation on these sisECM - PEDOT:PSS bioprinted scaffolds is to be done, to evaluate if cardiomyocyte maturation is improved.

Finally, sisECM-based bioinks have the potential to be altered for magnetic stimulation, with iron oxide magnetic particles, as demonstrated in this work, though further testing to investigate its biocompatibility and impact of magnetic-field exposure on cardiomyocyte maturation needs to be done. With this in mind, sisECM-based bioinks also have the potential to be formulated with piezoelectric nanoparticles for application in cardiac tissue engineering.

## References

1. Caddeo, S., Boffito, M. & Sartori, S. Tissue Engineering Approaches in the Design of Healthy and Pathological In Vitro Tissue Models. *Front. Bioeng. Biotechnol.* **0**, 40 (2017).
2. S, D. *et al.* 3D bioprinting for biomedical devices and tissue engineering: A review of recent trends and advances. *Bioact. Mater.* **3**, 144–156 (2018).
3. Askari, M. *et al.* Recent progress in extrusion 3D bioprinting of hydrogel biomaterials for tissue regeneration: a comprehensive review with focus on advanced fabrication techniques. *Biomater. Sci.* **9**, 535–573 (2021).
4. Correia, C. *et al.* 3D aggregate culture improves metabolic maturation of human pluripotent stem cell derived cardiomyocytes. *Biotechnol. Bioeng.* **115**, 630–644 (2018).
5. Mason, C. & Dunnill, P. A brief definition of regenerative medicine. <http://dx.doi.org/10.2217/17460751.3.1.1> **3**, 1–5 (2007).
6. Mao, A. S., Mooney, D. J. & Paulson, J. A. Regenerative medicine: Current therapies and future directions. doi:10.1073/pnas.1508520112.
7. What is the future of 3D printed organs? (2021 Update). <https://www.sculpteo.com/blog/2019/10/16/the-most-promising-3d-printed-organs-projects/>.
8. 3D Printing Organs Pros & Cons - 2021 | Future Implications of Bioprinting. <https://ultradvice.com/3d-printing-organs-pros-cons/>.
9. Parak, A. *et al.* Functionalizing bioinks for 3D bioprinting applications. *Drug Discov. Today* **24**, 198–205 (2019).
10. Zhang, B. *et al.* 3D bioprinting: an emerging technology full of opportunities and challenges. *Bio-Design Manuf.* **2018 11 1**, 2–13 (2018).
11. Mirdamadi, E., Tashman, J. W., Shiwarski, D. J., Palchesko, R. N. & Feinberg, A. W. FRESH 3D Bioprinting a Full-Size Model of the Human Heart. *ACS Biomater. Sci. Eng.* **6**, 6453–6459 (2020).
12. B, D., LA, H., KH, K. & JT, B. 3D bioprinting of heterogeneous aortic valve conduits with alginate/gelatin hydrogels. *J. Biomed. Mater. Res. A* **101**, 1255–1264 (2013).
13. Cui, X., Breitenkamp, K., Finn, M. G., Lotz, M. & D'Lima, D. D. Direct Human Cartilage Repair Using Three-Dimensional Bioprinting Technology. *Tissue Eng. Part A* **18**, 1304 (2012).
14. More efficient drug screening with 3D bioprinting - CELLINK. <https://www.cellink.com/blog/more-efficient-drug-screening-with-3d-bioprinting/>.
15. Hagenbuchner, J., Nothdurfter, D. & Ausserlechner, M. J. 3D bioprinting: novel approaches for engineering complex human tissue equivalents and drug testing. *Essays Biochem.* **65**, 417–427 (2021).
16. Zhang, Y. S. *et al.* Bioprinting 3D microfibrillar scaffolds for engineering endothelialized myocardium and heart-on-a-chip. *Biomaterials* **110**, 45 (2016).
17. Nguyen, D. G. *et al.* Bioprinted 3D Primary Liver Tissues Allow Assessment of Organ-Level Response to Clinical Drug Induced Toxicity In Vitro. *PLoS One* **11**, e0158674 (2016).
18. HG, Y. *et al.* A bioprinted human-glioblastoma-on-a-chip for the identification of patient-specific responses to chemoradiotherapy. *Nat. Biomed. Eng.* **3**, 509–519 (2019).
19. Ma, X. *et al.* 3D bioprinting of functional tissue models for personalized drug screening and in vitro disease modeling. *Adv. Drug Deliv. Rev.* **132**, 235–251 (2018).
20. A, F.-J. *et al.* Bioprinting of human pluripotent stem cells and their directed differentiation into



- hepatocyte-like cells for the generation of mini-livers in 3D. *Biofabrication* **7**, (2015).
21. Q, G., E, T.-C., GG, W. & JM, C. 3D Bioprinting Human Induced Pluripotent Stem Cell Constructs for In Situ Cell Proliferation and Successive Multilineage Differentiation. *Adv. Healthc. Mater.* **6**, (2017).
  22. Nguyen, D. *et al.* Cartilage Tissue Engineering by the 3D Bioprinting of iPS Cells in a Nanocellulose/Alginate Bioink. *Sci. Reports 2017 71* **7**, 1–10 (2017).
  23. C, Y. *et al.* Scanningless and continuous 3D bioprinting of human tissues with decellularized extracellular matrix. *Biomaterials* **194**, 1–13 (2019).
  24. Desimone, E., Schacht, K., Jungst, T., Groll, J. & Scheibel, T. Biofabrication of 3D constructs: Fabrication technologies and spider silk proteins as bioinks. *Pure Appl. Chem.* **87**, 737–749 (2015).
  25. Mironov, V., Reis, D. N. & Derby, B. Review: Bioprinting: A Beginning. <https://home.liebertpub.com/ten> **12**, 631–634 (2006).
  26. Mobaraki, M., Ghaffari, M., Yazdanpanah, A., Luo, Y. & Mills, D. K. Bioinks and bioprinting: A focused review. *Bioprinting* **18**, e00080 (2020).
  27. Wang, Z. *et al.* A simple and high-resolution stereolithography-based 3D bioprinting system using visible light crosslinkable bioinks. *Biofabrication* **7**, 045009 (2015).
  28. Guillotin, B. *et al.* Laser-Assisted Bioprinting for Tissue Engineering. *Biofabrication Micro- Nano-fabrication, Printing, Patterning Assem.* 95–118 (2013) doi:10.1016/B978-1-4557-2852-7.00006-8.
  29. Dababneh, A. B. & Ozbolat, I. T. Bioprinting Technology: A Current State-of-the-Art Review. *J. Manuf. Sci. Eng.* **136**, (2014).
  30. Hölzl, K. *et al.* Bioink properties before, during and after 3D bioprinting. *Biofabrication* **8**, 032002 (2016).
  31. Murphy, S. V & Atala, A. 3D bioprinting of tissues and organs. *Nat. Biotechnol. 2014 328* **32**, 773–785 (2014).
  32. Jia, J. *et al.* Engineering alginate as bioink for bioprinting. *Acta Biomater.* **10**, 4323 (2014).
  33. Phillippi, J. A. *et al.* Microenvironments Engineered by Inkjet Bioprinting Spatially Direct Adult Stem Cells Toward Muscle- and Bone-Like Subpopulations. *Stem Cells* **26**, 127–134 (2008).
  34. FY, H., HH, L. & SH, H. 3D bioprinting of neural stem cell-laden thermoresponsive biodegradable polyurethane hydrogel and potential in central nervous system repair. *Biomaterials* **71**, 48–57 (2015).
  35. Raman, R. & Bashir, R. Stereolithographic 3D Bioprinting for Biomedical Applications. *Essentials 3D Biofabrication Transl.* 89–121 (2015) doi:10.1016/B978-0-12-800972-7.00006-2.
  36. JY, P. *et al.* A comparative study on collagen type I and hyaluronic acid dependent cell behavior for osteochondral tissue bioprinting. *Biofabrication* **6**, (2014).
  37. R, G. *et al.* Patterning human stem cells and endothelial cells with laser printing for cardiac regeneration. *Biomaterials* **32**, 9218–9230 (2011).
  38. Catros, S., Guillotin, B., Bačáková, M., Fricain, J. C. & Guillemot, F. Effect of laser energy, substrate film thickness and bioink viscosity on viability of endothelial cells printed by laser-assisted bioprinting. *Appl. Surf. Sci.* **257**, 5142–5147 (2011).
  39. Zhu, K. *et al.* A General Strategy for Extrusion Bioprinting of Bio-Macromolecular Bioinks through Alginate-Templated Dual-Stage Crosslinking. *Macromol. Biosci.* **18**, e1800127 (2018).
  40. Gao, T. *et al.* Optimization of gelatin–alginate composite bioink printability using rheological parameters: a systematic approach. *Biofabrication* **10**, 034106 (2018).

41. Hinton, T. J. *et al.* Three-dimensional printing of complex biological structures by freeform reversible embedding of suspended hydrogels. *Sci. Adv.* **1**, (2015).
42. MirdamadiEman, MuselimyanNarine, KotiPriyanka, AsfourHuda & SarvazyanNarine. Agarose Slurry as a Support Medium for Bioprinting and Culturing Freestanding Cell-Laden Hydrogel Constructs. <https://home.liebertpub.com/3dp> **6**, 158–164 (2019).
43. Hinton, T. J. *et al.* Three-dimensional printing of complex biological structures by freeform reversible embedding of suspended hydrogels. *Sci. Adv.* **1**, (2015).
44. Noor, N. *et al.* 3D Printing of Personalized Thick and Perfusable Cardiac Patches and Hearts. *Adv. Sci.* **6**, 1900344 (2019).
45. YJ, C. *et al.* A 3D cell printed muscle construct with tissue-derived bioink for the treatment of volumetric muscle loss. *Biomaterials* **206**, 160–169 (2019).
46. Baird, D. G. Polymer Processing. *Encycl. Phys. Sci. Technol.* 611–643 (2003) doi:10.1016/B0-12-227410-5/00593-7.
47. Basics of rheology :: Anton Paar Wiki. <https://wiki.anton-paar.com/en/basics-of-rheology/>.
48. WHITEPAPER 2 A Basic Introduction to Rheology Shear Flow.
49. Ramesh, S. *et al.* Extrusion bioprinting: Recent progress, challenges, and future opportunities. *Bioprinting* **21**, e00116 (2021).
50. Kaklamani, G. *et al.* On the electrical conductivity of alginate hydrogels. *Regen. Biomater.* **5**, 293–301 (2018).
51. Biosensing for the 21st Century. **109**, (2008).
52. Dechiraju, H., Jia, M., Luo, L. & Rolandi, M. Ion-Conducting Hydrogels and Their Applications in Bioelectronics. *Adv. Sustain. Syst.* 2100173 (2021) doi:10.1002/ADSU.202100173.
53. Verena Schwach & Robert Passier. Native cardiac environment and its impact on engineering cardiac tissue. *Biomater. Sci.* **7**, 3566–3580 (2019).
54. Shavandi, A. *Biomimetics*. (IntechOpen, 2021).
55. Alsberg, E., Anderson, K. W., Albeiruti, A., Rowley, J. A. & Mooney, D. J. Engineering growing tissues. *Proc. Natl. Acad. Sci.* **99**, 12025–12030 (2002).
56. S, A.-R., L, S., HR, R. & T, K. Chondrocyte-alginate constructs with or without TGF- $\beta$ 1 produces superior extracellular matrix expression than monolayer cultures. *Mol. Cell. Biochem.* **376**, 11–20 (2013).
57. E, H., T, B. & DJ, M. Designing scaffolds to enhance transplanted myoblast survival and migration. *Tissue Eng.* **12**, 1295–1304 (2006).
58. JA, R. & DJ, M. Alginate type and RGD density control myoblast phenotype. *J. Biomed. Mater. Res.* **60**, 217–223 (2002).
59. EK, P., A, S. & DR, K. Alginate composition effects on a neural stem cell-seeded scaffold. *Tissue Eng. Part C. Methods* **15**, 541–550 (2009).
60. Candiello, J., Singh, S. S., Task, K., Kumta, P. N. & Banerjee, I. Early differentiation patterning of mouse embryonic stem cells in response to variations in alginate substrate stiffness. *J. Biol. Eng.* **2013 717**, 1–14 (2013).
61. Lee, K. Y. & Mooney, D. J. Alginate: properties and biomedical applications. *Prog. Polym. Sci.* **37**, 106 (2012).
62. Pati, F. & Cho, D.-W. Bioprinting of 3D Tissue Models Using Decellularized Extracellular Matrix Bioink. *Methods Mol. Biol.* **1612**, 381–390 (2017).

63. Freeman, F. E. & Kelly, D. J. Tuning Alginate Bioink Stiffness and Composition for Controlled Growth Factor Delivery and to Spatially Direct MSC Fate within Bioprinted Tissues. *Sci. Reports* **2017 717**, 1–12 (2017).
64. C. Piras, C. & K. Smith, D. Multicomponent polysaccharide alginate-based bioinks. *J. Mater. Chem. B* **8**, 8171–8188 (2020).
65. Shim, J.-H., Lee, J.-S., Kim, J. Y. & Cho, D.-W. Bioprinting of a mechanically enhanced three-dimensional dual cell-laden construct for osteochondral tissue engineering using a multi-head tissue/organ building system. *J. Micromechanics Microengineering* **22**, 085014 (2012).
66. K, M. *et al.* 3D Bioprinting Human Chondrocytes with Nanocellulose-Alginate Bioink for Cartilage Tissue Engineering Applications. *Biomacromolecules* **16**, 1489–1496 (2015).
67. K, C. *et al.* Freeform inkjet printing of cellular structures with bifurcations. *Biotechnol. Bioeng.* **112**, 1047–1055 (2015).
68. Mandrycky, C., Wang, Z., Kim, K. & Kim, D. H. 3D bioprinting for engineering complex tissues. *Biotechnol. Adv.* **34**, 422–434 (2016).
69. Maciej Adamczyk, \*, Donald D. Johnson, and & Reddy, R. E. Bone Collagen Cross-Links: A Convergent Synthesis of (+)-Deoxypyrrrololine. *J. Org. Chem.* **66**, 11–19 (2000).
70. Kadler, K. E., Hill, A. & Canty-Laird, E. G. Collagen fibrillogenesis: fibronectin, integrins, and minor collagens as organizers and nucleators. *Curr. Opin. Cell Biol.* **20**, 495 (2008).
71. V, L. *et al.* Design and fabrication of human skin by three-dimensional bioprinting. *Tissue Eng. Part C. Methods* **20**, 473–484 (2014).
72. Maxson, E. L. *et al.* In vivo remodeling of a 3D-Bioprinted tissue engineered heart valve scaffold. *Bioprinting* **16**, e00059 (2019).
73. J, S.-W., M, T. & E, O.-K. Comparative Study of Gelatin Hydrogels Modified by Various Cross-Linking Agents. *Mater. (Basel, Switzerland)* **14**, 1–17 (2021).
74. Sun, M. *et al.* Synthesis and Properties of Gelatin Methacryloyl (GelMA) Hydrogels and Their Recent Applications in Load-Bearing Tissue. *Polymers (Basel)*. **10**, (2018).
75. LE, B. *et al.* Direct-write bioprinting of cell-laden methacrylated gelatin hydrogels. *Biofabrication* **6**, (2014).
76. L, T. *et al.* Extrusion-based 3D printing of photo-crosslinkable gelatin and κ-carrageenan hydrogel blends for adipose tissue regeneration. *Int. J. Biol. Macromol.* **140**, 929–938 (2019).
77. Nam, S. Y. & Park, S.-H. ECM Based Bioink for Tissue Mimetic 3D Bioprinting. *Adv. Exp. Med. Biol.* **1064**, 335–353 (2018).
78. Silva, K. Da, Kumar, P., Choonara, Y. E., Toit, L. C. du & Pillay, V. Three-dimensional printing of extracellular matrix (ECM)-mimicking scaffolds: A critical review of the current ECM materials. *J. Biomed. Mater. Res. Part A* **108**, 2324–2350 (2020).
79. Mendibil, U. *et al.* Tissue-specific decellularization methods: Rationale and strategies to achieve regenerative compounds. *Int. J. Mol. Sci.* **21**, 1–29 (2020).
80. J, G. & I, N. Recent trends in bioinks for 3D printing. *Biomater. Res.* **22**, (2018).
81. A, P. & LP, T. Current Status of Bioinks for Micro-Extrusion-Based 3D Bioprinting. *Molecules* **21**, (2016).
82. Jung, J. P., Bhuiyan, D. B. & Ogle, B. M. Solid organ fabrication: comparison of decellularization to 3D bioprinting. *Biomater. Res. 2016 201* **20**, 1–11 (2016).
83. D, C., HW, T., T, W. & MW, N. Organ-Derived Decellularized Extracellular Matrix: A Game Changer

- for Bioink Manufacturing? *Trends Biotechnol.* **36**, 787–805 (2018).
84. J, J. *et al.* 3D printed complex tissue construct using stem cell-laden decellularized extracellular matrix bioinks for cardiac repair. *Biomaterials* **112**, 264–274 (2017).
  85. B, T. *et al.* Development of Bioink from Decellularized Tendon Extracellular Matrix for 3D Bioprinting. *Macromol. Biosci.* **18**, (2018).
  86. F, P. *et al.* Biomimetic 3D tissue printing for soft tissue regeneration. *Biomaterials* **62**, 164–175 (2015).
  87. YJ, C. *et al.* 3D Cell Printing of Functional Skeletal Muscle Constructs Using Skeletal Muscle-Derived Bioink. *Adv. Healthc. Mater.* **5**, 2636–2645 (2016).
  88. Gao, G. *et al.* Tissue Engineered Bio-Blood-Vessels Constructed Using a Tissue-Specific Bioink and 3D Coaxial Cell Printing Technique: A Novel Therapy for Ischemic Disease. *Adv. Funct. Mater.* **27**, 1700798 (2017).
  89. Kumar, A. C. & Erothu, H. Synthetic Polymer Hydrogels. *Biomed. Appl. Polym. Mater. Compos.* 141–162 (2016) doi:10.1002/9783527690916.CH6.
  90. Yi, F.-L. *et al.* Polyacrylamide Hydrogel Composite E-skin Fully Mimicking Human Skin. *ACS Appl. Mater. Interfaces* **13**, 32084–32093 (2021).
  91. Saygili, E. *et al.* An alginate-poly(acrylamide) hydrogel with TGF- $\beta$ 3 loaded nanoparticles for cartilage repair: Biodegradability, biocompatibility and protein adsorption. *Int. J. Biol. Macromol.* **172**, 381–393 (2021).
  92. Hyon, S.-H., Cha, W.-I. & Ikada, Y. Preparation of transparent poly(vinyl alcohol) hydrogel. *Polym. Bull.* 1989 222 **22**, 119–122 (1989).
  93. F, Y. *et al.* Evaluation of a polyvinyl alcohol-alginate based hydrogel for precise 3D bioprinting. *J. Biomed. Mater. Res. A* **106**, 2944–2954 (2018).
  94. Bendtsen, S. T., Quinnell, S. P. & Wei, M. Development of a novel alginate-polyvinyl alcohol-hydroxyapatite hydrogel for 3D bioprinting bone tissue engineered scaffolds. *J. Biomed. Mater. Res. Part A* **105**, 1457–1468 (2017).
  95. Ulbricht, J., Jordan, R. & Luxenhofer, R. On the biodegradability of polyethylene glycol, polypeptoids and poly(2-oxazoline)s. *Biomaterials* **35**, 4848–4861 (2014).
  96. Xin, S., Chimene, D., Garza, J. E., Gaharwar, A. K. & Alge, D. L. Clickable PEG hydrogel microspheres as building blocks for 3D bioprinting. *Biomater. Sci.* **7**, 1179–1187 (2019).
  97. Piluso, S. *et al.* 3D bioprinting of molecularly engineered PEG-based hydrogels utilizing gelatin fragments. *Biofabrication* **13**, 045008 (2021).
  98. M, L. & W, T. Synthesis of polycaprolactone: a review. *Chem. Soc. Rev.* **38**, 3484–3504 (2009).
  99. Vijayavenkataraman, S., Vialli, N., Fuh, J. Y. H. & Lu, W. F. Conductive collagen/polypyrrole-b-polycaprolactone hydrogel for bioprinting of neural tissue constructs. *Int. J. Bioprinting* **5**, 31–43 (2019).
  100. Ramasamy, S. *et al.* Optimized construction of a full thickness human skin equivalent using 3D bioprinting and a PCL/collagen dermal scaffold. *Bioprinting* **21**, e00123 (2021).
  101. Fathi-Achachelouei, M. *et al.* Use of Nanoparticles in Tissue Engineering and Regenerative Medicine. *Front. Bioeng. Biotechnol.* **0**, 113 (2019).
  102. Agarwala, S. Electrically Conducting Hydrogels for Health care: Concept, Fabrication Methods, and Applications. *Int. J. Bioprinting* **6**, 1–15 (2020).
  103. Bhat, M. A., Rather, R. A. & Shalla, A. H. PEDOT and PEDOT:PSS conducting polymeric hydrogels:

- A report on their emerging applications. *Synth. Met.* **273**, 116709 (2021).
104. Yan Yang, Hua Deng & Qiang Fu. Recent progress on PEDOT:PSS based polymer blends and composites for flexible electronics and thermoelectric devices. *Mater. Chem. Front.* **4**, 3130–3152 (2020).
  105. Luo, S.-C. *et al.* Poly(3,4-ethylenedioxythiophene) (PEDOT) Nanobiointerfaces: Thin, Ultrasmooth, and Functionalized PEDOT Films with in Vitro and in Vivo Biocompatibility. *Langmuir* **24**, 8071–8077 (2008).
  106. Louwet, F. *et al.* PEDOT/PSS: synthesis, characterization, properties and applications. *Synth. Met.* **135–136**, 115–117 (2003).
  107. Tandon, B., Blaker, J. J. & Cartmell, S. H. Piezoelectric materials as stimulatory biomedical materials and scaffolds for bone repair. *Acta Biomater.* **73**, 1–20 (2018).
  108. Ribeiro, C., Sencadas, V., Correia, D. M. & Lanceros-Méndez, S. Piezoelectric polymers as biomaterials for tissue engineering applications. *Colloids Surfaces B Biointerfaces* **136**, 46–55 (2015).
  109. Spencer, A. R. *et al.* Bioprinting of a Cell-Laden Conductive Hydrogel Composite. *ACS Appl. Mater. Interfaces* **11**, 30518–30533 (2019).
  110. Heo, D. N. *et al.* Development of 3D printable conductive hydrogel with crystallized PEDOT:PSS for neural tissue engineering. *Mater. Sci. Eng. C* **99**, 582–590 (2019).
  111. Roshanbinfar, K. *et al.* Electroconductive Biohybrid Hydrogel for Enhanced Maturation and Beating Properties of Engineered Cardiac Tissues. *Adv. Funct. Mater.* **28**, 1803951 (2018).
  112. Aggas, J. R., Abasi, S., Phipps, J. F., Podstawczyk, D. A. & Guiseppi-Elie, A. Microfabricated and 3-D printed electroconductive hydrogels of PEDOT:PSS and their application in bioelectronics. *Biosens. Bioelectron.* **168**, 112568 (2020).
  113. Nyoung, H. *et al.* Directly Induced Neural Differentiation of Human Adipose-Derived Stem Cells Using Three-Dimensional Culture System of Conductive Microwell with Electrical Stimulation. <https://home.liebertpub.com/tea> **24**, 537–545 (2018).
  114. Wu, Y. *et al.* Fabrication of conductive gelatin methacrylate–polyaniline hydrogels. *Acta Biomater.* **33**, 122–130 (2016).
  115. Wright, C. J. *et al.* Synthesis and 3D Printing of Conducting Alginate–Polypyrrole Ionomers. *Gels* **2020**, Vol. 6, Page 13 **6**, 13 (2020).
  116. Vijayavenkataraman, S., Vialli, N., Fuh, J. Y. H. & Lu, W. F. Conductive collagen/polypyrrole-b-polycaprolactone hydrogel for bioprinting of neural tissue constructs. *Int. J. Bioprinting* **5**, 31–43 (2019).
  117. Wang, Y. *et al.* 3D bioprinting of conductive hydrogel for enhanced myogenic differentiation. *Regen. Biomater.* **8**, (2021).
  118. Hadi Rastin *et al.* 3D bioprinting of cell-laden electroconductive MXene nanocomposite bioinks. *Nanoscale* **12**, 16069–16080 (2020).
  119. Baei, P. *et al.* Electrically conductive gold nanoparticle-chitosan thermosensitive hydrogels for cardiac tissue engineering. *Mater. Sci. Eng. C* **63**, 131–141 (2016).
  120. Navaei, A. *et al.* Gold nanorod-incorporated gelatin-based conductive hydrogels for engineering cardiac tissue constructs. *Acta Biomater.* **41**, 133–146 (2016).
  121. Liu, X., Kim, J. C., Miller, A. L., Waletzki, B. E. & Lu, L. Electrically conductive nanocomposite hydrogels embedded with functionalized carbon nanotubes for spinal cord injury. *New J. Chem.* **42**,

- 17671–17681 (2018).
122. Jiang, L. *et al.* Preparation of an Electrically Conductive Graphene Oxide/Chitosan Scaffold for Cardiac Tissue Engineering. *Appl. Biochem. Biotechnol.* 2019 1884 **188**, 952–964 (2019).
  123. Jacob, J., More, N., Kalia, K. & Kapusetti, G. Piezoelectric smart biomaterials for bone and cartilage tissue engineering. *Inflamm. Regen.* 2018 381 **38**, 1–11 (2018).
  124. G, C., L, R. & V, M. Preparation, characterization and in vitro testing of poly(lactic-co-glycolic) acid/barium titanate nanoparticle composites for enhanced cellular proliferation. *Biomed. Microdevices* **13**, 255–266 (2011).
  125. Rocha, L. B., Goissis, G. & Rossi, M. A. Biocompatibility of anionic collagen matrix as scaffold for bone healing. *Biomaterials* **23**, 449–456 (2002).
  126. Ashammakhi, N. *et al.* Advances and Future Perspectives in 4D Bioprinting. *Biotechnol. J.* **13**, 1800148 (2018).
  127. Kokkinis, D., Schaffner, M. & Studart, A. R. Multimaterial magnetically assisted 3D printing of composite materials. *Nat. Commun.* 2015 61 **6**, 1–10 (2015).
  128. Tang, J. *et al.* Super tough magnetic hydrogels for remotely triggered shape morphing. *J. Mater. Chem. B* **6**, 2713–2722 (2018).
  129. Silva, E. D. *et al.* Multifunctional magnetic-responsive hydrogels to engineer tendon-to-bone interface. *Nanomedicine Nanotechnology, Biol. Med.* **14**, 2375–2385 (2018).
  130. Ziv-Polat, O., Skaat, H., Shahar, A. & Margel, S. Novel magnetic fibrin hydrogel scaffolds containing thrombin and growth factors conjugated iron oxide nanoparticles for tissue engineering. *Int. J. Nanomedicine* **7**, 1259 (2012).
  131. Cardiovascular diseases. [https://www.who.int/health-topics/cardiovascular-diseases/#tab=tab\\_1](https://www.who.int/health-topics/cardiovascular-diseases/#tab=tab_1).
  132. Das, S. & Jang, J. 3D bioprinting and decellularized ECM-based biomaterials for in vitro CV tissue engineering. <https://doi.org/10.2217/3dp-2018-0002> **2**, 69–87 (2018).
  133. Arnal-Pastor, M., Chachques, J. C., Pradas, M. M. & Vallés-Lluch, A. Biomaterials for Cardiac Tissue Engineering. (2013) doi:10.5772/56076.
  134. Vunjak-Novakovic, G. *et al.* Challenges in Cardiac Tissue Engineering. <https://home.liebertpub.com/teb> **16**, 169–187 (2009).
  135. Eschenhagen, T., Didié, M., Heubach, J., Ravens, U. & Zimmermann, W. H. Cardiac tissue engineering. *Transpl. Immunol.* **9**, 315–321 (2002).
  136. Zhao, G., Qiu, Y., Zhang, H. M. & Yang, D. Intercalated discs: cellular adhesion and signaling in heart health and diseases. *Heart Fail. Rev.* **24**, 115–132 (2019).
  137. Shiels, H. A. Design and physiology of the heart | Cardiac Cellular Length-Tension Relationship. *Encycl. Fish Physiol.* **2**, 1060–1066 (2011).
  138. C., V. *et al.* Immaturity of Human Stem-Cell-Derived Cardiomyocytes in Culture: Fatal Flaw or Soluble Problem? <https://home.liebertpub.com/scd> **24**, 1035–1052 (2015).
  139. Hong, T. T. & Shaw, R. M. Cardiac T-Tubule Microanatomy and Function. *Physiol. Rev.* **97**, 227–252 (2017).
  140. Eisner, D. A., Caldwell, J. L., Kistamás, K. & Trafford, A. W. Calcium and Excitation-Contraction Coupling in the Heart. *Circ. Res.* **121**, 181–195 (2017).
  141. Woodcock, E. A. & Matkovich, S. J. Cardiomyocytes structure, function and associated pathologies. *Int. J. Biochem. Cell Biol.* **37**, 1746–1751 (2005).
  142. Hortensius, R. A., Lin, W. H. & Ogle, B. M. Cardiac Tissue Engineering: A Pathway for Repair. *Eng.*

- Med. Adv. Challenges* 3–33 (2019) doi:10.1016/B978-0-12-813068-1.00001-4.
143. Karbassi, E. *et al.* Cardiomyocyte maturation: advances in knowledge and implications for regenerative medicine. *Nat. Rev. Cardiol.* 2020 176 **17**, 341–359 (2020).
  144. Veerman, C. C. *Inherited arrhythmia syndromes: From genotype to phenotype in hiPSC-derived cardiomyocytes.* (2017).
  145. Karakikes, I., Ameen, M., Termglinchan, V. & Wu, J. C. Human Induced Pluripotent Stem Cell–Derived Cardiomyocytes. *Circ. Res.* **117**, 80–88 (2015).
  146. Peters, N. S. *et al.* Spatiotemporal relation between gap junctions and fascia adherens junctions during postnatal development of human ventricular myocardium. *Circulation* **90**, 713–725 (1994).
  147. Jiang, Y., Park, P., Hong, S.-M. & Ban, K. Maturation of Cardiomyocytes Derived from Human Pluripotent Stem Cells: Current Strategies and Limitations. *Mol. Cells* **41**, 613 (2018).
  148. Lundy, S. D., Zhu, W.-Z., Regnier, M. & Laflamme, M. A. Structural and Functional Maturation of Cardiomyocytes Derived from Human Pluripotent Stem Cells. <https://home.liebertpub.com/scd> **22**, 1991–2002 (2013).
  149. Radisic, M. *et al.* Functional assembly of engineered myocardium by electrical stimulation of cardiac myocytes cultured on scaffolds. *Proc. Natl. Acad. Sci.* **101**, 18129–18134 (2004).
  150. Lieu, D. K. *et al.* Mechanism-Based Facilitated Maturation of Human Pluripotent Stem Cell–Derived Cardiomyocytes. *Circ. Arrhythmia Electrophysiol.* **6**, 191–201 (2013).
  151. Shyu, K.-G. Cellular and molecular effects of mechanical stretch on vascular cells and cardiac myocytes. *Clin. Sci.* **116**, 377–389 (2009).
  152. Shimko, V. F. & Claycomb, W. C. Effect of Mechanical Loading on Three-Dimensional Cultures of Embryonic Stem Cell-Derived Cardiomyocytes. <https://home.liebertpub.com/tea> **14**, 49–58 (2008).
  153. Haizlip, K. M. & Janssen, P. M. L. In vitro studies of early cardiac remodeling: impact on contraction and calcium handling. *Front. Biosci. (Schol. Ed.)* **3**, 1047 (2011).
  154. Ruan, J.-L. *et al.* Mechanical Stress Conditioning and Electrical Stimulation Promote Contractility and Force Maturation of Induced Pluripotent Stem Cell-Derived Human Cardiac Tissue. *Circulation* **134**, 1557–1567 (2016).
  155. Abilez, O. J. *et al.* Passive Stretch Induces Structural and Functional Maturation of Engineered Heart Muscle as Predicted by Computational Modeling. *Stem Cells* **36**, 265–277 (2018).
  156. Ronaldson-Bouchard, K. *et al.* Advanced maturation of human cardiac tissue grown from pluripotent stem cells. *Nat.* 2018 5567700 **556**, 239–243 (2018).
  157. Ribeiro, A. J. S. *et al.* Contractility of single cardiomyocytes differentiated from pluripotent stem cells depends on physiological shape and substrate stiffness. *Proc. Natl. Acad. Sci.* **112**, 12705–12710 (2015).
  158. Yang, X., Pabon, L. & Murry, C. E. Engineering Adolescence. *Circ. Res.* **114**, 511–523 (2014).
  159. Abecasis, B. *et al.* Unveiling the molecular crosstalk in a human induced pluripotent stem cell-derived cardiac model. *Biotechnol. Bioeng.* **116**, 1245–1252 (2019).
  160. Shadrin, I. Y. *et al.* Cardiopatch platform enables maturation and scale-up of human pluripotent stem cell-derived engineered heart tissues. *Nat. Commun.* 2017 81 **8**, 1–15 (2017).
  161. Sun, X. & Nunes, S. S. Biowire platform for maturation of human pluripotent stem cell-derived cardiomyocytes. *Methods* **101**, 21–26 (2016).
  162. Rodrigues, I. C. P., Kaasi, A., Maciel Filho, R., Jardini, A. L. & Gabriel, L. P. Cardiac tissue engineering: current state-of-the-art materials, cells and tissue formation. *Einstein (São Paulo)* **16**,

- eRB4538 (2018).
163. Wang, Z. *et al.* 3D bioprinting in cardiac tissue engineering. *Theranostics* **11**, 7948 (2021).
  164. M, L., K, L., A, E. & DL, K. Vascularization strategies for tissue engineering. *Tissue Eng. Part B. Rev.* **15**, 353–370 (2009).
  165. VK, L. & G, D. Printing of Three-Dimensional Tissue Analogs for Regenerative Medicine. *Ann. Biomed. Eng.* **45**, 115–131 (2017).
  166. A, L. *et al.* 3D bioprinting of collagen to rebuild components of the human heart. *Science* **365**, 482–487 (2019).
  167. N, A., H, P., GR, K., KM, S. & LJ, W. Bone extracellular matrix hydrogel enhances osteogenic differentiation of C2C12 myoblasts and mouse primary calvarial cells. *J. Biomed. Mater. Res. B. Appl. Biomater.* **106**, 900–908 (2018).
  168. Distler, T. *et al.* Electrically Conductive and 3D-Printable Oxidized Alginate-Gelatin Polypyrrole:PSS Hydrogels for Tissue Engineering. *Adv. Healthc. Mater.* **10**, 2001876 (2021).
  169. Manjua, A. C., Alves, V. D., Crespo, J. G. & Portugal, C. A. M. Magnetic Responsive PVA Hydrogels for Remote Modulation of Protein Sorption. *ACS Appl. Mater. Interfaces* **11**, 21239–21249 (2019).
  170. Vaithilingam, J. *et al.* Multifunctional Bioinspired 3D Architectures to Modulate Cellular Behavior. *Adv. Funct. Mater.* **29**, 1902016 (2019).
  171. Mosqueira, D. *et al.* CRISPR/Cas9 editing in human pluripotent stem cell-cardiomyocytes highlights arrhythmias, hypocontractility, and energy depletion as potential therapeutic targets for hypertrophic cardiomyopathy. *Eur. Heart J.* **39**, 3879–3892 (2018).
  172. Roshanbinfar, K. *et al.* Electroconductive Biohybrid Hydrogel for Enhanced Maturation and Beating Properties of Engineered Cardiac Tissues. *Adv. Funct. Mater.* **28**, 1803951 (2018).
  173. Nyong, H. *et al.* Directly Induced Neural Differentiation of Human Adipose-Derived Stem Cells Using Three-Dimensional Culture System of Conductive Microwell with Electrical Stimulation. <https://home.liebertpub.com/tea> **24**, 537–545 (2018).
  174. Reinoso, R. F., Telfer, B. A. & Rowland, M. Tissue water content in rats measured by desiccation. *J. Pharmacol. Toxicol. Methods* **38**, 87–92 (1997).
  175. Yuk, H. *et al.* 3D printing of conducting polymers. *Nat. Commun.* **2020 111** **11**, 1–8 (2020).
  176. Oldenburger, M. *et al.* Investigation of the low frequency Warburg impedance of Li-ion cells by frequency domain measurements. *J. Energy Storage* **21**, 272–280 (2019).
  177. Nguyen, T. Q. & Breitung, C. Determination of Diffusion Coefficients Using Impedance Spectroscopy Data. *J. Electrochem. Soc.* **165**, E826 (2018).
  178. Kumar, J. & Rajesh Kumar, D. Estimation of Loss Factor of Viscoelastic Material by Using Cantilever Sandwich Plate.
  179. Zare, Y., Park, S. P. & Rhee, K. Y. Analysis of complex viscosity and shear thinning behavior in poly (lactic acid)/poly (ethylene oxide)/carbon nanotubes biosensor based on Carreau–Yasuda model. *Results Phys.* **13**, 102245 (2019).
  180. Li, S., Zhao, G. & Chen, H. The Relationship between Steady Shear Viscosity and Complex Viscosity. <http://dx.doi.org/10.1081/DIS-200054555> **26**, 415–419 (2006).
  181. Colosi, C. *et al.* Microfluidic Bioprinting of Heterogeneous 3D Tissue Constructs Using Low-Viscosity Bioink. *Adv. Mater.* **28**, 677–684 (2016).
  182. Pislaru, C., Urban, M. W., Pislaru, S. V., Kinnick, R. R. & Greenleaf, J. F. Viscoelastic Properties of Normal and Infarcted Myocardium Measured by a Multifrequency Shear Wave Method: Comparison



- with Pressure-Segment Length Method. *Ultrasound Med. Biol.* **40**, 1785–1795 (2014).
183. Das, S. *et al.* Decellularized extracellular matrix bioinks and the external stimuli to enhance cardiac tissue development in vitro. *Acta Biomater.* **95**, 188–200 (2019).
184. W, L. *et al.* Extrusion Bioprinting of Shear-Thinning Gelatin Methacryloyl Bioinks. *Adv. Healthc. Mater.* **6**, (2017).
185. Adhikari, J. *et al.* Effects of Processing Parameters of 3D Bioprinting on the Cellular Activity of Bioinks. *Macromol. Biosci.* **21**, (2021).
186. Gillispie, G. J. *et al.* The Influence of Printing Parameters and Cell Density on Bioink Printing Outcomes. <https://home.liebertpub.com/tea> **26**, 1349–1358 (2020).
187. van Wijk, B., Moorman, A. F. M. & van den Hoff, M. J. B. Role of bone morphogenetic proteins in cardiac differentiation. *Cardiovasc. Res.* **74**, 244–255 (2007).
188. Kim, M.-S. *et al.* Activin-A and Bmp4 Levels Modulate Cell Type Specification during CHIR-Induced Cardiomyogenesis. *PLoS One* **10**, 118670 (2015).
189. Lian, X. *et al.* Directed cardiomyocyte differentiation from human pluripotent stem cells by modulating Wnt/ $\beta$ -catenin signaling under fully defined conditions. *Nat. Protoc.* **8**, 162 (2013).